# Implementation of a Microstrip Square Planar *N*-Way Metamaterial Power Divider

Junyao Zong

A thesis submitted in partial fulfilment
of the requirements for the Degree of
Master of Engineering
in
Electrical and Electronic Engineering
at the
University of Canterbury,
Christchurch, New Zealand.

June 2008

# ABSTRACT

The work done in this thesis focuses on the design of a square-shaped 20-way metamaterial power divider which is fabricated in microstrip technology and operates at 1 GHz. The divider comprises 12 square-shaped left-handed unit cells and 13 square-shaped right-handed unit cells, and these unit cells have the same size and are placed in a checker-board tessellation, where the left-handed unit cells are connected only to right-handed unit cells and vice versa. The divider is based upon the infinite wavelength phenomenon in two-dimensions, and this means that the insertion phase between any two ports of the left-handed unit cell is equal, but with opposite sign, to that of the right-handed unit cell. The divider gives an equal-amplitude equal-phase power division from the central input port to the output ports which are located on a straight line on each side. Thus, it is convenient to integrate with, or interconnect to, other planar circuits in a system, such as power amplifier modules. The design concept can be extended to an $N$-way power divider, where $N = 4n$ and $n$ is an odd integer.

# ACKNOWLEDGEMENT

I would sincerely like to express my thanks to my supervisor Dr. Kim W. Eccleston, for his patient guidance, help and encouragement.

Also, thanks to Randy Hampton, Nick Smith, Ron Battersby and Malcolm Gordon for fabricating the microstrip circuits and test fixtures.

I would also like to thank my parents for their love, support and encouragement in my studying time of this thesis.

Finally, thanks to my friends for their friendship and assistance.

# CONTENTS

# LIST OF FIGURES

# LIST OF TABLES

# ABBREVIATIONS AND ACRONYMS

**1D** one dimensional

**2D** two dimensional

**3D** three dimensional

**BW** backward wave

**DNG** double-negative

**LH** left-handed

**LHM** left-handed material

**MM** metamaterial

**NRI** negative-refractive-index

**PCB** printed circuit board

**RH** right-handed

**RHM** right-handed material

**SRR** Split Ring-Resonator

**TL** transmission line

**TMM** tessellated metamaterial

# Chapter 1

# INTRODUCTION

## 1.1 MICROWAVE POWER DIVIDER/COMBINER

Power dividers/combiners have been used widely in microwave applications. For example, they have been used in antenna-array feeding networks and solid-state power amplifier combiner networks. In recent years, it is desirable in developing power combining techniques for solid-state power generation to achieve high output power with low loss, high combining efficiency and wide bandwidth. Various microwave power combining techniques have been summarised in the literature [1].

Power combining can be separated into two general levels: the device level and the circuit level [1]. Device level combining techniques place devices in a small area compared to a wavelength, so it is limited in the number of devices. Circuit level combining techniques, on the other hand, are not limited to clustering devices in a small region compared to a wavelength. In this thesis, we are more interested in circuit level combining technique, such as a parallel combined power amplifier. In general, a parallel combined power amplifier consists of a power divider network, $N$ amplifiers and a power combiner network. Since the power divider and combiner networks are usually identical, the same network can be used as either a power divider or a power combiner, and therefore it will be referred to as a divider/combiner network.

There are many different methods for combining techniques. At the circuit level, combining approaches can be classified into two categories: one is that the outputs of all devices are combined in a single step, and one is that power is combined in several

steps [1]. The former are also called *N*-way combiners, and can be divided into resonant and nonresonant cavity combiners. The latter can be separated into chain (or serial) and tree (or corporate) combining structures. The Figure 1.1 shows many different methods for combining.

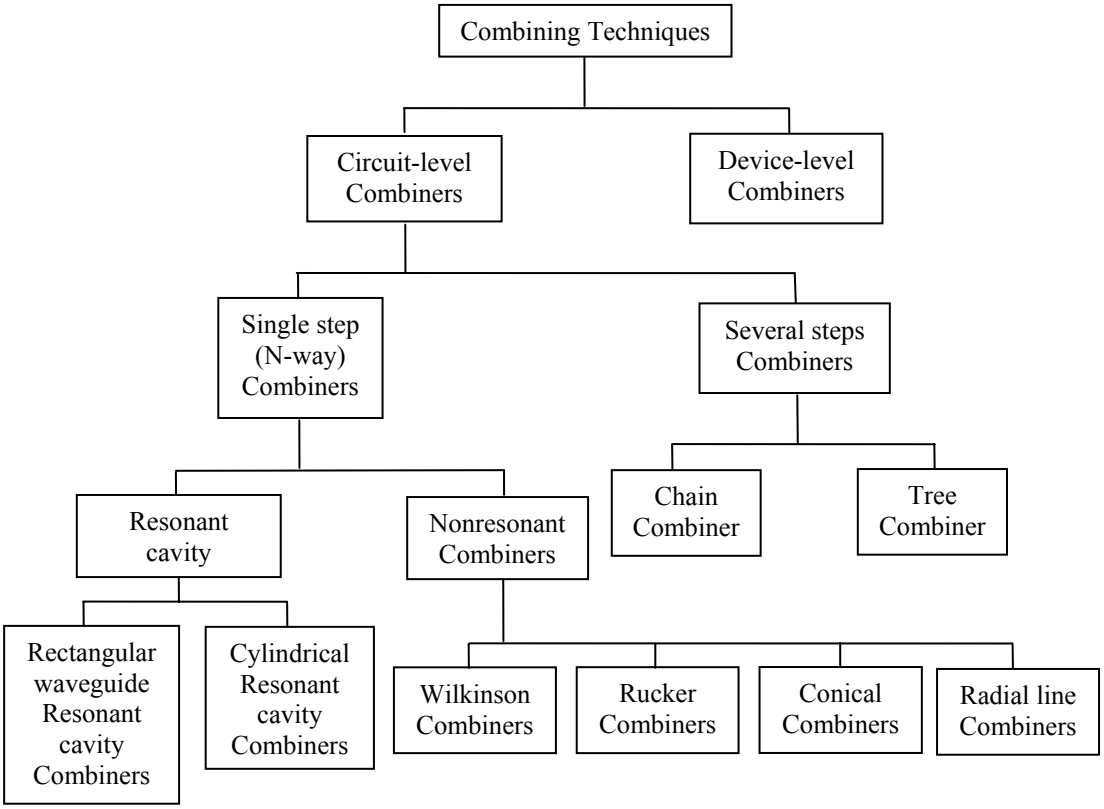


Fig. 1.1. Different combining techniques.

Each of these methods has its own advantages and disadvantages. Chain or tree combiners have the advantage of wide bandwidth and isolation between devices [2], but have the disadvantage of using couplers and connecting sections which cause more losses and decrease the combining efficiency, especially for a large number of devices [3]. Resonant *N*-way combiners have high combining efficiency but narrow bandwidth. Nonresonant *N*-way combiners provide wide bandwidth, but have the disadvantage of isolation problems, which lead to undesired higher order modes.

## 1.2 LEFT-HANDED MATERIALS

In recent times, a hot topic in microwave engineering is left-handed (LH) materials, also called metamaterials (MMs). Left-handed materials (LHMs) are artificial structures that exhibit specific electromagnetic properties which are not shown in natural materials. Novel applications and devices have been developed using these unique properties of left-handed materials, so *Science* magazine chose left-handed materials as one of the top ten scientific breakthroughs of 2003 [4].

Conventional materials simultaneously have positive permittivity and permeability, and group and phase velocities both directed away from the source; hence the phase lags in the direction of the positive group velocity. In the late 1960s, Veselago first theoretically studied materials with simultaneous negative permittivity and permeability [5]. Veselago named these materials left-handed materials (LHMs) because electric field intensity vector **E**, magnetic field intensity vector **H** and wavevector **k** would form a left-handed triplet. Yet, **E**, **H** and the Poynting vector **S** maintain a right-handed relationship, thus left-handed materials exhibit a group velocity directed away from the source whilst the phase velocity is directed toward the source, hence the term backward waves. In other words, the phase leads in the direction of the positive group velocity.

The first realisation of such materials was developed by Shelby *et al*. [6], using thin wire strips and Split Ring-Resonators (SRRs). However, these structures rely on resonances and are inherently narrowband and lossy, so they are difficult to implement for microwave applications. Structures using the transmission line (TL) approach have been developed that do not rely upon resonances [7] [8], and are amenable to microwave PCB technology [9]. These structures are based upon periodically loaded transmission lines with lumped elements, inductors and capacitors.

### 1.2.1 TERMINOLOGY

There are several terminologies found in the literature to describe metamaterials with simultaneous negative permittivity and permeability. The most frequently used terms are listed as follows [10] [11]:

- Left-handed (LH): This is the nomenclature named by Veselago, and it describes the most fundamental property of these materials.
- Backward wave (BW): This terminology mentions the property of antiparallel phase/group velocities.
- Negative-refractive-index (NRI): It shows a meaningful property for two dimensional (2D) and three dimensional (3D) structures, but it cannot describe one dimensional (1D) structures.
- Double-negative (DNG): It comes from the fact that these materials have simultaneously negative permittivity and permeability.

## 1.3 *N*-WAY MCIROWAVE POWER DIVIDER USING TWO-DIMENSIONAL METAMATERIALS

In this thesis, we propose a new structure of *N*-way power divider comprising 2D left-handed and right-handed unit cells [12] [13]. To achieve equal magnitude and phase for voltages at all the output ports, left-handed unit cells are connected only to right-handed unit cells, and vice versa. This structure is square-shaped and is easily integrated with amplifiers. In addition, this structure represents the infinite wavelength phenomenon in two-dimensions and could replace a circular radial power divider. To validate design methods and fabrication techniques, a 20-way power divider was constructed and measured.

## 1.4 OUTLINE OF THESIS

The thesis is organized as follows. In Chapter 2, a background is given to *N*-way power dividers in parallel combined power amplifiers, and the transmission line approach to left-handed materials. In Chapter 3, we reveal in detail the structure and principle of the 20-way power divider proposed in this thesis, and then discuss the equivalent 1D model of the 2D unit cell, and finally give the design overview. In

Chapter 4, we give the design details of 1D left-handed unit cell, and then we show the simulation and measurement results. In Chapter 5, we design and fabricate the 20-way power divider, and then simulation and test results are presented. In Chapter 6, we conclude with the core results of this thesis and indicate possible future research. Throughout this thesis, AWR Microwave Office was used to simulate all the circuits.

# Chapter 2

# BACKGROUND

In this chapter, we review the background materials related to this thesis. In section 2.1, we give general descriptions of several different *N*-way power dividers in a parallel combined power amplifier. In section 2.2, we describe the transmission line theory of left-handed transmission line and present the practical 1D and 2D unit cells for left-handed material.

## 2.1 *N*-WAY POWER DIVIDER

### 2.1.1 DIFFERENT TYPES OF *N*-WAY POWER DIVIDER

The *N*-way power divider is used extensively in microwave applications, where it is used to divide and combine microwave power. Microstrip line technology is used widely in *N*-way power dividers, because it is cheap and easy to fabricate, and can be integrated with amplifier modules. There are several useful microstrip line *N*-way power dividers: radial power dividers [3] [14], fork power dividers [15], sector-shaped power dividers [16] [17] and tapered line power dividers [18] [19]. The examples of these power dividers are shown in Figure 2.1.

The radial power divider shown in Figure 2.1 (a) is well known for its ability to achieve an *N*-way power split, especially for larger *N*, and it presents low loss and excellent balance performance of amplitude and phase [3]. Radial power dividers consist of two sections: the launcher and the radial line. The launcher section is a coaxial line which feeds a radial line in the centre. The radial line is a circular, low

loss parallel-plate transmission line, and it is used to split the signal into output ports which are located around the side of radial line.

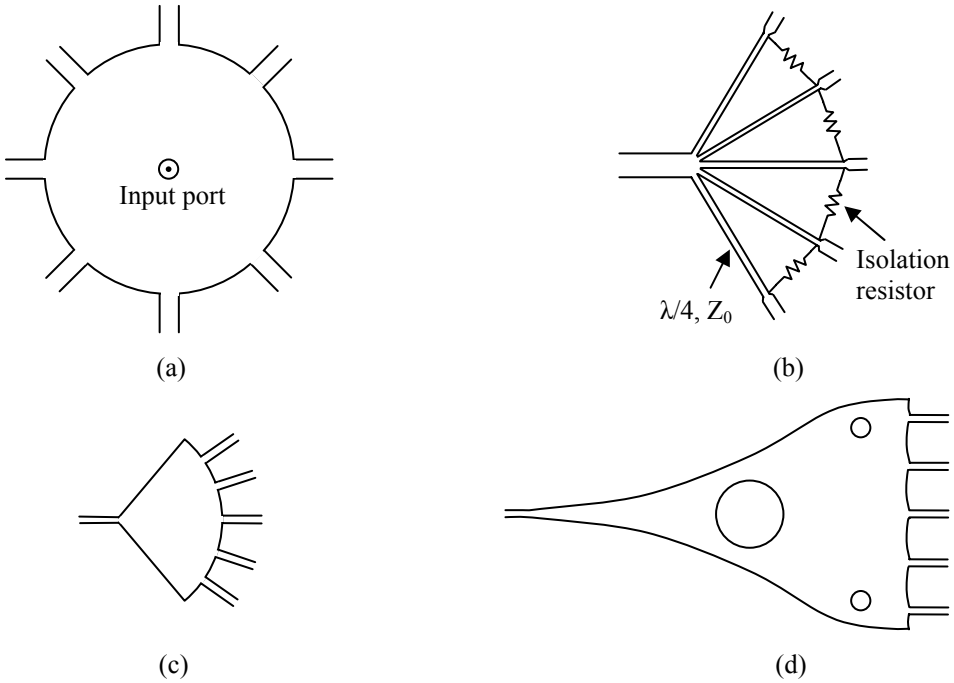


Fig. 2.1 Several different types of *N*-way power divider.
(a) Radial power divider. (b) Fork power divider.
(c) Sector-shaped power divider. (d) Tapered line power divier [19].

The fork power divider shown in Figure 2.1 (b) exhibits low loss, a good performance of isolation between output ports and a broad bandwidth [15]. As shown in Figure 2.1 (b), the splitter part consists of $N$ transmission lines, which have characteristic impedance $Z_0$ and quarter wavelength length at the centre frequency, and $N$-1 isolation resistors between adjacent output ports. The sector-shaped power divider shown in Figure 2.1 (c) uses a sectorial transmission line to divide signal into $N$ output ports which are located with evenly space on a sectorial side, and it has a good amplitude balance performance and a wide bandwidth [16]. The tapered microstrip line power divider presents a good balance performance of amplitude and phase and a wide bandwidth [18]. In Figure 2.1 (d), it is a special tapered microstrip line power divider [19], and its output ports are located on a straight line, and the holes in the structure are used to equalise the transmission path lengths from the input port to the output ports [19]. The three power dividers, which are fork, sector-shaped

and tapered line power dividers, are all completely planar structure because they do not need a vertical (or probe) coaxial line feed port which is used in the radial power divider. In general, *N*-way power divider need good isolation over the bandwidth, and isolation resistors located between adjacent output ports can be used to improve the isolation performance [3] [16].

### 2.1.2 THE PARALLEL COMBINED POWER AMPLIFIER

The *N*-way power divider is often used in a parallel combined power amplifier as shown in Figure 2.2. In a parallel combined power amplifier, an *N*-way power divider is used at the input ports of *N* power amplifiers, and another *N*-way power combiner is used at the output ports of *N* amplifiers to achieve the high output power. The *N*-way power divider and combiner are identical in their structure, but with the opposite roles of their input and output ports. To achieve the maximum combining efficiency when the power divider/combiner is symmetrical, the combined signals from the amplifiers should have equal magnitude and phase [21].

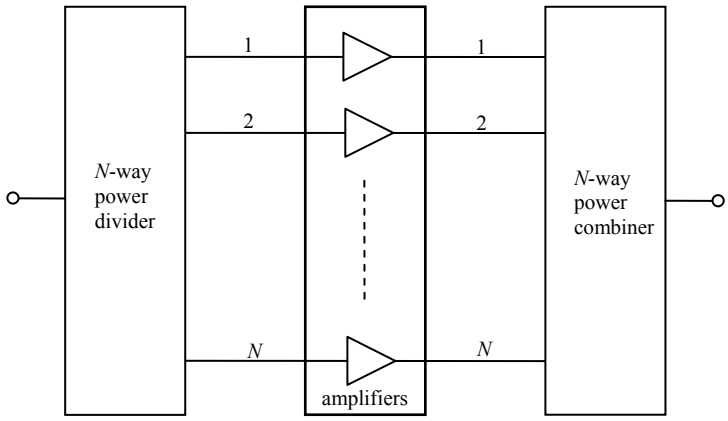


Fig. 2.2. A model for a parallel combined power amplifier [20].

As shown in Figure 2.1 (a) (b) (c), the in-phase output ports of radial, fork and sector-shaped power dividers are located on an arc or circle. In a parallel combined power amplifier, it is necessary to have equal length interconnecting transmission lines between the amplifier modules and the power divider and combiner to ensure correct phasing. Figure 2.3 shows a parallel combined power amplifier using fork

power divider and combiner [22]. It can be seen that the equal length interconnecting transmission lines are non-identically curved. When a radial power divider and combiner are used in a parallel combined power amplifier, the interconnecting transmission lines are uniform, but the amplifier modules are mounted on a cylinder [23] as shown in Figure 2.4. In this case, each amplifier is fabricated on a separate printed circuit board (PCB).

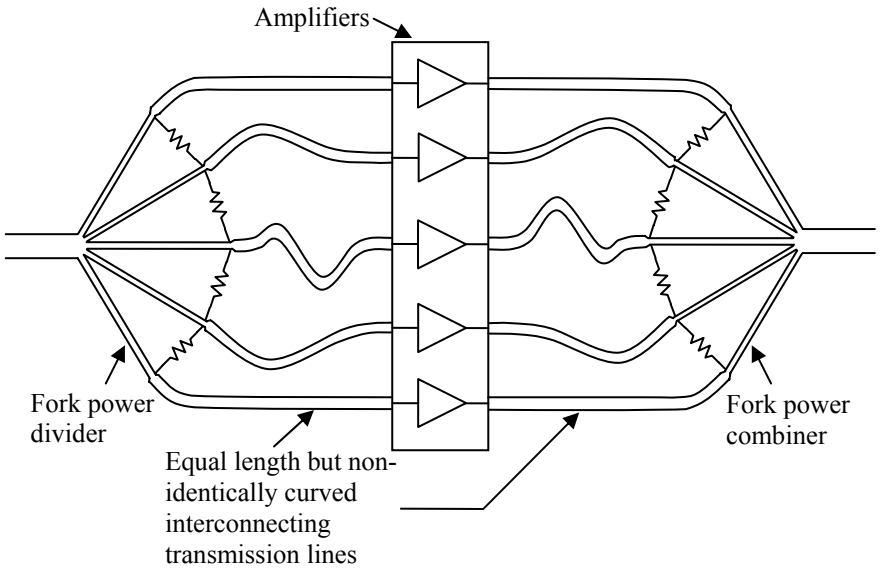


Fig. 2.3. Fork power divider/combiner used in a parallel combined power amplifier.

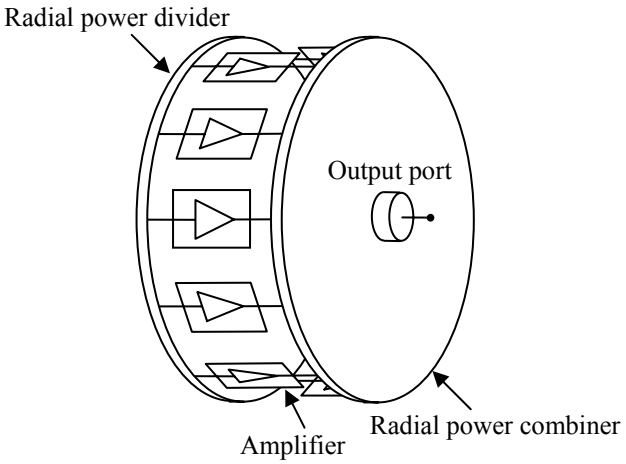


Fig. 2.4. Radial power divider/combiner used in a parallel combined power amplifier.

In a parallel combined power amplifier, it is desirable that the output ports of power divider are located on a straight line, so that it is easier to interconnect or integrate

with amplifier modules. As shown in Figure 2.1 (d), the tapered line power divider of the type in reference [19] has the output ports on a straight line; therefore, the interconnecting lines between the amplifiers and the power divider and combiner are identical as shown in Figure 2.5. Another novel power divider is a square-shaped power divider [12], which has four groups of output ports. In each group, the output ports are located on a straight line. Therefore, amplifier modules can be integrated on four PCBs, which allow them to conveniently interconnect to the power divider and combiner as shown in Figure 2.6, compared to the radial power divider shown in Figure 2.4. In this thesis, a novel square-shaped power divider will be designed, fabricated and tested, and more detail will be presented in the following chapters.

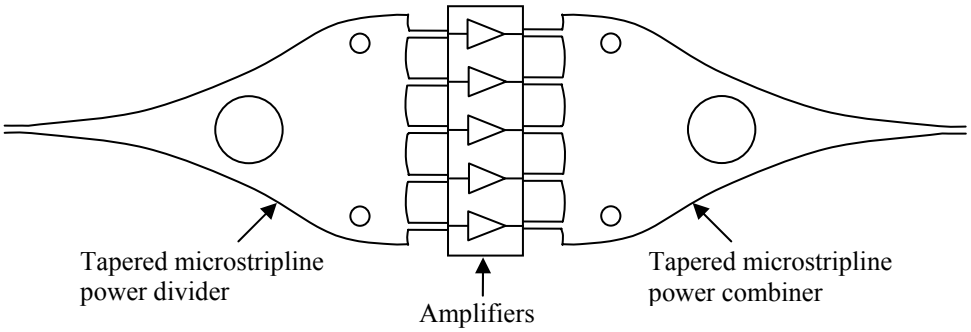


Fig. 2.5. Tapered line power divider/combiner used in a parallel combined power amplifier.

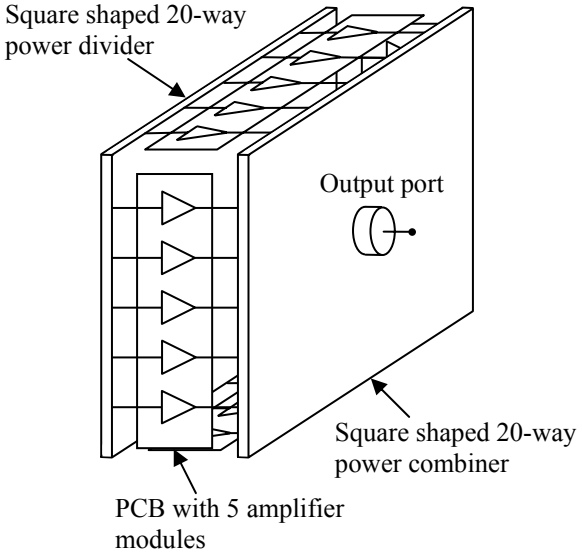


Fig. 2.6. Square shaped power divider/combiner used in a parallel combined power amplifier.

### 2.1.3 REQUIREMENTS FOR *N*-WAY POWER DIVIDER

When an *N*-way power divider is designed to achieve a good performance, some main requirements need to be fulfilled [3] [21] [22].

1. One requirement is that the *N*-way power divider needs to give an equal-amplitude equal-phase power division from the input port to the output ports.
2. The input port of the *N*-way power divider needs to be matched to the signal launching device. Therefore, there will be no power return loss due to impedance mismatch at the input port.
3. Between the input port and the output ports, the *N*-way power divider needs to have minimal insertion losses.
4. The output ports of the *N*-way power divider need to be matched to the terminations, such as amplifier modules.
5. The *N*-way power divider needs good output port isolation to obtain graceful degradation when it is used as the power combining structure and some amplifier devices fail. The output port isolation is important to the *N*-way power divider, and it is a requirement for high combining efficiency.

## 2.2 LEFT-HANDED TRANSMISSION LINE

### 2.2.1 DISTRIBUTED NETWORK APPROACH

Distributed *L*-*C* networks can be used to model dielectrics [7]. The per-unit-length inductance and capacitance can describe the permeability and permittivity, respectively [7]. Figure 2.7 shows the unit cell of a 2D distributed *L*-*C* network, and we can obtain dielectric properties derived from distributed series impedances and shunt admittances in the *L*-*C* network.

The effective dielectric parameters can be expressed as [7]

$$j\omega\mu_s = Z \Rightarrow \mu_s = \frac{Z}{j\omega} \tag{2.1}$$

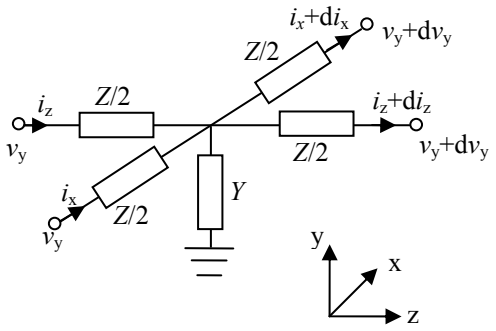


Fig. 2.7. The unit cell of a 2D distributed *L*-*C* network.

$$j\omega\varepsilon_s = Y \Rightarrow \varepsilon_s = \frac{Y}{j\omega}. \tag{2.2}$$

If we consider a 2D distributed low-pass topology with series distributed inductance per unit length, $L$, and shunt distributed capacitance per unit length, $C$, then $Z = j\omega L$ and $Y = j\omega C$, hence

$$\mu_s = L, \tag{2.3}$$

$$\varepsilon_s = C. \tag{2.4}$$

As $L$ and $C$ are positive, then $\mu_s$ and $\varepsilon_s$ are positive. Hence a 2D distributed low-pass *L*-*C* topology can model a conventional dielectric with positive valued $\mu_s$ and $\varepsilon_s$. The propagation constant can be written as

$$\beta = \sqrt{-ZY} = \omega\sqrt{LC} = \omega\sqrt{\mu_s\varepsilon_s}. \tag{2.5}$$

And the phase and group velocities are given by

$$v_\phi = \frac{\omega}{\beta} = \frac{1}{\sqrt{LC}}, \tag{2.6}$$

$$v_g = \frac{1}{\frac{\partial\beta}{\partial\omega}} = \frac{1}{\sqrt{LC}}. \tag{2.7}$$

This shows that the phase and group velocities are equal and both positive and parallel. According to equation (2.5), the propagation constant, $\beta$, is positive; hence the phase lags in the direction of the positive group velocity in a right-handed material (RHM). Furthermore, the characteristic impedance of the network is equal to the equivalent wave impedance and can be expressed as

$$Z_0 = \sqrt{\frac{L}{C}} = \eta = \sqrt{\frac{\mu_s}{\varepsilon_s}} \ . \tag{2.8}$$

If we now consider a 2D distributed high-pass $L$-$C$ topology so that $Z = 1/j\omega C'$ and $Y = 1/j\omega L'$, then

$$\mu_s = -\frac{1}{\omega^2 C'}, \tag{2.9}$$

$$\varepsilon_s = -\frac{1}{\omega^2 L'}, \tag{2.10}$$

Since $L'$ and $C'$ are positive, a 2D distributed high-pass $L$-$C$ network can model a material with negative $\mu_s$ and $\varepsilon_s$. The corresponding propagation constant can be expressed as

$$\beta = -\sqrt{-ZY} = -\frac{1}{\omega\sqrt{L'C'}}, \tag{2.11}$$

which shows that it is inversely proportional to the frequency. Furthermore, the phase and group velocities can be yielded as

$$v_\phi = \frac{\omega}{\beta} = -\omega^2\sqrt{L'C'}\,, \tag{2.12}$$

$$v_g = \left(\frac{\partial\beta}{\partial\omega}\right)^{-1} = +\omega^2\sqrt{L'C'}\,. \tag{2.13}$$

The negative root in equation (2.11) is chosen to ensure that the group velocity is positive. This shows that the phase and group velocities are antiparallel, and according to equation (2.11), the propagation constant is negative; thus the phase leads in the direction of the positive group velocity in a left-handed material, known as backward wave. In addition, the characteristic impedance of the network is also equal to the equivalent wave impedance, and is given by

$$Z_0 = \sqrt{\frac{L'}{C'}} = \eta = \sqrt{\frac{\mu_s}{\varepsilon_s}}. \tag{2.14}$$

### 2.2.2 PERIODIC *L*-*C* LOADED TRANSMISSION-LINE NETWORK APPROACH

As discussed previously, the distributed *L*-*C* network in a high-pass configuration can be considered as a left-handed material, where permittivity and permeability are all negative, and can provide a backward wave performance. However, in practical realisation, the distributed *L*-*C* network must be implemented as a periodic network with nonvanishing physical dimensions [7]. The dimensions of a unit cell must be much smaller than one guide wavelength, so that it can be satisfied the homogeneity condition; therefore, this periodic structure can be considered distributed [10]. The practical 2D structure can be realised as a 2D host transmission lines network periodically loaded with lumped reactive elements [7] [24] as shown in Figure 2.8. The host transmission line has a characteristic impedance $Z_0$ and a propagation constant $k$, and provides the unit cell dimension $d$, so that it presents a total phase shift $\theta = kd$ along both directions. Furthermore, the host transmission lines load with discrete element components, series capacitors, $2C_0$ and a shunt inductor, $L_0$.

The practical 1D periodic left-handed material structure [9] [25] [26] is depicted in Figure 2.9. It can be used in the applications such as compact zero-degree phase shifters [9] and 1D power dividers [25] [26], and these applications are all based on the 1D infinite wavelength phenomenon.

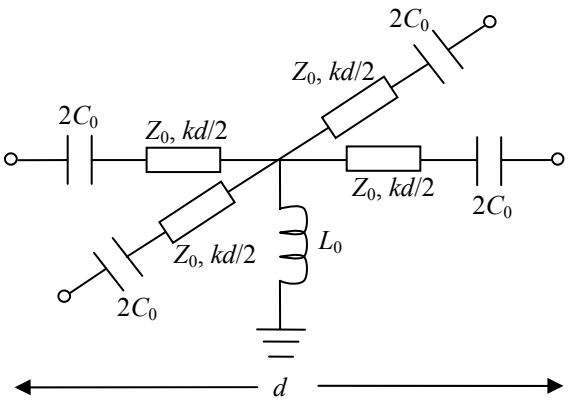


Fig. 2.8. Practical 2D unit cell for left-handed material.

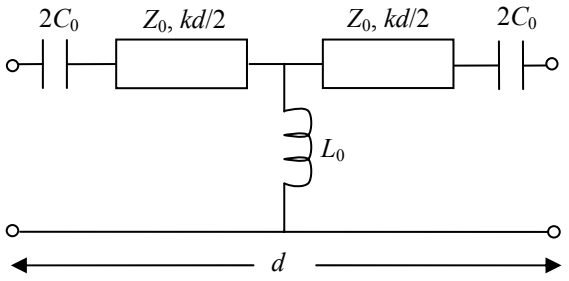


Fig. 2.9. Practical 1D unit cell for left-handed material.

# Chapter 3

# 20-WAY POWER DIVIDER USING METAMATERIAL

In this chapter, we describe in detail the square shaped 20-way power divider. In section 3.1, we present the important principles and structure of this power divider, and following we discuss the equivalent 1D model of the 2D unit cell in section 3.2. Finally, in section 3.3, we describe the design overview.

## 3.1 STRUCTURE AND PRINCIPLE

### 3.1.1 THE STRUCTURE OF THE TESSELLATED METAMATERIAL

As discussed in above chapter, the square shaped power divider has the output ports which are located on four straight lines, so that it is easier to integrate with or interconnect to power amplifiers in a parallel combined power amplifier. Figure 3.1 depicts a 5 by 5 version of the 2D structure which is the main part of the square shaped 20-way power divider [12]. This structure exhibits an infinite wavelength phenomenon in two-dimensions [13]. As shown in Figure 3.1, L and R are considered as square left-handed and right-handed unit cells, respectively. There are 12 left-handed unit cells and 13 right-handed unit cells which are placed in a checker-board tessellation. This structure is also called as the tessellated metamaterial (TMM). In the structure, right-handed unit cells are connected only to left-handed unit cells, and left-handed cells are connected only to right-handed cells. Port 0 is the input port, and it is connected to the central right-handed unit cell in the central point. Ports 1 to 20 are the peripheral output ports, which are located on a square shaped. Due to symmetry,

the couplings from port 0 to ports 1 to 20 can be separated into three groups:

$$S_{1,0} = S_{5,0} = S_{6,0} = S_{10,0} = S_{11,0} = S_{15,0} = S_{16,0} = S_{20,0}, \tag{3.1}$$

$$S_{2,0} = S_{4,0} = S_{7,0} = S_{9,0} = S_{12,0} = S_{14,0} = S_{17,0} = S_{19,0}, \tag{3.2}$$

$$S_{3,0} = S_{8,0} = S_{13,0} = S_{18,0}. \tag{3.3}$$

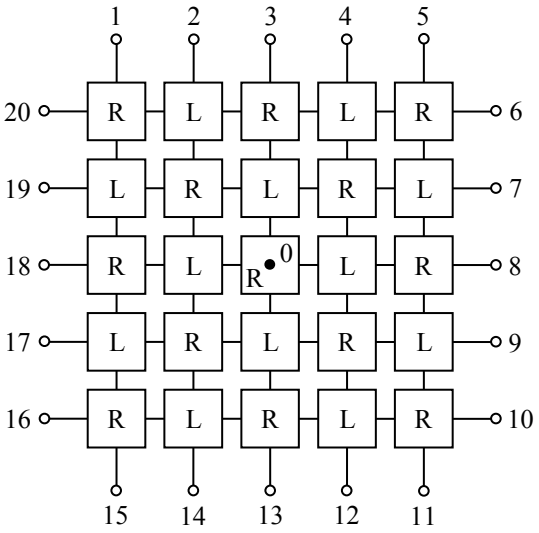


Fig. 3.1. 5 by 5 tessellated metamaterial (TMM) structure.

## 3.1.2 PRINCIPLE OF OPERATION BASED ON IDEAL TRANSMISSION LINES

If we use ideal transmission lines to realise the TMM structure, both left-handed and right-handed unit cells are comprised of four transmission lines which form a 4 port unit cell as shown in Figure 3.2. The 5$^{th}$ port is only in the central right-handed unit cell and is connected to the central point. All transmission lines have the same characteristic impedance $Z_0$, and, at the centre frequency, the insertion phase is $\varphi$ in a left-handed unit cell and is $-\varphi$ in a right-handed unit cell, where $\varphi$ is a positive phase angle. Therefore, the insertion phase between any two ports 1 to 4 is $2\varphi$ in a left-handed unit cell, and is $-2\varphi$ in a right-handed unit cell. Moreover, in the central right-handed unit cell, the insertion phase between port 5 and any port 1 to 4 is $-\varphi$.

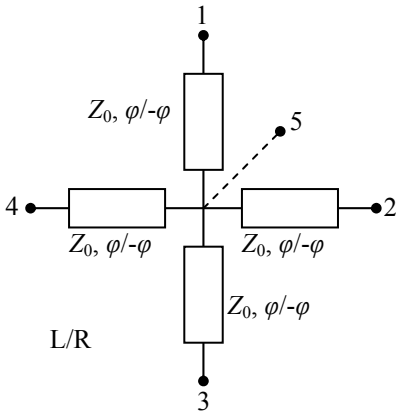


Fig. 3.2. 2D ideal left-handed or right-handed transmission line unit cell in TMM structure.

All unit cells have the same Bloch impedance $Z_0$, and they are matched to each other in the TMM structure. The output ports 1 to 20 in the TMM structure are matched to a termination with impedance which is equal to the Bloch impedance of the unit cell, $Z_0$. At the centre frequency, we can yield that the insertion phase between the input port 0 to an output port 1 to 20 is $-\varphi$ for ports of 1, 3, 5, 6, 8, 10, 11, 13, 15, 16, 18, 20, and is $\varphi$ for ports of 2, 4, 7, 9, 12, 14, 17, 19 [13]. This means that the phase angles of the couplings between the input and output ports are two alternating values which differ by $2\varphi$. Furthermore, power is identically divided to all peripheral ports, and the input impedance of the input port 0 is $Z_0/20$, where $Z_0$ is the Bloch impedance of the unit cell [13]. We can also see that the voltages at the central point of each unit cell have the equal magnitude and phase [13]. These concepts can be extended to an $N$-way TMM structure, where $N = 4n$ and $n$ is an odd integer, and the input impedance of the input port 0 will be $Z_0/N$ and the coupling between the input and output ports will be $1/2\sqrt{N}$ [13].

### 3.1.3 REALISATION USING REAL COMPONENTS

We use an example to demonstrate the behaviour of the TMM structure, which are operating at 1 GHz [13]. The right-handed unit cell shown in Figure 3.3 (b) consists of four conventional transmission lines with characteristic impedance, 100 Ω, and the length, 4.7 mm, and at 1 GHz the insertion phase of -5.65°. The structure of left-

handed unit cell is depicted in Figure 3.3 (a). To ensure $\varphi = 5.65°$ for the left-handed unit cell, we choose $L_0$ = 43.7 nH, $C_0$ = 4.37 pF and the four conventional transmission lines with characteristic impedance of 100 Ω, and the length of 4 mm, and at 1 GHz the insertion phase of -4.8°. The conventional transmission lines are all filled air dielectric.

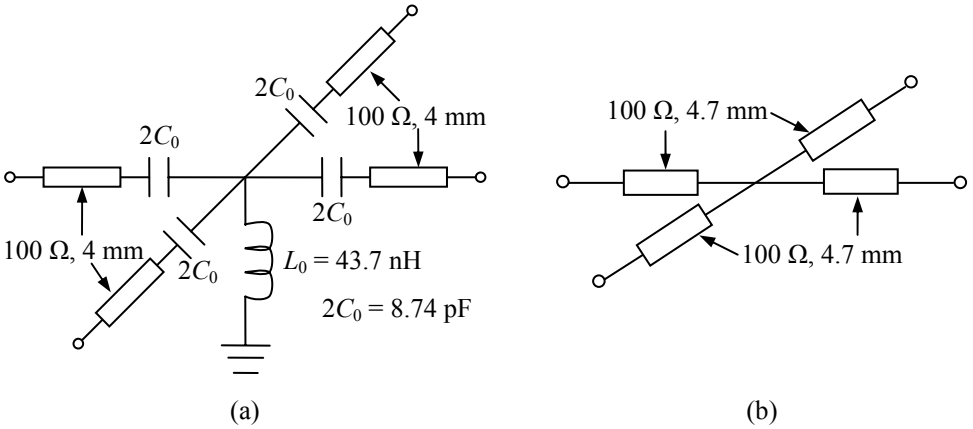


Fig. 3.3. The structure of 2D unit cell: (a) left-handed unit cell, and (b) right-handed unit cell.

Before proceeding it is instructive to consider the 1D equivalent circuits and their simulated S-parameter results as shown in Figure 3.4 and Figure 3.5. The values of the components are the same as those in the 2D unit cells of Figure 3.3. More detail about the equivalent 1D unit cells will be discussed in section 3.2. In Figure 3.4 (b), the simulated $S_{11}$ magnitude and $S_{21}$ phase are shown and the simulated $S_{21}$ magnitude is not shown because it is almost equal to 0 dB over the range from 0.6 GHz to 1.4 GHz. In Figure 3.5 (b), the simulated $S_{21}$ phase is only displayed, due to the simulated $S_{11}$ magnitude is below -100 dB and the simulated $S_{21}$ magnitude is nearly 0 dB. The simulation results show that the insertion phases of the 1D left-handed and right-handed unit cells are equal but with opposite sign at 1 GHz, and they are 11.3° ($2\varphi$) and -11.3° ($-2\varphi$), respectively.

### 3.1.3.1 THE INFINITE WAVELENGTH PHENOMENON IN TWO-DIMENSIONS

Figure 3.6 shows the branch circuit which connects two central nodes of two adjacent unit cells in the TMM structure, where one is left-handed unit cell and another one is

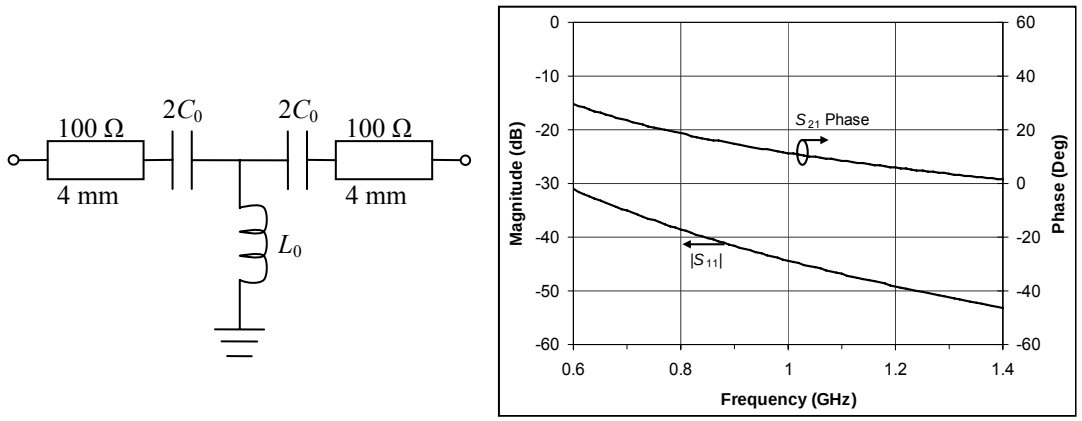


(a) (b)

Fig. 3.4. The equivalent 1D left-handed unit cell: (a) topology, and (b) the simulated S-parameters.

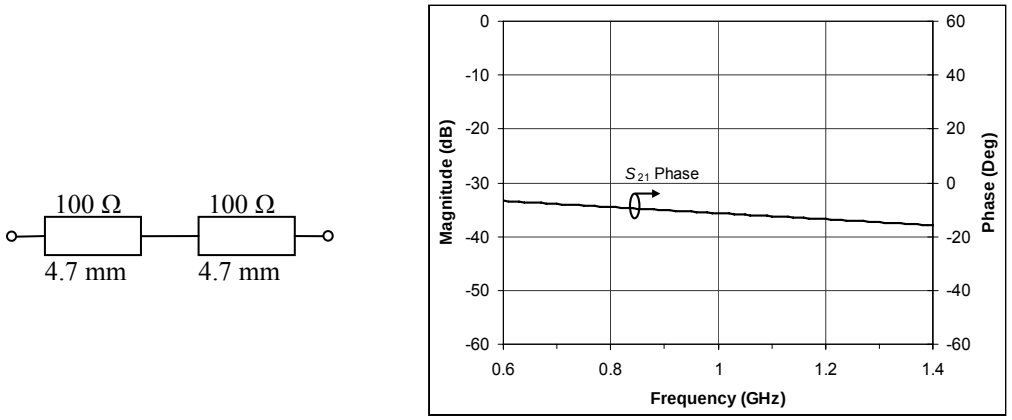


(a) (b)

Fig. 3.5. The equivalent 1D right-handed unit cell: (a) topology, and (b) the simulated S-parameters.

right-handed unit cell. Figure 3.7 shows the simulated ABCD parameters of this branch circuit. We can see that, at 1 GHz, $A$ and $D$ are equal to one, and $B$ and $C$ are equal to zero. This means that the branch circuit essentially behaves as a short circuit connecting the two adjacent central nodes at 1 GHz.

This result can also be obtained using the equivalent series inductances of two transmission lines. We have the equations

$$\beta = \omega\sqrt{LC} \tag{3.4}$$

$$Z_0 = \sqrt{\frac{L}{C}}, \tag{3.5}$$

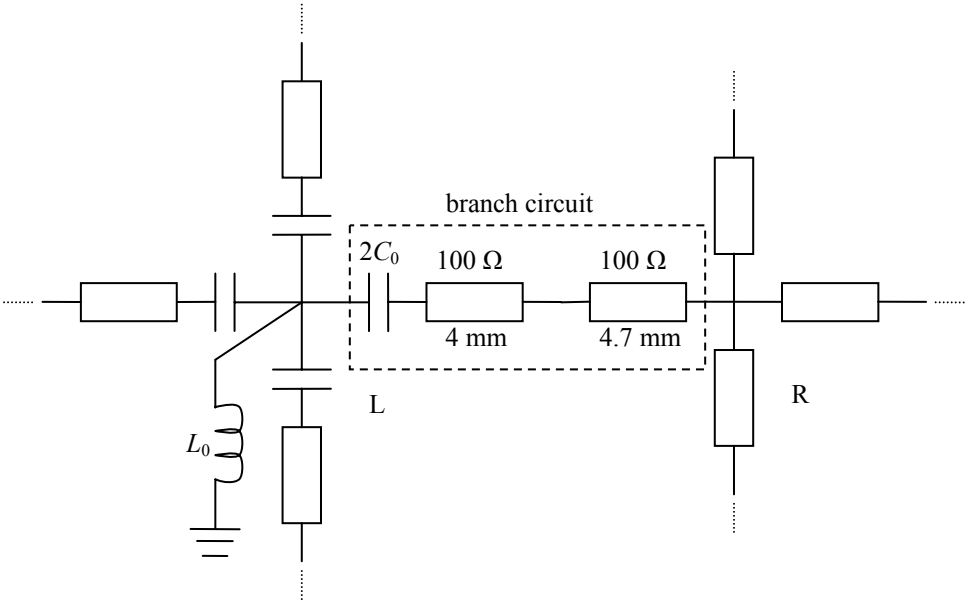


Fig. 3.6. The branch circuit connecting two central nodes of two adjacent unit cells.

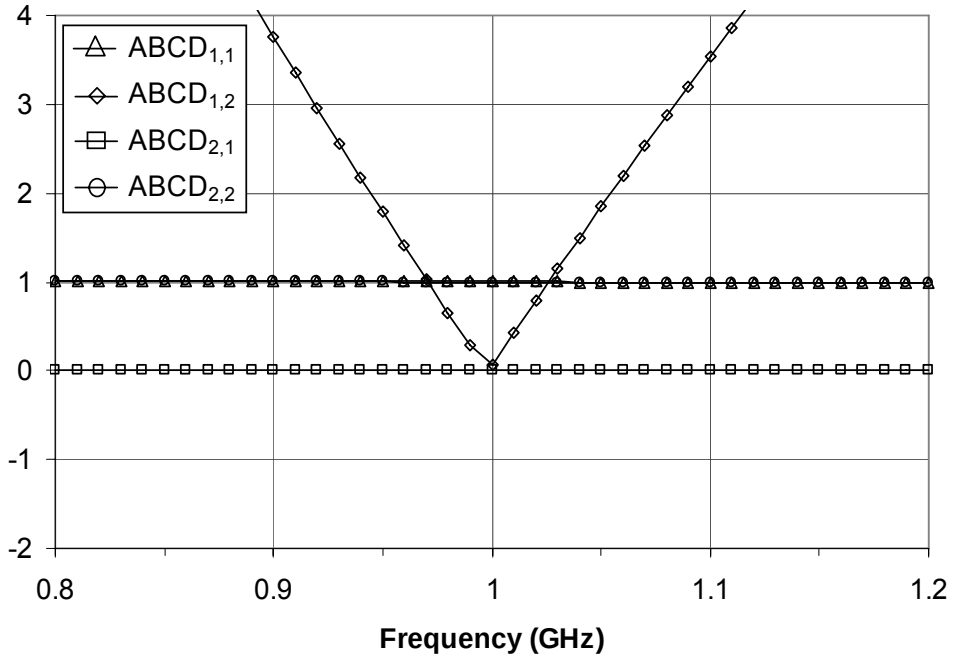


Fig. 3.7. The simulated ABCD parameters of the branch circuit.

where $\beta$ is the propagation constant, $Z_0$ is the characteristic impedance of the transmission line, and $L$ (H/m) and $C$ (F/m) are the equivalent series distributed inductance and shunt distributed capacitance of the transmission line, respectively. Then the equivalent series inductor can be yielded as

$$L_s = Ld = \frac{\beta Z_0}{\omega} d \,, \tag{3.6}$$

where $d$ is the length of the transmission line. Using equation (3.6), the equivalent series inductor of the transmission line, $L_s$, is equal to 1.33 nH for the left-handed cell, and is 1.57 nH for the right-handed cell. Figure 3.8 shows the branch circuit using the equivalent series inductors of two transmission lines. The resonant frequency of this branch circuit is calculated as $f = 1/2\pi\sqrt{LC}$ = 1 GHz. This also means that the branch circuit can be considered as a short circuit at 1 GHz.

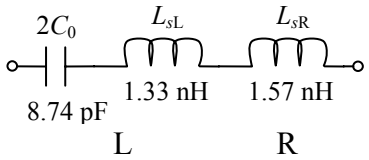


Fig. 3.8. The branch circuit using the equivalent series inductances of transmission lines.

As a result, when a plane wave propagates on the TMM structure, all central nodes of the unit cells will have the same voltage; thus, the TMM structure exhibits an infinite wavelength phenomenon in two-dimensions. The 17 by 17 TMM structure is simulated to show the spatial variation of voltages. The generator is connected at the central node of the central right-handed unit cell of the TMM structure, and the peripheral ports are terminated with 100 Ω, and voltage probes are inserted at the central nodes of each unit cell.

Figure 3.9 shows the spatial variation of the voltage across the TMM structure at 1 GHz. The step of contour in Figure 3.9 (b) is 0.2°. It is found that the voltage magnitude across the TMM structure varies 0.2 dB and the phase varies 2°. Therefore, the voltage across the TMM structure is almost constant, and the TMM structure displays an infinite wavelength phenomenon in two-dimensions.

For comparison, a 17 by 17 mosaic structure comprised of only right-handed unit cells is simulated, and the simulation results are shown in Figure 3.10. The step of contour in Figure 3.10 (a) is 2 dB, and the step of contour in Figure 3.10 (b) is 10°. The voltage magnitude across the structure varies 13.5 dB and the phase varies 207.6°. It is clear that the voltage across the structure varies significantly and this phenomenon is similar to cylindrical waves.

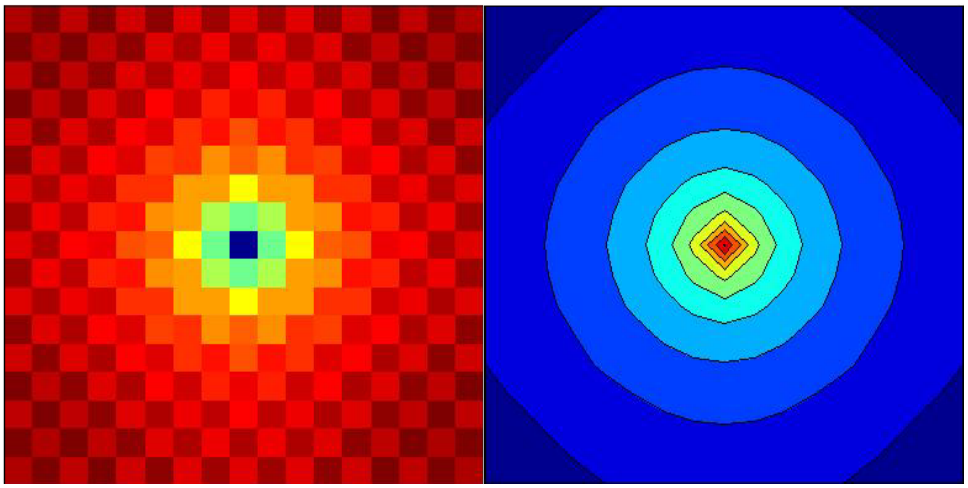

(a) (b)

Fig. 3.9. Voltage across the 17 by 17 TMM structure at 1 GHz: (a) magnitude with range 0.2 dB, and (b) phase with contours in steps of 0.2°.

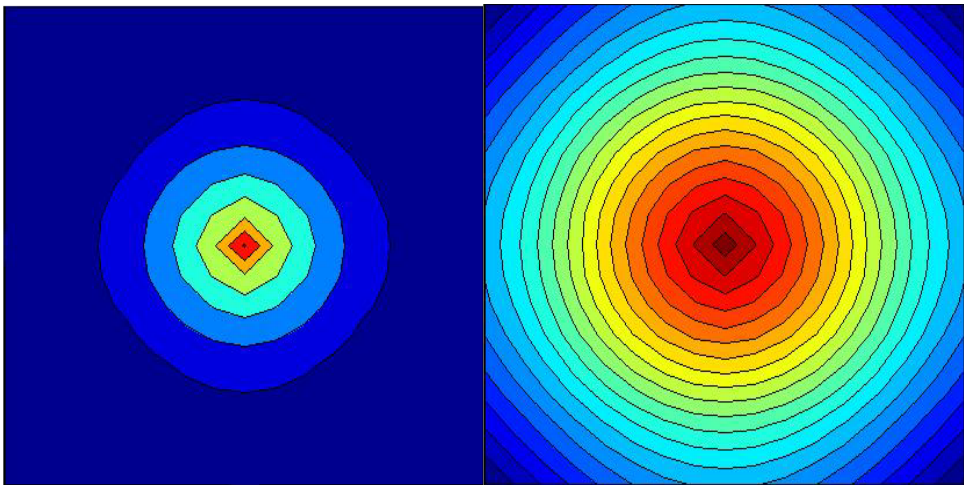

(a) (b)

Fig. 3.10. Voltage across the 17 by 17 mosaic structure comprised of only right-handed unit cells at 1 GHz: (a) magnitude with contours in steps of 2 dB, and (b) phase with contours in steps of 10°.

### 3.1.3.2 THE SIMULATION OF THE 5 BY 5 TMM STRUCTURE

We now consider the simulations of the 5 by 5 TMM structure as shown in Figure 3.1, and the 5 by 5 mosaic structure comprised of only right-handed unit cells for comparison. Figure 3.11 shows the simulated frequency responses of S-parameters of the 5 by 5 TMM structure. The reference impedance of S-parameter is 5 Ω at input port 0, and 100 Ω at output ports 1 to 20. The simulation results show that the TMM structure works as expected at 1 GHz: it divides power equally to 20 output ports, where the coupling magnitude between the input and output ports is -13.1 dB which is favourable compared to the theoretical value of -13 dB, and the coupling phases differ by 0° or 11.3°, which is consistent with the simulation results of the 1D models shown in Figure 3.4 and Figure 3.5. The coupling magnitudes across the range from 0.8 GHz to 1.2 GHz are almost same and flat, and the corresponding coupling phases differ less than 16.3°.

Figure 3.12 shows the simulated frequency responses of S-parameters of the 5 by 5 mosaic structure comprised of only right-handed unit cells which are the same as the right-handed unit cell in the TMM structure. The best match at input port was obtained when the reference impedance of input port became 5.7-j 6.4 Ω. The performance of this structure is similar to a parallel plate waveguide excited in the centre point as discussed above, so it can explains why the reference impedance of input port is complex [27]. The coupling magnitudes across the range from 0.8 GHz to 1.2 GHz are an equal value of -13 dB, and the difference of coupling phases is 18° at 1 GHz and less than 21.6° over this range. It is apparent that the TMM structure displays a better performance than the mosaic structure using only right-handed unit cells.

It is interesting to consider a 5 by 5 mosaic structure comprised of only right-handed unit cells where the insertion phases of four transmission lines are -180° at 1 GHz. Thus, the size of the right-handed unit cell is one wavelength at 1 GHz. The simulated frequency response is shown in Figure 3.13. It is observed that the excellent match is obtained at 1 GHz, but the bandwidth is very narrow and the size of the structure is very large, 5$\lambda$ by 5$\lambda$. Although, the high dielectric constant substrate and meandering of transmission lines can be used, the structure will be larger than the

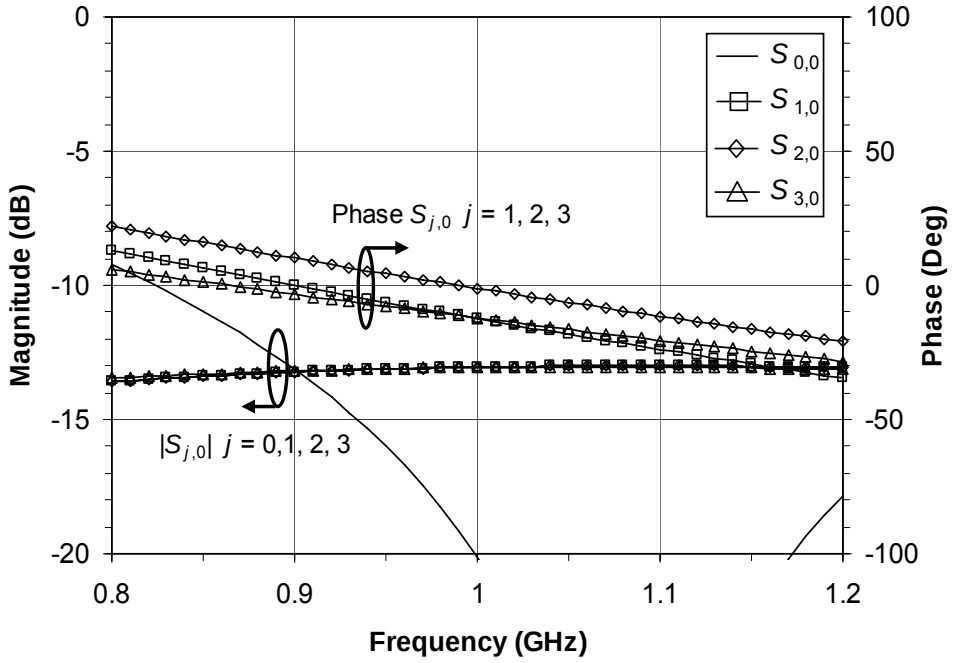


Fig. 3.11. S-parameters of 5 by 5 TMM structure.

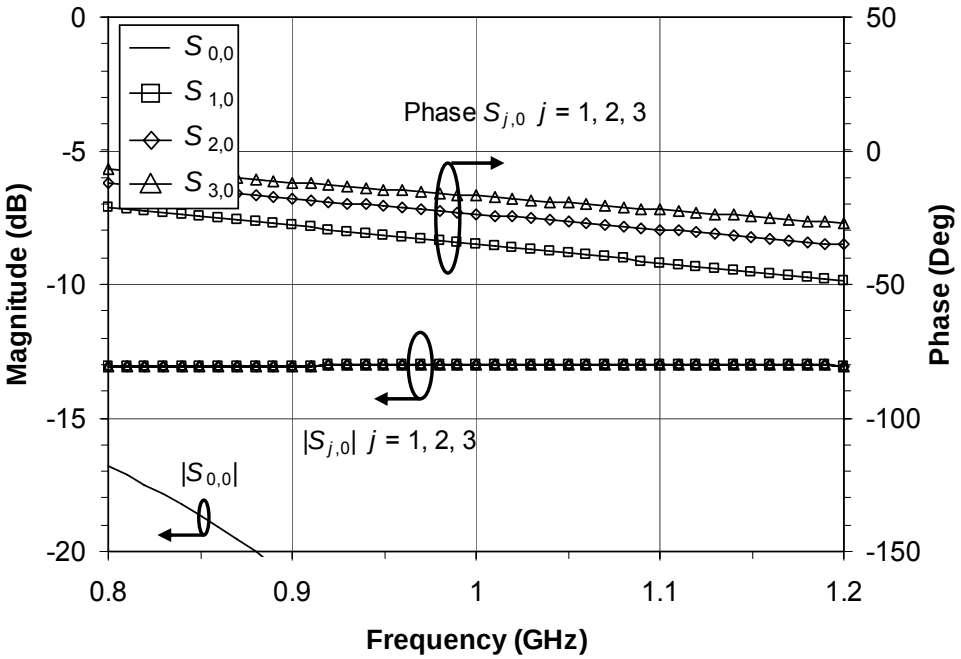


Fig. 3.12. S-parameters of 5 by 5 mosaic structure comprised only right-handed unit cells.

TMM structure which is only 0.16$\lambda$ by 0.16$\lambda$.

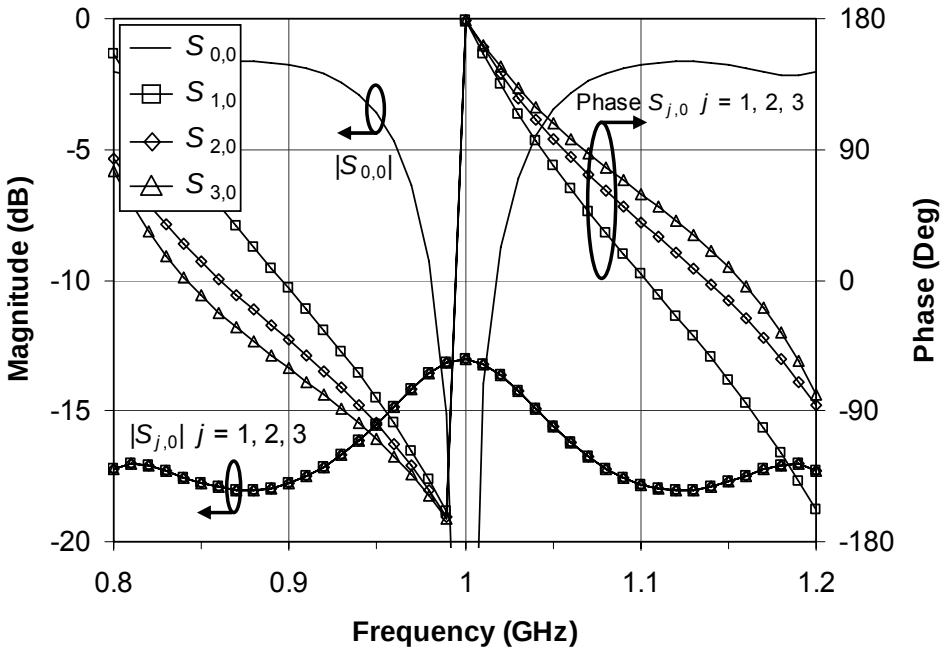


Fig. 3.13. S-parameters of 5 by 5 mosaic structure of 360° right-handed unit cells.

## 3.2 THE EQUIVALENT 1D MODEL OF 2D UNIT CELL

To design the 2D left-handed and right-handed unit cells, it is of interest to consider their equivalent 1D model for the TMM structure. We simulate a 25 by 17 TMM structure as being representative of a large TMM structure, as shown in Figure 3.14, where L and R denote the left-handed and right-handed unit cell, respectively. The plane wave propagates in the longitudinal direction as the arrows shown in Figure 3.14, and the structure is terminated with loads in the longitudinal direction, but it is opened on the two sides of the transverse direction, where the unit cells located on the top and bottom sides remove the opened stubs. The lines of sources connected to the left edge of the TMM structure are properly phased so that a plane wave is launched into the TMM structure. There are two types of 1D model: one is shown in Figure 3.15 [7], where the unit cells have two opened stubs in the transverse direction and the wave propagates in the longitudinal direction; and the other is the 1D line model

without the transverse stubs as shown in Figure 3.16. We will discuss which 1D model is the best model for the TMM structure.

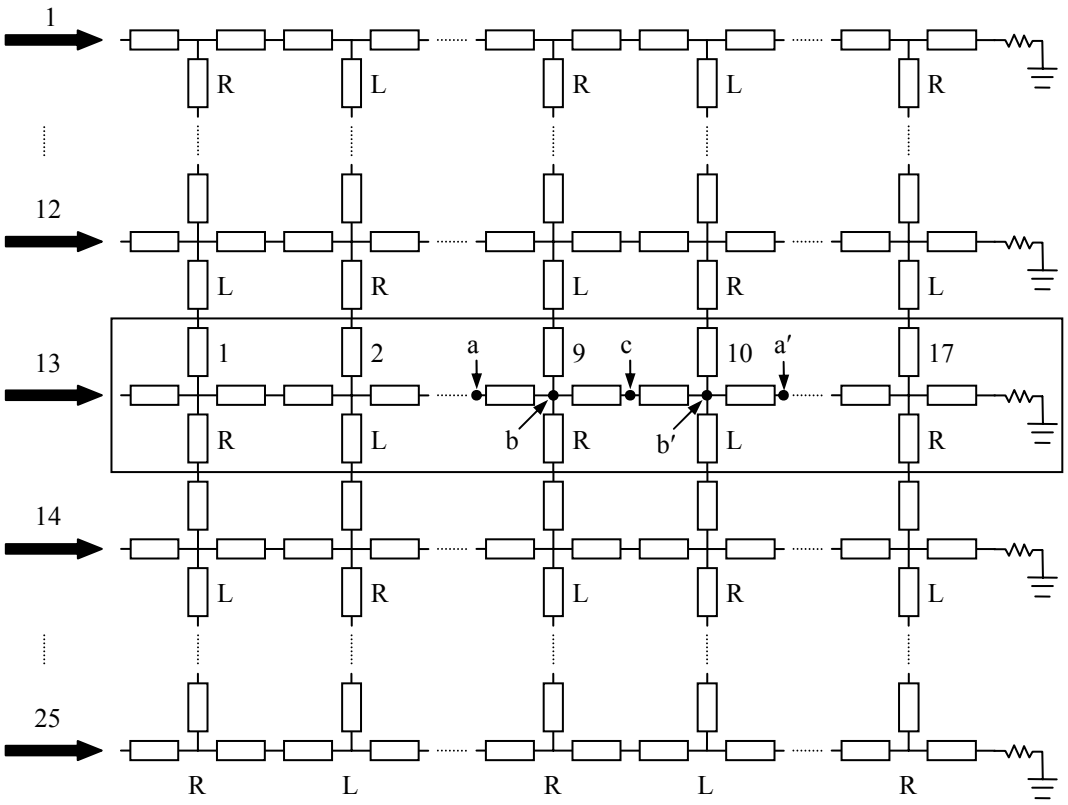


Fig. 3.14. The 25 by 17 TMM structure with the wave propagated in the longitudinal direction, where the arrows show the direction of the plane wave.

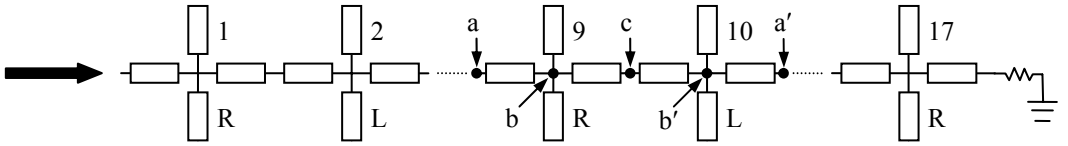


Fig. 3.15. The 1D model with opened transverse stubs [7], where the arrow shows the direction of the plane wave.

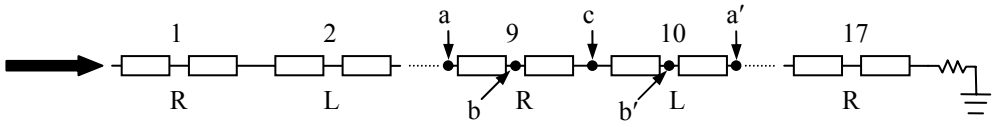


Fig. 3.16. The 1D line model without the transverse stubs, where the arrow shows the direction of the plane wave.

### 3.2.1 2D RIGHT-HANDED STRUCTURES USING IDEAL TRANSMISSION LINES

First, we consider the homogeneous structures which comprise only right-handed unit cells and are similar to the Figure 3.14, Figure 3.15 and Figure 3.16. The right-handed unit cell is based upon ideal transmission lines as shown in Figure 3.2, where we choose $Z_0$ is 100 Ω and $\varphi$ is 5.65° at 1 GHz. Figure 3.17 shows the currents and voltages in the central right-handed unit cell (No.9) of the 25 by 17 mosaic structure using only right-handed cells. Figure 3.18 and Figure 3.19 show the currents and voltages in the central right-handed unit cells (No.9) of the two different 1D models comprised of only right-handed cells, respectively. It can be seen that the currents and voltages in the central right-handed unit cell of the 1D model shown as Figure 3.15 are consistent with those in the mosaic structure shown as Figure 3.14. This means that the 1D model with opened transverse stubs is a good equivalent model for the 2D mosaic homogeneous structure comprised of entire right-handed unit cells. Table 3.1 and Table 3.2 summarise the currents and voltages in the central right-handed cells of these three structures at 1 GHz, respectively. Moreover, if we repeat the simulations using the left-handed unit cell to replace the right-handed unit cell, we can also obtain the similar results [7].

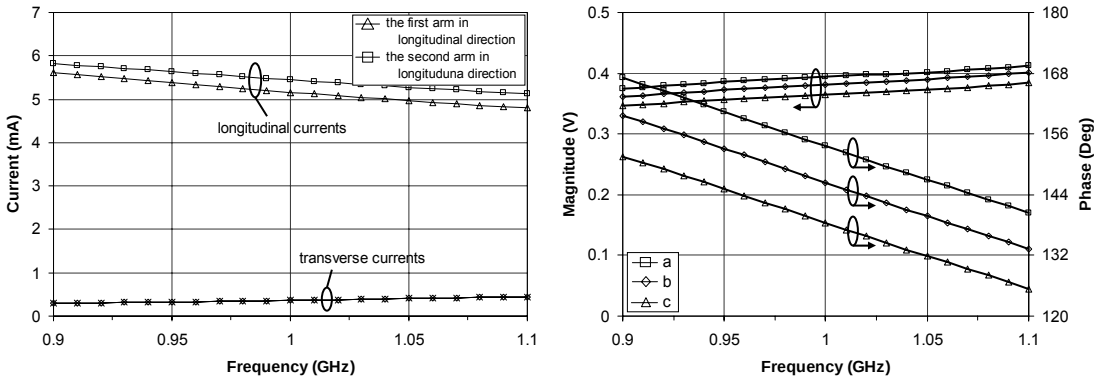


(a) (b)

Fig. 3.17. Simulated currents and voltages of the central right-handed unit cell (No.9) in mosaic structure: (a) currents, and (b) three nodes (a, b, and c) voltages.

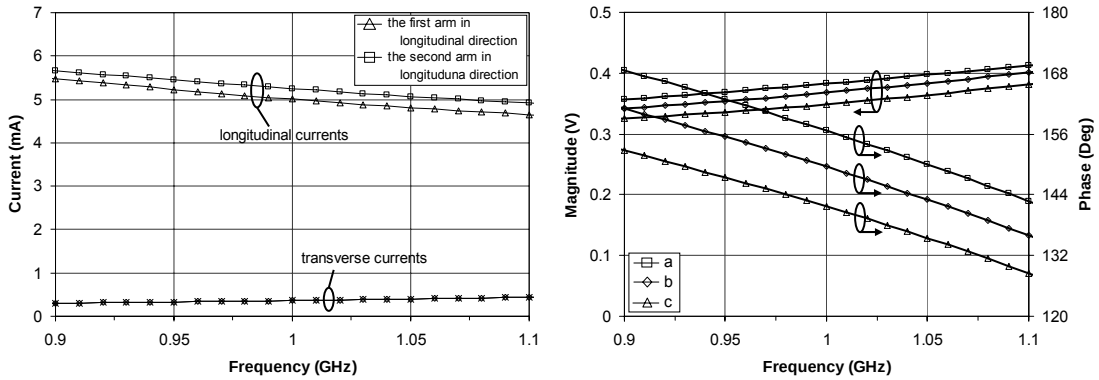


(a) (b)

Fig. 3.18. Simulated currents and voltages of the central right-handed unit cell (No.9) in the 1D model shown as Fig. 3.15: (a) currents, and (b) three nodes (a, b, and c) voltages.

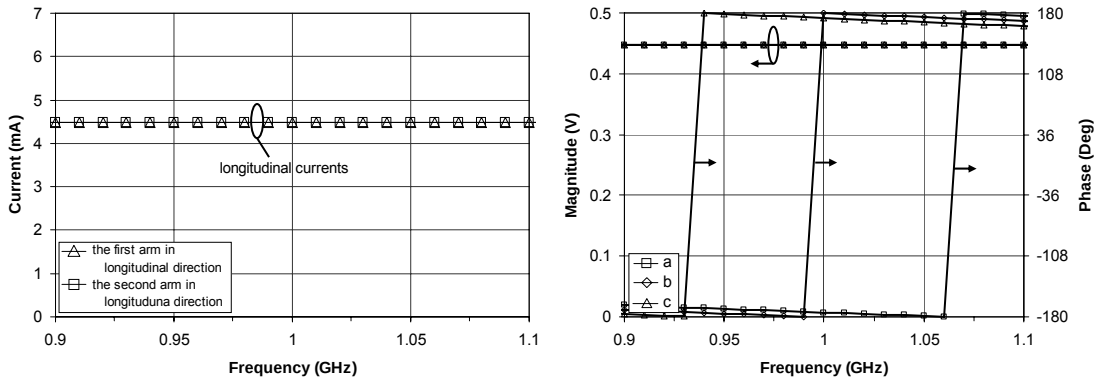


(a) (b)

Fig. 3.19. Simulated currents and voltages of the central right-handed unit cell (No.9) in the 1D model shown as Fig. 3.16: (a) currents, and (b) three nodes (a, b, and c) voltages.

| | Longitudinal currents | | Transverse currents |
|---|---|---|---|
| | First arm | Second arm | |
| Mosaic structure | 5.16 mA | 5.45 mA | 0.36 mA |
| 1D model shown as Fig. 3.15 | 5 mA | 5.25 mA | 0.36 mA |
| 1D model shown as Fig. 3.16 | 4.47 mA | 4.47 mA | / |

Table 3.1. The currents in the central right-handed cells of three different structures at 1 GHz.

| | Voltages | | | | | |
|---|---|---|---|---|---|---|
| | a | | b | | c | |
| | Magnitude | Phase | Magnitude | Phase | Magnitude | Phase |
| Mosaic structure | 0.39 V | 153.58° | 0.38 V | 146.36° | 0.37 V | 138.41° |
| 1D model shown as Fig. 3.15 | 0.38 V | 156.63° | 0.37 V | 149.52° | 0.35 V | 141.71° |
| 1D model shown as Fig. 3.16 | 0.45 V | -174.8° | 0.45 V | 179.6° | 0.45 V | 173.9° |

Table 3.2. The voltages in the central right-handed cells of three different structures at 1 GHz.

### 3.2.2 TMM STRUCTURE USING IDEAL TRANSMISSION LINES

We now use the model based upon ideal transmission lines as shown in Figure 3.2 to describe the left-handed and right-handed unit cells in the TMM structure, where we also choose $Z_0$ is 100 Ω and $\varphi$ is 5.65° at 1 GHz. Figure 3.20 shows the longitudinal and transverse currents of the right-handed (No.9) and left-handed (No.10) unit cells in the centre of the TMM structure shown in Figure 3.14. It is found that, at 1 GHz, in both cells the longitudinal currents are equal to 4.47 mA and the transverse currents are equal to 0.0002 mA, which are almost zero and very small compared to the longitudinal currents. Therefore, the transverse currents can be neglected, and this means that currents would only flow in the longitudinal direction and not in the transverse direction; thus, the transverse arms can be ignored. Figure 3.21 and Figure 3.22 show the longitudinal and transverse currents of the right-handed (No.9) and left-handed (No.10) unit cells of the 1D structures shown in Figure 3.15 and Figure 3.16, respectively. In the 1D model shown in Figure 3.15, at 1 GHz, in both cells the longitudinal currents are equal to 4.54 mA or 4.45 mA, and the transverse currents are equal to 0.44 mA, which over-estimate the transverse currents for the TMM structure. In the 1D model shown in Figure 3.16, the longitudinal currents are equal to 4.47 mA at 1 GHz in both cells, and the transverse currents are not present due to the absence

of the transverse stubs. All the currents at 1 GHz are summarised in Table 3.3. Therefore, according to the currents, the 1D line model without the transverse stubs shown in Figure 3.16 provides a good model for the TMM structure.

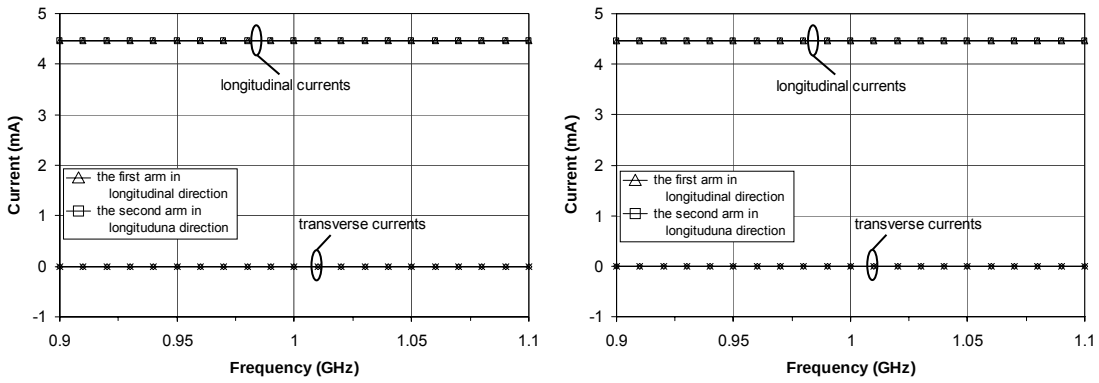


(a) (b)

Fig. 3.20. Simulated longitudinal and transverse currents in the TMM structure of Fig. 3.14: (a) right-handed cell (No.9), and (b) left-handed cell (No.10).

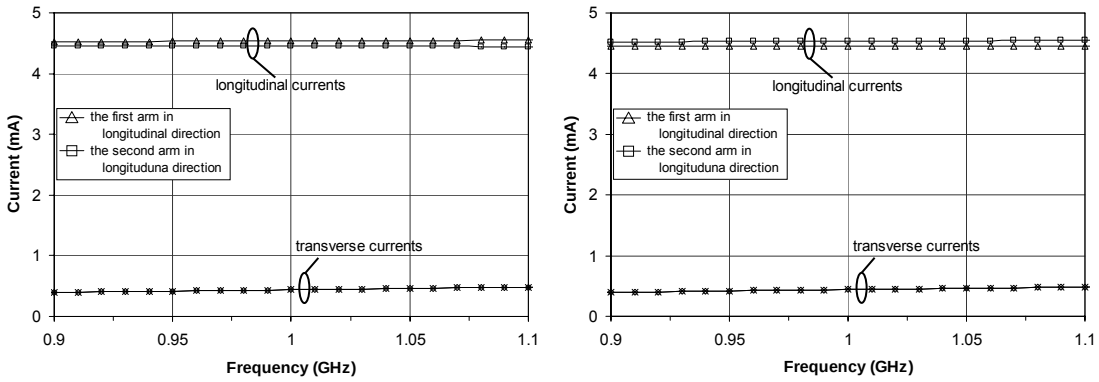


(a) (b)

Fig. 3.21. Simulated longitudinal and transverse currents in the 1D model with opened transverse stubs of Fig. 3.15: (a) right-handed cell (No.9), and (b) left-handed cell (No.10).

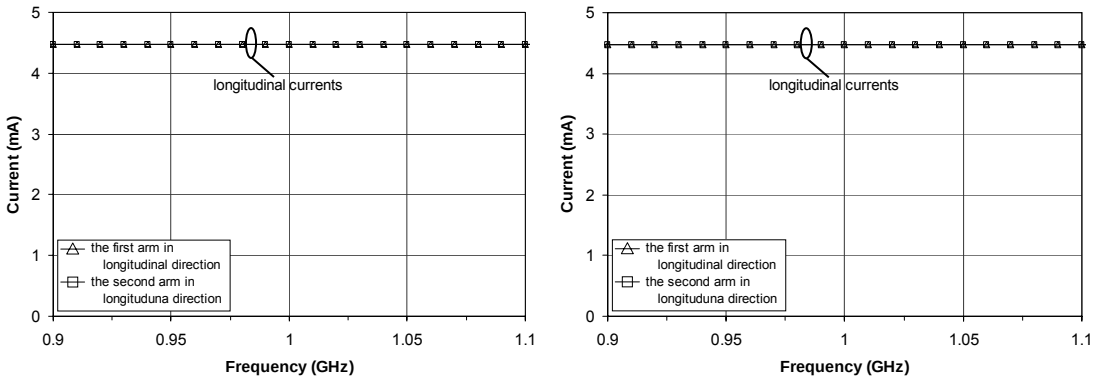


(a) (b)

Fig. 3.22. Simulated currents in the 1D model without transverse stubs of Fig. 3.16: (a) right-handed cell (No.9), and (b) left-handed cell (No.10).

| | Longitudinal currents | | | | Transverse currents | |
|---|---|---|---|---|---|---|
| | RH unit cell (No.9) | | LH unit cell (No.10) | | RH unit cell (No.9) | LH unit cell (No.10) |
| | First arm | Second arm | First arm | Second arm | | |
| TMM | 4.47 mA | 4.47 mA | 4.47 mA | 4.47 mA | 0.0002 mA | 0.0002 mA |
| 1D model shown in Fig. 3.15 | 4.54 mA | 4.45 mA | 4.45 mA | 4.54 mA | 0.44 mA | 0.44 mA |
| 1D model shown in Fig. 3.16 | 4.47 mA | 4.47 mA | 4.47 mA | 4.47 mA | / | / |

Table 3.3. The currents of three different structures at 1 GHz.

This conclusion can also be established according to the voltages. Figure 3.23 shows the three nodes (a, b and c) voltages of the central right-handed unit cell (No.9) and the three nodes (c, b′ and a′) voltages of the left-handed unit cell (No.10) in the TMM structure shown in Figure 3.14. Figure 3.24 and Figure 3.25 show the three nodes (a, b and c) voltages of the central right-handed unit cell (No.9) and the three nodes (c, b′ and a′) voltages of the left-handed unit cell (No.10) for the two different 1D models. These voltages at 1 GHz are summarised in Table 3.4 and Table 3.5. It is clear that the voltages in both unit cells of the 1D model shown in Figure 3.16 are consistent with the results of the TMM structure. Therefore, according to voltages, the 1D line model without the transverse stubs can be considered as a good model for the TMM structure.

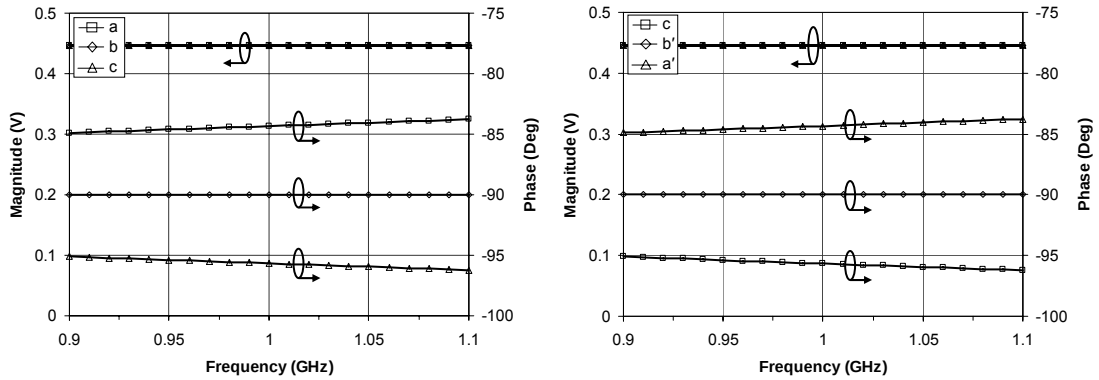


(a) (b)

Fig. 3.23. Simulated voltages in the TMM structure of Fig. 3.14: (a) right-handed cell (No.9) at three nodes (a, b, c), and (b) left-handed cell (No.10) at three nodes (c, b′, a′).

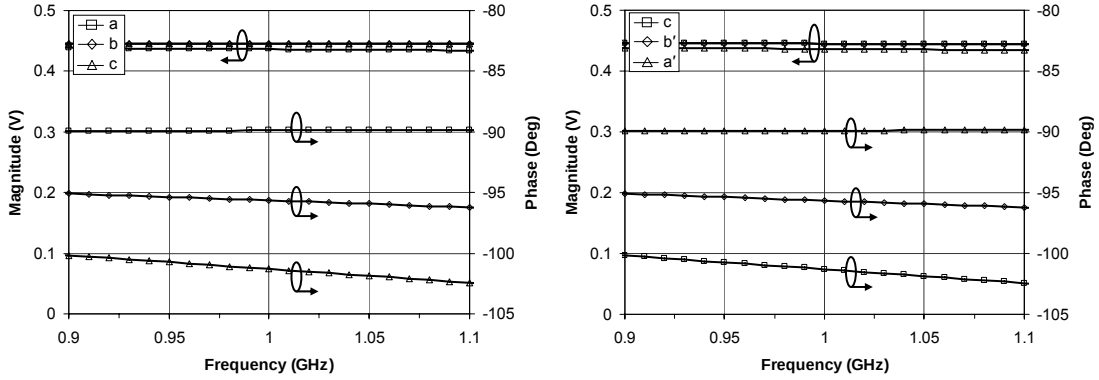


(a) (b)

Fig. 3.24. Simulated voltages in the 1D model of Fig. 3.15: (a) right-handed cell (No.9) at three nodes (a, b, c), and (b) left-handed cell (No.10) at three nodes (c, b′, a′).

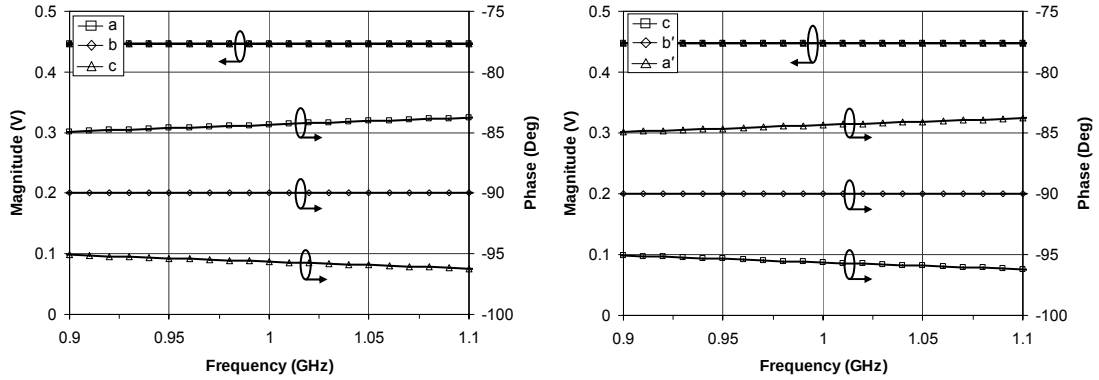


(a) (b)

Fig. 3.25. Simulated voltages in the 1D model of Fig. 3.16: (a) right-handed cell (No.9) at three nodes (a, b, c), and (b) left-handed cell (No.10) at three nodes (c, b′, a′).

| | Voltages | | | | | |
|---|---|---|---|---|---|---|
| | a | | b | | c | |
| | Magnitude | Phase | Magnitude | Phase | Magnitude | Phase |
| TMM | 0.45 V | -84.33° | 0.45 V | -90° | 0.45 V | -95.66° |
| 1D model of Fig. 3.15 | 0.44 V | -89.89° | 0.45 V | -95.65° | 0.45 V | -101.3° |
| 1D model of Fig. 3.16 | 0.45 V | -84.35° | 0.45 V | -90° | 0.45 V | -95.65° |

Table 3.4. The voltages in the central right-handed cells (No.9) of three different structures at 1 GHz.

| | Voltages | | | | | |
|---|---|---|---|---|---|---|
| | c | | b′ | | a′ | |
| | Magnitude | Phase | Magnitude | Phase | Magnitude | Phase |
| TMM | 0.45 V | -95.66° | 0.45 V | -90° | 0.45 V | -84.34° |
| 1D model of Fig. 3.15 | 0.45 V | -101.3° | 0.45 V | -95.65° | 0.44 V | -89.89° |
| 1D model of Fig. 3.16 | 0.45 V | -95.65° | 0.45 V | -90° | 0.45 V | -84.35° |

Table 3.5. The voltages in the left-handed cells (No.10) of three different structures at 1 GHz.

### 3.2.3 TMM STRUCTURE USING REALISATION MODELS

We now consider the simulations which are repeated using the realisations of the 2D left-handed and right-handed unit cells, which are discussed in the section 3.1 and are shown in Figure 3.3. We will refer to Figure 3.14, Figure 3.15 and Figure 3.16 in this section noting that the left-handed unit cells of Figure 3.14 and Figure 3.15 use the topology in Figure 3.3 (a) whilst the 1D left-handed unit cells of Figure 3.16 use the topology in Figure 3.4 (a).

Figure 3.26 shows the longitudinal and transverse currents in the right-handed (No.9) and left-handed (No.10) unit cells of the TMM structure. The transverse currents are 0.34 mA in the left-handed unit cell, and 0.1 mA in the right-handed unit cell, at 1 GHz. It is clear that, in both unit cells, the transverse currents are very small compared to the longitudinal currents. Figure 3.27 and Figure 3.28 show the longitudinal and transverse currents in the right-handed (No.9) and left-handed (No.10) unit cells of the two different 1D models, respectively. All currents in the right-handed (No.9) and left-handed (No.10) unit cells of these three structures at 1 GHz are summarised in Table 3.6. We can see that, according to currents, although there are the differences between the results of the 1D model shown in Figure 3.15 and the TMM structure, the results of the 1D model shown in Figure 3.15 are much closer to those of the TMM structure, compared to the 1D model shown in Figure 3.16. We also consider the voltages. Figure 3.29, Figure 3.30 and Figure 3.31 show the three nodes (a, b and c) voltages of the central right-handed unit cell (No.9) and the three nodes (c, b′ and a′) voltages of the left-handed unit cell (No.10) in the TMM structure and the two different 1D models, respectively. These voltages at 1 GHz are summarised in Table 3.7 and Table 3.8. It is clear that, in both unit cells, the voltages in the 1D model shown in Figure 3.15 are much closer to those in the TMM structure, compared to the 1D model shown in Figure 3.16. Therefore, the 1D model with opened transverse stubs seems to be a good model for the TMM structure.

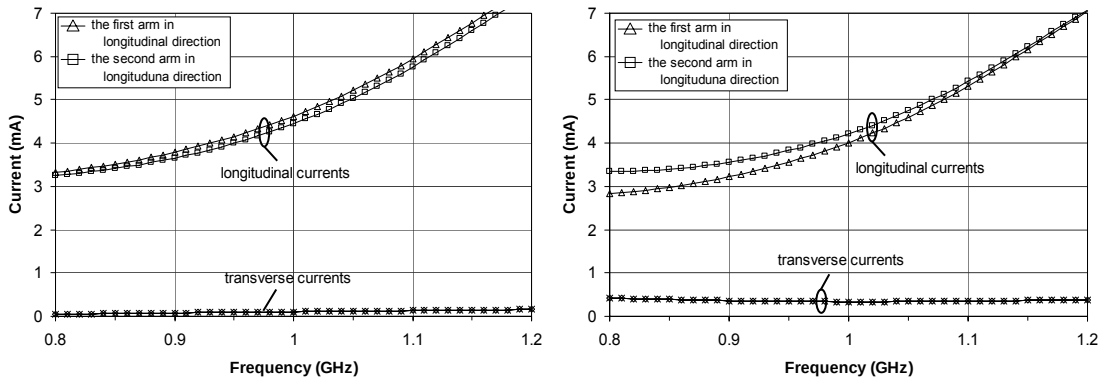


(a) (b)

Fig. 3.26. Simulated longitudinal and transverse currents in the TMM structure of Fig. 3.14: (a) right-handed cell (No.9), and (b) left-handed cell (No.10).

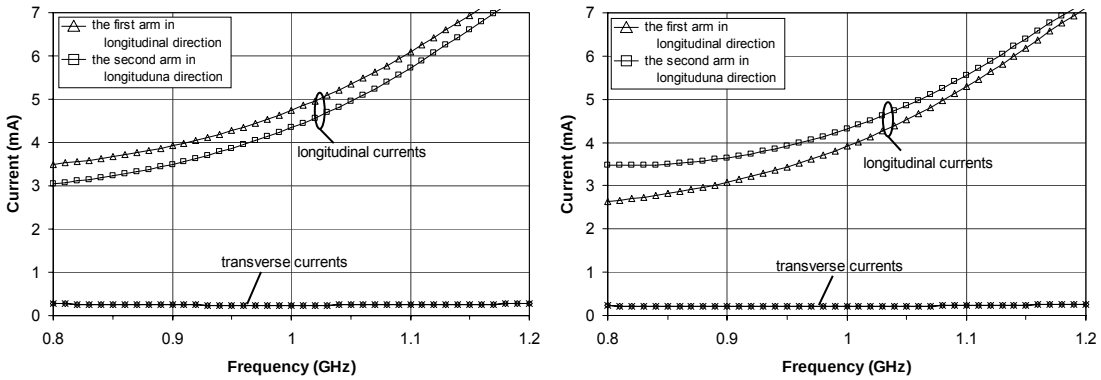


(a) (b)

Fig. 3.27. Simulated longitudinal and transverse currents in the 1D model of Fig. 3.15: (a) right-handed cell (No.9), and (b) left-handed cell (No.10).

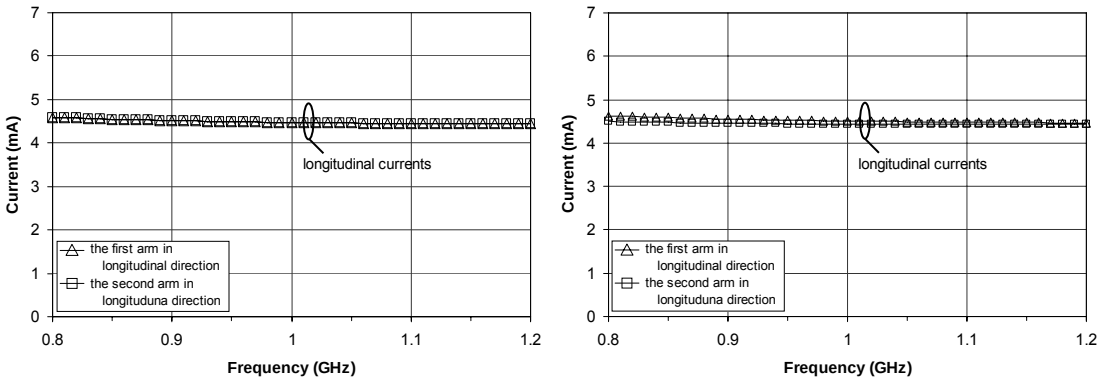


(a) (b)

Fig. 3.28. Simulated currents in the 1D model of Fig. 3.16: (a) right-handed cell (No.9), and (b) left-handed cell (No.10).

| | Longitudinal currents | | | | Transverse currents | |
|---|---|---|---|---|---|---|
| | RH unit cell (No.9) | | LH unit cell (No.10) | | RH unit cell (No.9) | LH unit cell (No.10) |
| | First arm | Second arm | First arm | Second arm | | |
| TMM | 4.62 mA | 4.45 mA | 4.01 mA | 4.22 mA | 0.1 mA | 0.34 mA |
| 1D model shown in Fig. 3.15 | 4.74 mA | 4.34 mA | 3.91 mA | 4.31 mA | 0.24 mA | 0.21 mA |
| 1D model shown in Fig. 3.16 | 4.47 mA | 4.47 mA | 4.51 mA | 4.44 mA | / | / |

Table 3.6. The currents of three different structures at 1 GHz.

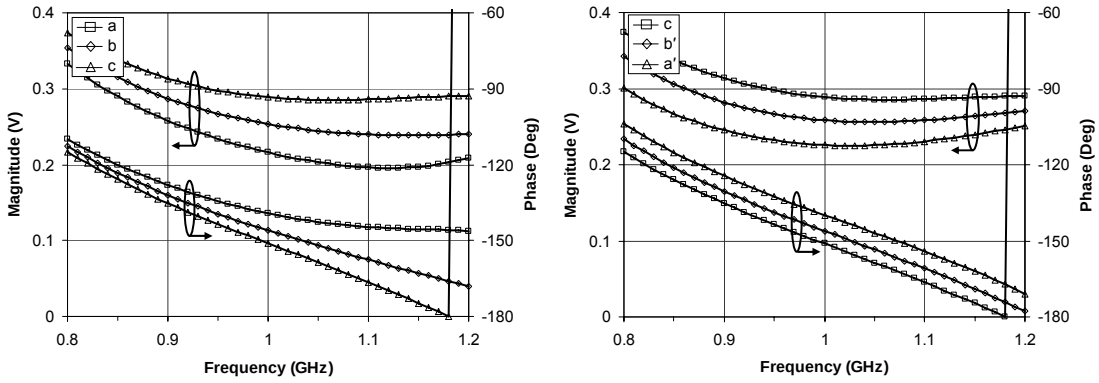


(a) (b)

Fig. 3.29. Simulated voltages in the TMM structure of Fig. 3.14: (a) right-handed cell (No.9) at three nodes (a, b, c), and (b) left-handed cell (No.10) at three nodes (c, b′, a′).

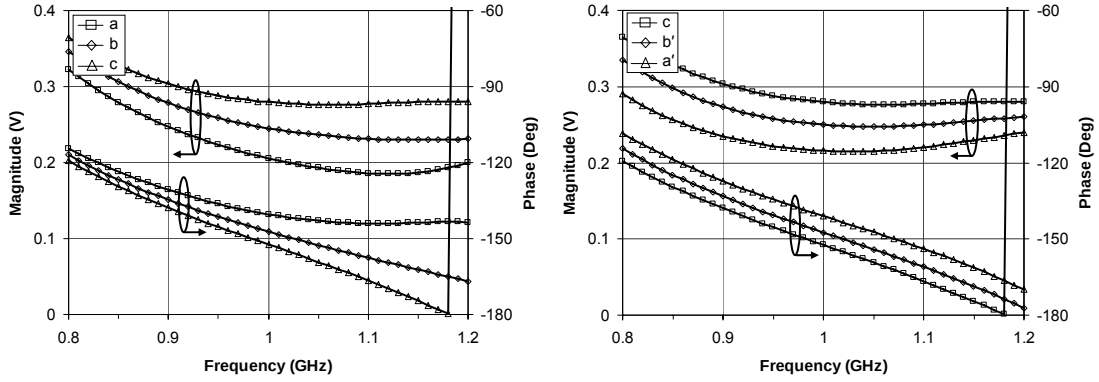


(a) (b)

Fig. 3.30. Simulated voltages in the 1D model of Fig. 3.15: (a) right-handed cell (No.9) at three nodes (a, b, c), and (b) left-handed cell (No.10) at three nodes (c, b′, a′).

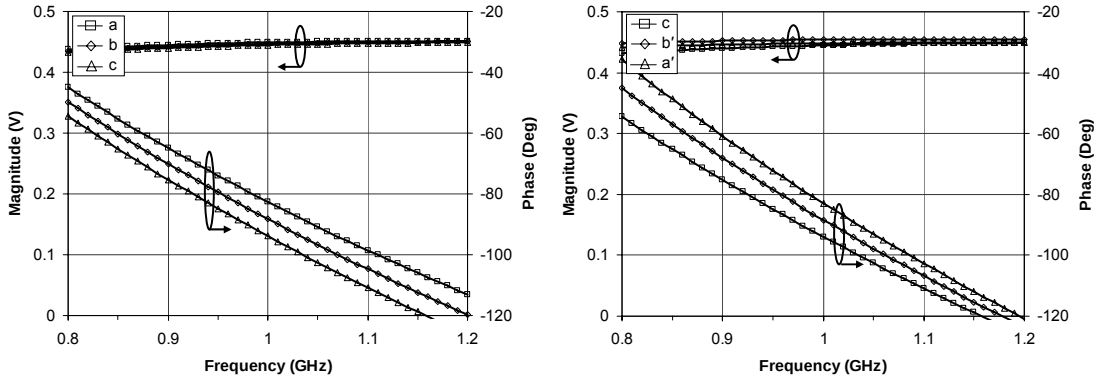


(a) (b)

Fig. 3.31. Simulated voltages in the 1D model of Fig. 3.16: (a) right-handed cell (No.9) at three nodes (a, b, c), and (b) left-handed cell (No.10) at three nodes (c, b′, a′).

| | Voltages | | | | | |
|---|---|---|---|---|---|---|
| | a | | b | | c | |
| | Magnitude | Phase | Magnitude | Phase | Magnitude | Phase |
| TMM | 0.22 V | -139.2° | 0.25 V | -146.1° | 0.29 V | -151.1° |
| 1D model of Fig. 3.15 | 0.21 V | -140.3° | 0.25 V | -147.3° | 0.28 V | -152.3° |
| 1D model of Fig. 3.16 | 0.45 V | -82.63° | 0.45 V | -88.24° | 0.44 V | -93.91° |

Table 3.7. The voltages in the central right-handed cells (No.9) of three different structures at 1 GHz.

| | Voltages | | | | | |
|---|---|---|---|---|---|---|
| | c | | b′ | | a′ | |
| | Magnitude | Phase | Magnitude | Phase | Magnitude | Phase |
| TMM | 0.29 V | -151.1° | 0.26 V | -146.2° | 0.23 V | -139.8° |
| 1D model of Fig. 3.15 | 0.28 V | -152.3° | 0.25 V | -147.4° | 0.22 V | -141° |
| 1D model of Fig. 3.16 | 0.44 V | -93.91° | 0.45 V | -88.37° | 0.45 V | -82.87° |

Table 3.8. The voltages in the left-handed cells (No.10) of three different structures at 1 GHz.

### 3.2.4 TMM STRUCTURE USING REALISATION MODELS WITH 4 PLANE WAVES

We can see that the conclusion in section 3.2.3 is different from the conclusion in section 3.2.2, so we need to continue to discuss which 1D model is a good model for the TMM structure. As discussed above, all the structures were simulated based upon a single plane wave which propagates in the longitudinal direction. However, when the TMM structure is used in a power divider, such as the simulations in Figure 3.9

and Figure 3.11, it involves four plane waves: one travels left, one travels right, one travels up and the other travels down. Therefore, we simulate a 17 by 17 TMM structure with four plane waves as shown in Figure 3.32, where the arrows show the directions of the plane waves. That is, a plane wave incidents on each boundary of the TMM structure. L and R denote the left-handed and right-handed unit cell, respectively. For comparison, we also simulate the two different 1D models with two plane waves excited at both ends, as shown in Figure 3.33 and Figure 3.34, respectively. We use the realisation models of Figure 3.3 in simulations. For clarity, Figure 3.32, Figure 3.33 and Figure 3.34 do not explicitly show the details of the left-handed unit cells. It is understood that the left-handed unit cells of Figure 3.32 and Figure 3.33 use the topology in Figure 3.3 (a) whilst the 1D left-handed unit cells of

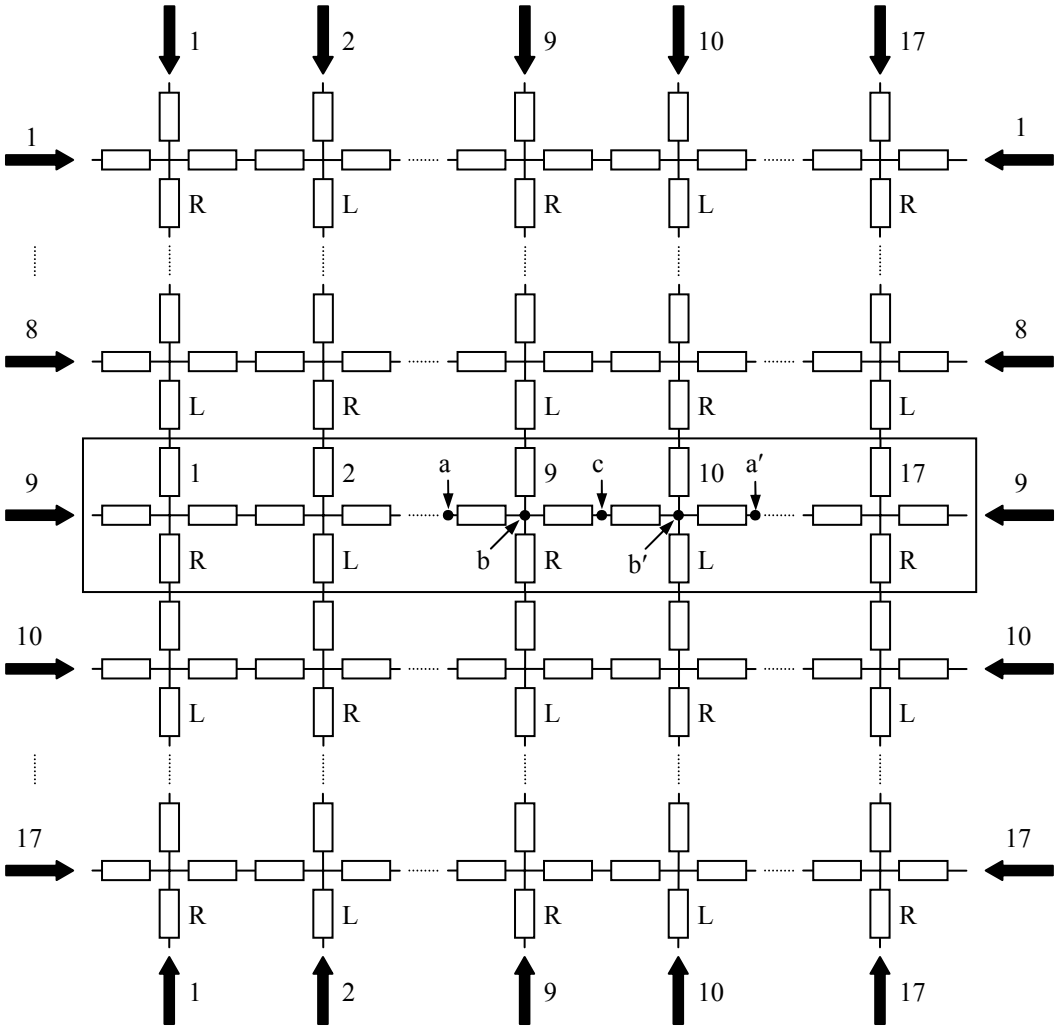


Fig. 3.32. The 17 by 17 TMM structure with four plane waves, where the arrows show the directions of the plane waves.

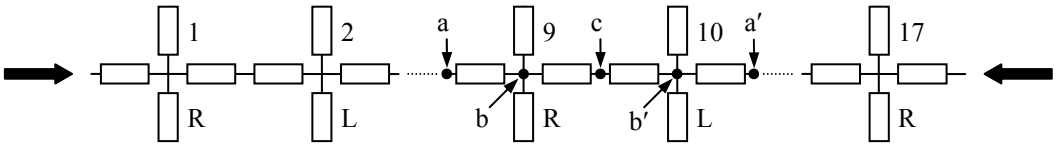


Fig. 3.33. The 1D model with opened transverse stubs excited by two plane waves at both ends, where the arrows show the directions of the plane waves.

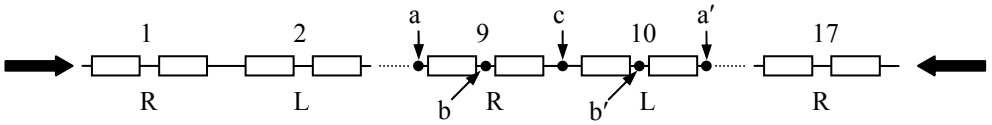


Fig. 3.34. The 1D model without the transverse stubs excited by two plane waves at both ends, where the arrows show the directions of the plane waves.

Figure 3.34 use the topology in Figure 3.4 (a).

Figure 3.35, Figure 3.36 and Figure 3.37 show the currents in the right-handed (No.9) and left-handed (No.10) unit cells of the TMM structure shown in Figure 3.32 and the two different 1D models shown in Figure 3.33 and Figure 3.34, respectively. All the currents at 1 GHz are summarised in Table 3.9. It is apparent that, at least at 1 GHz, the currents of the both unit cells in the 1D model shown in Figure 3.34 are much closer to those in the TMM structure, compared to the 1D model shown in Figure 3.33. Figure 3.38, Figure 3.39 and Figure 3.40 show the three nodes (a, b and c) voltages of the central right-handed unit cell (No.9) and the three nodes (c, b′ and a′) voltages of the left-handed unit cell (No.10) in the TMM structure of Figure 3.32 and the two different 1D models of Figure 3.33 and Figure 3.34, respectively. The

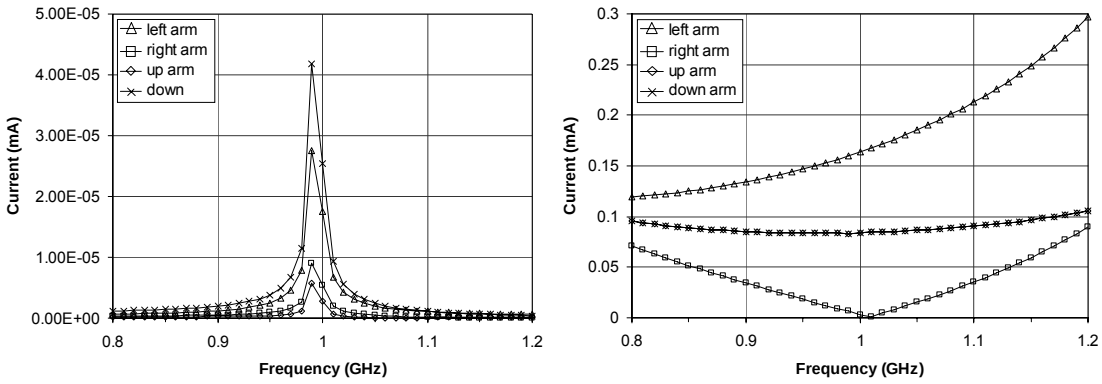


(a) (b)

Fig. 3.35. Simulated currents in the TMM structure of Fig. 3.32: (a) right-handed cell (No.9), and (b) left-handed cell (No.10).

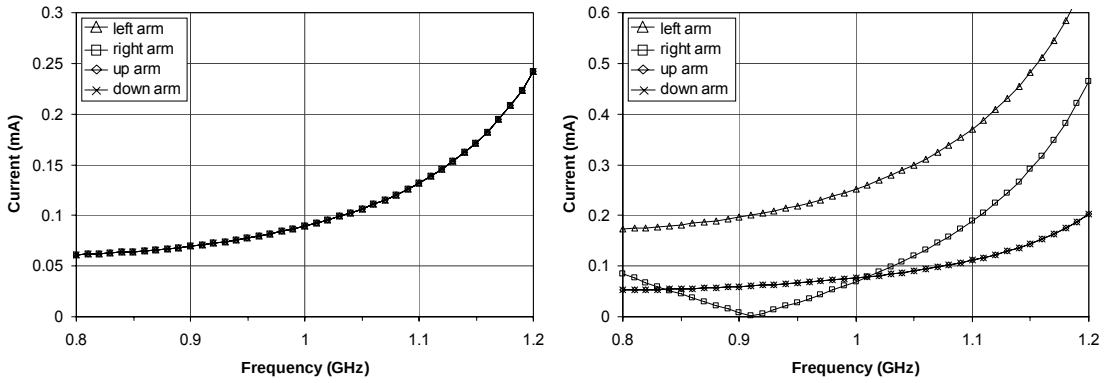


(a) (b)

Fig. 3.36. Simulated currents in the 1D model of Fig. 3.33: (a) right-handed cell (No.9), and (b) left-handed cell (No.10).

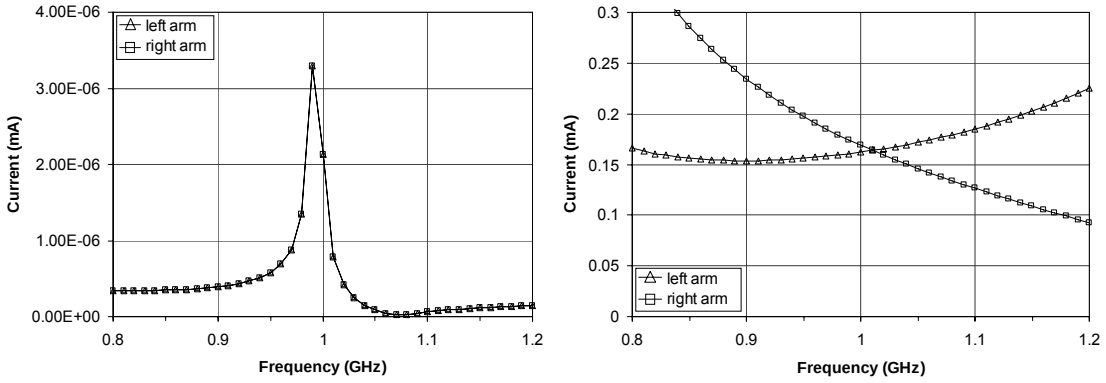


(a) (b)

Fig. 3.37. Simulated currents in the 1D model of Fig. 3.34: (a) right-handed cell (No.9), and (b) left-handed cell (No.10).

| | Currents (mA) | | | | | | | |
|---|---|---|---|---|---|---|---|---|
| | Right-handed unit cell (No.9) | | | | Left-handed unit cell (No.10) | | | |
| | left | right | up | down | left | right | up | down |
| TMM of Fig. 3.32 | 1.7e-5 | 5.3e-6 | 2.8e-6 | 2.5e-5 | 0.16 | 0.003 | 0.084 | 0.084 |
| 1D model of Fig. 3.33 | 0.09 | 0.09 | 0.09 | 0.09 | 0.25 | 0.069 | 0.076 | 0.076 |
| 1D model of Fig. 3.34 | 2.1e-6 | 2.1e-6 | / | / | 0.16 | 0.17 | / | / |

Table 3.9. The currents of three different structures at 1 GHz.

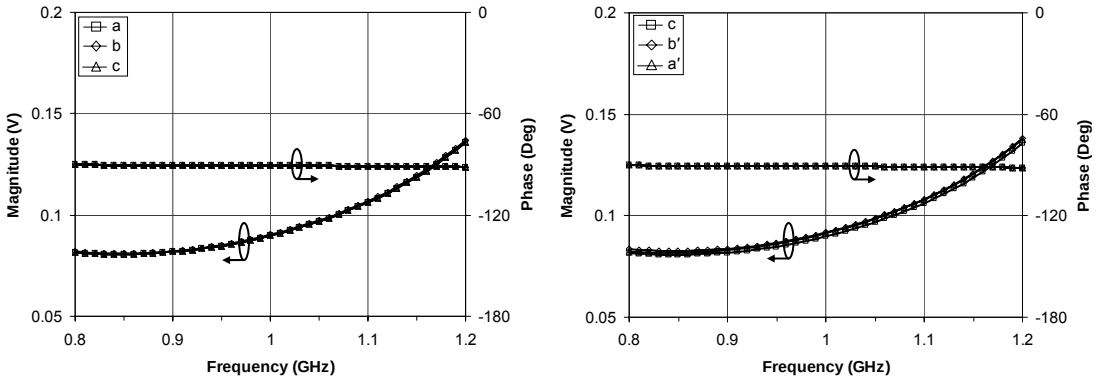


(a) (b)

Fig. 3.38. Simulated voltages in the TMM structure of Fig. 3.32: (a) right-handed cell (No.9) at three nodes (a, b, c), and (b) left-handed cell (No.10) at three nodes (c, b′, a′).

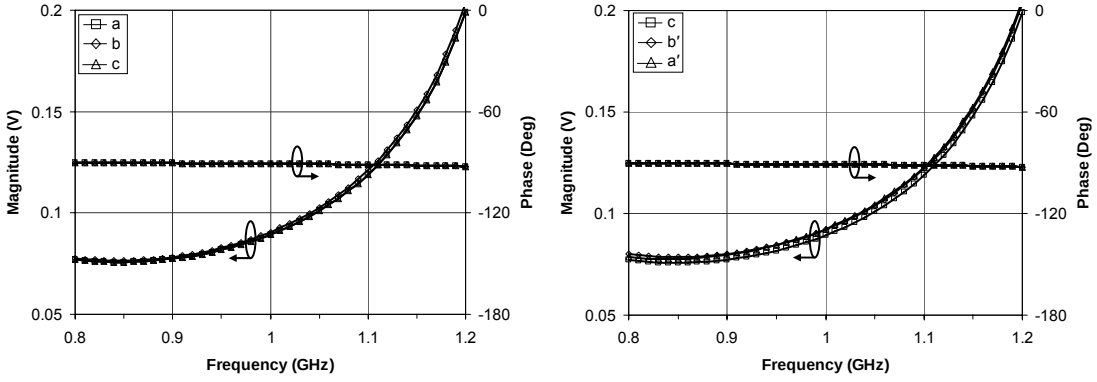


(a) (b)

Fig. 3.39. Simulated voltages in the 1D model of Fig. 3.33: (a) right-handed cell (No.9) at three nodes (a, b, c), and (b) left-handed cell (No.10) at three nodes (c, b′, a′).

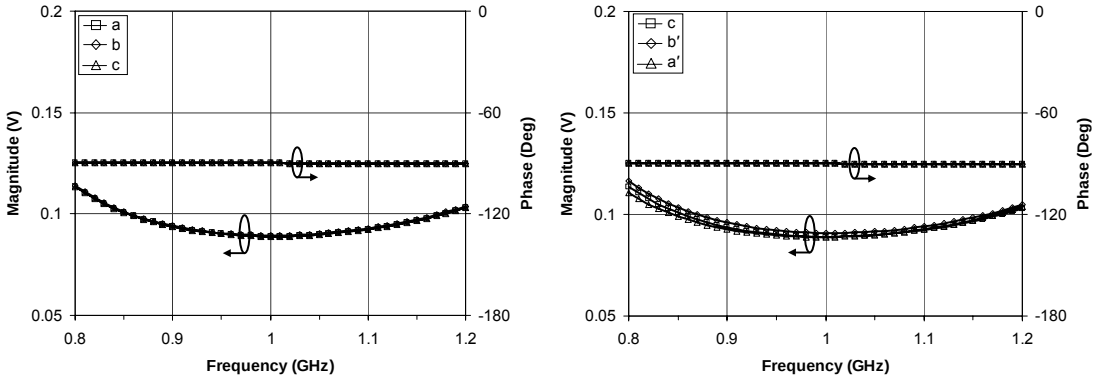


(a) (b)

Fig. 3.40. Simulated voltages in the 1D model of Fig. 3.34: (a) right-handed cell (No.9) at three nodes (a, b, c), and (b) left-handed cell (No.10) at three nodes (c, b′, a′).

| | Voltages | | | | | |
|---|---|---|---|---|---|---|
| | a | | b | | c | |
| | Magnitude | Phase | Magnitude | Phase | Magnitude | Phase |
| TMM of Fig. 3.32 | 0.09 V | -90.48° | 0.09 V | -90.48° | 0.09 V | -90.48° |
| 1D model of Fig. 3.33 | 0.089 V | -90.89° | 0.091 V | -90.89° | 0.089 V | -90.89° |
| 1D model of Fig. 3.34 | 0.089 V | -89.98° | 0.089 V | -89.98° | 0.089 V | -89.98° |

Table 3.10. The voltages in the central right-handed cells (No.9) of three different structures at 1 GHz.

| | Voltages | | | | | |
|---|---|---|---|---|---|---|
| | c | | b′ | | a′ | |
| | Magnitude | Phase | Magnitude | Phase | Magnitude | Phase |
| TMM of Fig. 3.32 | 0.09 V | -90.48° | 0.092 V | -90.48° | 0.091 V | -90.48° |
| 1D model of Fig. 3.33 | 0.089 V | -90.89° | 0.092 V | -90.89° | 0.092 V | -90.89° |
| 1D model of Fig. 3.34 | 0.089 V | -89.98° | 0.091 V | -89.98° | 0.089 V | -89.98° |

Table 3.11. The voltages in the left-handed cells (No.10) of three different structures at 1 GHz.

voltages of the both unit cells at 1 GHz are summarised in Table 3.10 and Table 3.11. We can also see that, at least at 1 GHz, the voltages of the both unit cells in the 1D model shown in Figure 3.34 are consistent with those in the TMM structure.

In conclusion, according to the simulation results of the 17 by 17 and 5 by 5 TMM structures shown in Figure 3.9 and Figure 3.11 and the simulations with four plane waves discussed in this section, at least at the design frequency of 1 GHz, the 1D line model without the transverse arms provides a good equivalent model for the 2D left-

handed and right-handed unit cells of the TMM structure which is non-homogeneous, where the left-handed unit cells are connected only to the right-handed unit cells and vice versa. Therefore, to design the 2D left-handed and right-handed unit cells, we can design their equivalent 1D unit cells firstly, and then use these results in the 2D unit cells.

## 3.3 DESIGN OVERVIEW

The 5 by 5 TMM structure exhibits a 20-way equal power division but with the coupling phases alternated between two values which differ by $2\varphi$ at the centre frequency. In order to obtain the equal phases at peripheral ports, extra compensating right-handed transmission lines with two different electrical lengths can be connected to the output ports of the TMM structure as depicted in Figure 3.41. These two different length transmission lines are denoted as TL1 and TL2, respectively, and their characteristic impedances must be equal to the Bloch impedance of left-handed and right-handed unit cells. Since the difference of coupling phases is $2\varphi$ at the output ports of the TMM structure, the insertion phase should be $-\theta+\varphi$ in TL1 and $-\theta-\varphi$ in TL2 at the centre frequency, where $\theta$ is a positive constant, so that the divider coupling phases are equal at the output ports of the 20-way power divider at the centre frequency.

To design this 20-way power divider, some main conditions need to be satisfied as follow:

1. The insertion phases in the left-handed and right-handed unit cells are equal but with opposite sign;
2. Each unit cell has the same Bloch impedance and is matched to each other;
3. The physical sizes of the left-handed and right-handed unit cells are the same and each unit cell is square shaped.

Before left-handed and right-handed unit cells are built, their 1D version unit cells are designed firstly to achieve the above conditions. Therefore, the 2D unit cells can be designed directly from their 1D version unit cells. Finally, because the transmission line TL2 is longer than TL1, it must be meandered to ensure that the output ports are located on a straight line; thus the 20-way power divider is square-shaped.

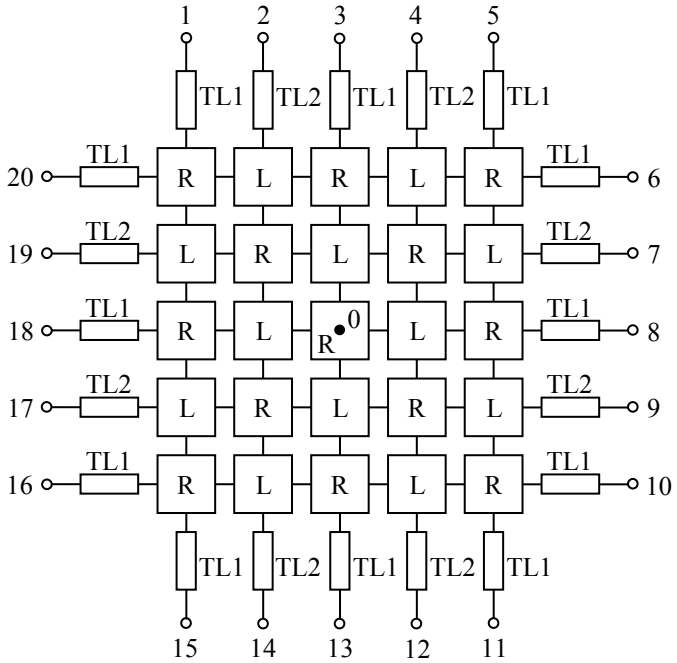


Fig. 3.41. Square shaped 20-way power divider based on a TMM structure.

# Chapter 4

# DESIGN AND TEST OF 1D TEST UNIT CELLS

In this chapter, we present the details about the 1D left-handed and right-handed unit cells. In section 4.1, we give the design processes of the 1D left-handed and right-handed unit cells, and then the simulation results are shown in section 4.2. Finally, we fabricate these unit cells and give the measurement results in section 4.3.

## 4.1 DESIGN 1D UNIT CELLS

To validate design methods and fabrication techniques, the 1D version left-handed and right-handed unit cells are built before the 2D unit cells are designed. In this section, we analyse the 1D left-handed unit cell firstly, and then present the design processes of the 1D left-handed and right-handed unit cells.

### 4.1.1 ANALYSIS OF THE IDEAL *L*-*C* NETWORK

Before analysing the 1D left-handed unit cell, we analyse an ideal *L*-*C* network in a high-pass topology structure. It can help us to choose the values of the inductor and capacitors in the 1D left-handed unit cell. This network is depicted in Figure 4.1.

Its ABCD matrix is expressed as

$$\begin{pmatrix} A & B \\ C & D \end{pmatrix} = \begin{pmatrix} 1 & \dfrac{1}{j2\omega C_0} \\ 0 & 1 \end{pmatrix} \cdot \begin{pmatrix} 1 & 0 \\ \dfrac{1}{j\omega L_0} & 1 \end{pmatrix} \cdot \begin{pmatrix} 1 & \dfrac{1}{j2\omega C_0} \\ 0 & 1 \end{pmatrix}, \tag{4.1}$$

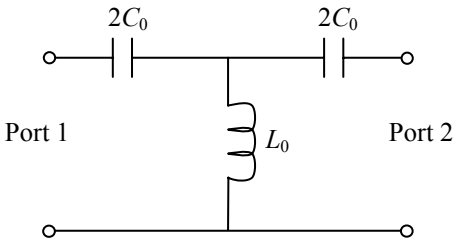


Fig. 4.1. An ideal *L*-*C* network in a high-pass topology structure.

and the ABCD parameters are derived as

$$A = 1 - \frac{1}{2\omega^2 L_0 C_0} \tag{4.2a}$$

$$B = \frac{1}{j\omega C_0}\left(1 - \frac{1}{4\omega^2 L_0 C_0}\right) \tag{4.2b}$$

$$C = \frac{1}{j\omega L_0} \tag{4.2c}$$

$$D = 1 - \frac{1}{2\omega^2 L_0 C_0} = A\,. \tag{4.2d}$$

Then the Bloch impedance of the network is given by [28]:

$$Z_B = \sqrt{\frac{B}{C}} = \sqrt{\frac{L_0}{C_0}}\sqrt{1 - \frac{1}{4\omega_0^2 L_0 C_0}}\,, \tag{4.3}$$

where $\omega_0 = 2\pi f_0$ and $f_0$ is the design frequency. Its S-parameters, $S_{11}$ and $S_{21}$, are calculated using equations [28]:

$$\begin{aligned} S_{11} &= \frac{A + B/Z_0 - CZ_0 - D}{A + B/Z_0 + CZ_0 + D} \\ &= \frac{\dfrac{1}{j\omega}\left[\dfrac{1}{C_0 Z_0}\left(1 - \dfrac{1}{4\omega^2 L_0 C_0}\right) - \dfrac{Z_0}{L_0}\right]}{2 - \dfrac{1}{\omega^2 L_0 C_0} + \dfrac{1}{j\omega}\left[\dfrac{1}{C_0 Z_0}\left(1 - \dfrac{1}{4\omega^2 L_0 C_0}\right) + \dfrac{Z_0}{L_0}\right]}, \end{aligned} \tag{4.4}$$

$$S_{21} = \frac{2}{A + B/Z_0 + CZ_0 + D} = \frac{2}{2 - \frac{1}{\omega^2 L_0 C_0} + \frac{1}{j\omega}\left[\frac{1}{C_0 Z_0}\left(1 - \frac{1}{4\omega^2 L_0 C_0}\right) + \frac{Z_0}{L_0}\right]}, \tag{4.5}$$

where $Z_0$ is the port reference impedance. To ensure that $S_{11}$ is equal to zero at the design frequency, we have

$$Z_B = Z_0, \tag{4.6}$$

and then $S_{21}$ at the design frequency can be reduced to

$$S_{21} = \frac{2\omega_0^2 L_0 C_0}{(2\omega_0^2 L_0 C_0 - 1) - j\sqrt{4\omega_0^2 L_0 C_0 - 1}}, \tag{4.7}$$

and the phase angle of $S_{21}$ at the design frequency is

$$\angle S_{21} = \arctan \frac{\sqrt{4\omega_0^2 L_0 C_0 - 1}}{2\omega_0^2 L_0 C_0 - 1}. \tag{4.8}$$

In general, the phase angle is very small ($\phi_{21} \ll 1$), thus $\tan\phi_{21} \approx \phi_{21}$ and $\omega^2 L_0 C_0 \gg 1$, and (4.8) can be written approximately as

$$\angle S_{21} \approx \frac{1}{\omega_0 \sqrt{L_0 C_0}}. \tag{4.9}$$

In this thesis, the design frequency is 1 GHz, and we use (4.3) and (4.8) to plot the graphs of the Bloch impedance and the phase angle of $S_{21}$ versus $L_0$ and $2C_0$, at 1 GHz, where the range of $L_0$ is 0 to 80 nH and the range of $2C_0$ is 0 to 10 pF. These graphs are shown in Figure 4.2 and Figure 4.3.

Also, we have several choices of values of $L_0$ and $2C_0$ to design the 1D left-handed unit cell, where $L_0$ is from the values of 12 nH, 22 nH and 43 nH, and $2C_0$ is from 1 pF, 2 pF, 4.7 pF and 10 pF. Then the Bloch impedance and the phase angle of $S_{21}$ from these twelve combinations at 1 GHz are calculated using (4.3) and (4.8), and plotted in Figure 4.2 and Figure 4.3, and summarised in Table 4.1 and Table 4.2.

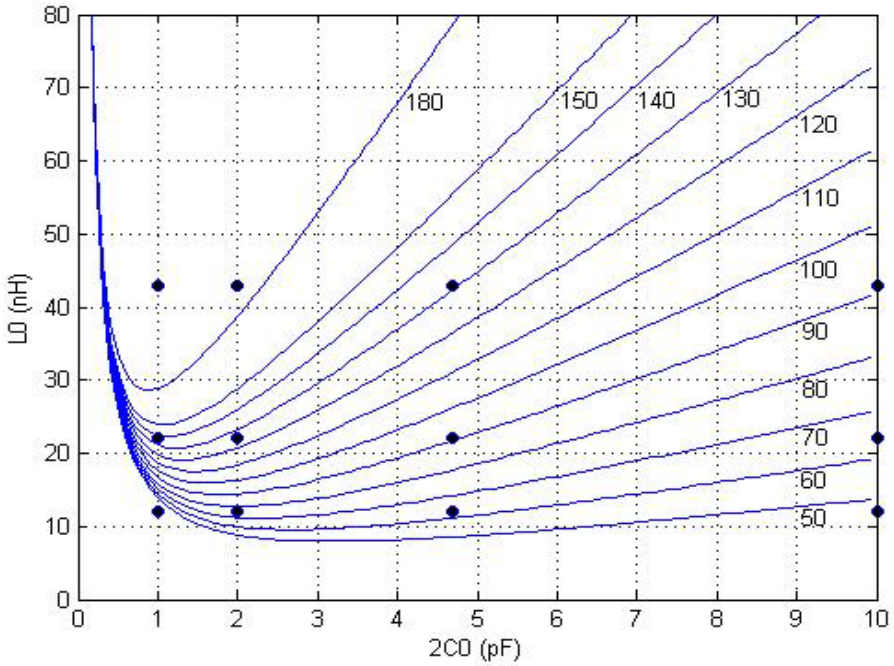


Fig. 4.2. The graph of the Bloch impedance versus $L_0$ and $2C_0$ at 1 GHz.

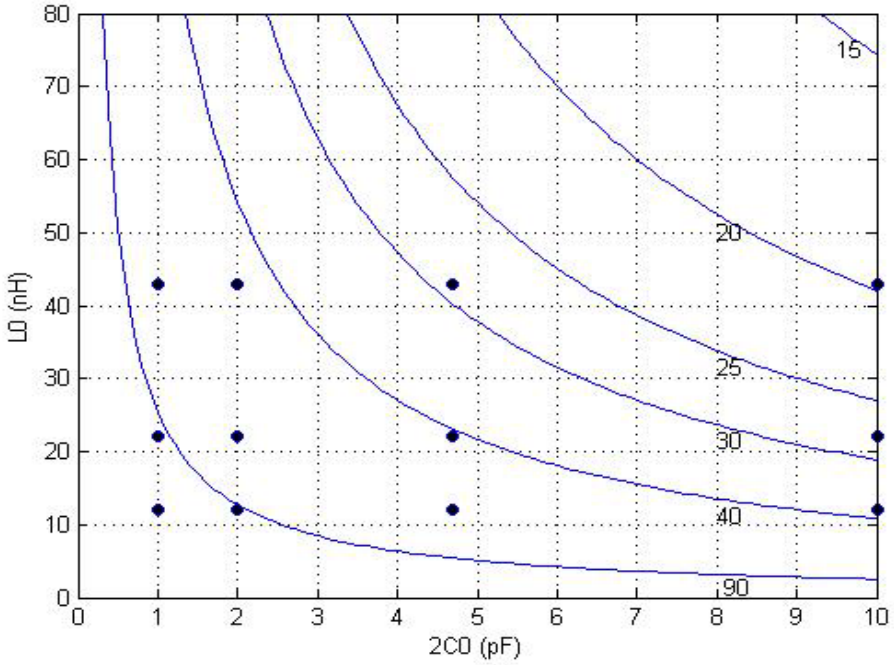


Fig. 4.3. The graph of the phase angle of $S_{21}$ versus $L_0$ and $2C_0$ at 1 GHz.

| $Z_0$ (Ω) | | $2C_0$ (pF) | | | |
|---|---|---|---|---|---|
| | | 1 | 2 | 4.7 | 10 |
| $L_0$ (nH) | 12 | / | 75.28 | 62.93 | 46.33 |
| | 22 | 136.64 | 125.17 | 90.64 | 64.39 |
| | 43 | 246.31 | 191.49 | 130.96 | 91.36 |

Table 4.1. The Bloch impedance from the twelve combinations at 1 GHz.

| $\Phi_{21}$ (deg) | | $2C_0$ (pF) | | | |
|---|---|---|---|---|---|
| | | 1 | 2 | 4.7 | 10 |
| $L_0$ (nH) | 12 | / | 93.18 | 56.57 | 37.92 |
| | 22 | 98.71 | 64.89 | 40.97 | 27.77 |
| | 43 | 65.74 | 45.13 | 28.99 | 19.76 |

Table 4.2. The phase angle of $S_{21}$ from the twelve combinations at 1 GHz.

### 4.1.2 ANALYSIS OF THE PRACTICAL 1D LEFT-HANDED UNIT CELL

We now analyse the 1D left-handed unit cell as shown in Figure 4.4. $Z_{01}$ and $\phi_1$ are characteristic impedance and phase shift of host transmission line, respectively. It is observed that the difference between the left-handed unit cells shown in Figure 4.4 and Figure 3.4 is that the capacitors and transmission lines are exchanged their places. This change ensures that the left-handed unit cell can be fabricated in microstrip line, and it causes an insignificant effect provided the length of transmission line is much smaller than one wavelength.

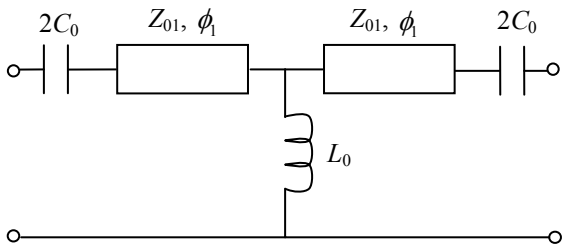


Fig. 4.4. The 1D left-handed unit cell.

The ABCD matrix of this network is derived as

$$\begin{pmatrix} A & B \\ C & D \end{pmatrix} = \begin{pmatrix} 1 & \dfrac{1}{j2\omega C_0} \\ 0 & 1 \end{pmatrix} \cdot \begin{pmatrix} \cos\phi_1 & jZ_{01}\sin\phi_1 \\ j\dfrac{\sin\phi_1}{Z_{01}} & \cos\phi_1 \end{pmatrix} \cdot \begin{pmatrix} 1 & 0 \\ \dfrac{1}{j\omega L_0} & 1 \end{pmatrix} \cdot \begin{pmatrix} \cos\phi_1 & jZ_{01}\sin\phi_1 \\ j\dfrac{\sin\phi_1}{Z_{01}} & \cos\phi_1 \end{pmatrix} \cdot \begin{pmatrix} 1 & \dfrac{1}{j2\omega C_0} \\ 0 & 1 \end{pmatrix}, \tag{4.10}$$

and the ABCD parameters are

$$A = \left(1 - \frac{1}{2\omega^2 L_0 C_0}\right)\cos^2\phi_1 + \left(\frac{1}{\omega C_0 Z_{01}} + \frac{Z_{01}}{\omega L_0}\right)\sin\phi_1\cos\phi_1 - \sin^2\phi_1 \tag{4.11a}$$

$$B = \frac{1}{j\omega C_0}\left(1 - \frac{1}{4\omega^2 L_0 C_0}\right)\cos^2\phi_1 + j2Z_{01}\left(1 - \frac{1}{2\omega^2 L_0 C_0} - \frac{1}{4\omega^2 C_0{}^2 Z_{01}^2}\right)\sin\phi_1\cos\phi_1 + j\left(\frac{Z_{01}^2}{\omega L_0} + \frac{1}{\omega C_0}\right)\sin^2\phi_1 \tag{4.11b}$$

$$C = \frac{j2\sin\phi_1\cos\phi_1}{Z_{01}} + \frac{\cos^2\phi_1}{j\omega L_0} \tag{4.11c}$$

$$D = \left(1 - \frac{1}{2\omega^2 L_0 C_0}\right)\cos^2\phi_1 + \left(\frac{1}{\omega C_0 Z_{01}} + \frac{Z_{01}}{\omega L_0}\right)\sin\phi_1\cos\phi_1 - \sin^2\phi_1 = A\,. \tag{4.11d}$$

The Bloch impedance of the network is calculated using (4.11b) and (4.11c)

$$Z_B = \sqrt{\frac{B}{C}}\,. \tag{4.12}$$

And S-parameters, $S_{11}$ and $S_{21}$, are obtained using equations [28]

$$S_{11} = \frac{A + B/Z_0 - CZ_0 - D}{A + B/Z_0 + CZ_0 + D} \tag{4.13}$$

$$S_{21} = \frac{2}{A + B/Z_0 + CZ_0 + D}, \tag{4.14}$$

where $Z_0$ is the port reference impedance. To ensure that $S_{11}$ is zero at the design frequency, we also obtain

$$Z_B = Z_0 . \tag{4.15}$$

Then the phase angle of $S_{21}$ is found from (4.14)

$$\angle S_{21} = \arctan \frac{\left[\frac{1}{\omega C_0 Z_0}\left(1-\frac{1}{4\omega^2 L_0 C_0}\right)+\frac{Z_0}{\omega L_0}\right]\cos^2\phi_1 - \frac{1}{Z_0}\left(\frac{Z_{01}^2}{\omega L_0}+\frac{1}{\omega C_0}\right)\sin^2\phi_1}{-\left[\frac{Z_{01}}{Z_0}\left(1-\frac{1}{2\omega^2 L_0 C_0}-\frac{1}{4\omega^2 C_0{}^2 Z_{01}^2}\right)+\frac{Z_0}{Z_{01}}\right]\sin 2\phi_1} \\ 2\left(1-\frac{1}{2\omega^2 L_0 C_0}\right)\cos^2\phi_1 + 2\left(\frac{1}{\omega C_0 Z_{01}}+\frac{Z_{01}}{\omega L_0}\right)\sin\phi_1\cos\phi_1 - 2\sin^2\phi_1 . \tag{4.16}$$

### 4.1.3 DESIGN PROCESSES OF THE 1D LEFT-HANDED AND RIGHT-HANDED UNIT CELLS

To fabricate the unit cells, microstrip line is used to realise the transmission lines in left-handed and right-handed unit cells, and the inductor and capacitors of the left-handed unit cell are surface mount components. The inductor is placed in a hole which is drilled through the substrate in the centre of microstrip line, and this method has been validated in [7]. Figure 4.5 and Figure 4.6 show the 1D left-handed and right-handed unit cells realised by microstrip line, respectively.

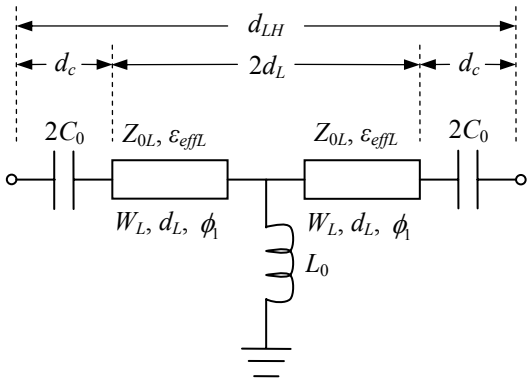


Fig. 4.5. Microstrip line 1D left-handed unit cell.

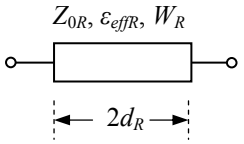


Fig. 4.6. Microstrip line 1D right-handed unit cell.

$Z_{0L}$ and $\varepsilon_{effL}$ denote the characteristic impedance and effective dielectric constant of microstrip line in the left-handed unit cell, and $W_L$, $d_L$ and $\phi_1$ denote its width, length and phase shift, respectively. Similarly, $Z_{0R}$, $\varepsilon_{effR}$, $W_R$ and $d_R$ denote those parameters of microstrip line in the right-handed unit cell. A gap with length $d_c$ is used to accommodate the capacitor, hence the size of the left-handed unit cell is

$$d_{LH} = 2\left(d_c + d_L\right), \tag{4.17}$$

and the length of microstrip line, $d_L$, is

$$d_L = \frac{d_{LH} - 2d_c}{2}. \tag{4.18}$$

To achieve the same size left-handed and right-handed cells:

$$2d_R = d_{LH} = 2\left(d_c + d_L\right). \tag{4.19}$$

In the left-handed unit cell, $Z_{0L}$ is calculated using (4.3)

$$Z_{0L} = \sqrt{\frac{L_0}{C_0}}\sqrt{1 - \frac{1}{4\omega_0^2 L_0 C_0}}, \tag{4.20}$$

where $\omega_0 = 2\pi f_0$ and $f_0$ is the design frequency. In general, the Bloch impedance of the left-handed unit cell is a function of $d_{LH}$, and the phase of $S_{21}$, $\angle S_{21L}$, is an nonlinear function of $d_{LH}$. However, if we use (4.20), we can see that the sensitivity between the Bloch impedance and $d_{LH}$ will be considerably reduced, and the phase of $S_{21}$, $\angle S_{21L}$, will be an approximate linear function of $d_{LH}$.

Then $W_L$ and $\varepsilon_{effL}$ can be obtained using microstrip line design equations [28]. Therefore, the phase shift $\phi_1$ is [28]

$$\phi_1 = \sqrt{\varepsilon_{effL}} k_0 d_L = \frac{2\pi f_0}{c} \sqrt{\varepsilon_{effL}} d_L = \frac{2\pi f_0}{c} \sqrt{\varepsilon_{effL}} \left( \frac{d_{LH} - 2d_c}{2} \right). \tag{4.21}$$

We can find the Bloch impedance of the left-handed unit cell using (4.10) and (4.12), $S_{11}$ using (4.13) and $S_{21}$ using (4.14). If (4.15) is satisfied, $S_{11}$ becomes zero at the design frequency. Thus, to ensure that the left-handed and right-handed unit cells are matched to each other, we get

$$Z_{0R} = Z_0 = Z_B \,. \tag{4.22}$$

Using (4.16), the phase of $S_{21}$, $\angle S_{21L}$, can be calculated as a function of $d_{LH}$.

In the right-handed unit cell, $Z_{0R}$ is obtained from (4.22), and $W_R$ and $\varepsilon_{effR}$ are obtained using microstrip line design equations [28]. Hence, the insertion phase of microstrip line can be expressed [28]

$$\angle S_{21R} = -\sqrt{\varepsilon_{effR}} k_0 2d_R = -\frac{2\pi f_0}{c} \sqrt{\varepsilon_{effR}} 2d_R = -\frac{2\pi f_0}{c} \sqrt{\varepsilon_{effR}} d_{LH} \,, \tag{4.23}$$

and it is also a function of $d_{LH}$.

Since $\angle S_{21L}$ and $\angle S_{21R}$ are all functions of $d_{LH}$, we use Matlab to plot the curves of $\angle S_{21L}$ and $-\angle S_{21R}$ versus $d_{LH}$ using (4.16) and (4.23). The intersection point gives a value of $d_{LH}$ which ensures that the insertion phases of the left-handed and right-handed unit cells are equal but with opposite sign. Finally, $d_L$ and $d_R$ are calculated using (4.18) and (4.19), respectively.

In the design the 1D left-handed and right-handed unit cells, we choose a Taconic TLY-5 substrate [29] with dielectric constant $\varepsilon_r$ = 2.2 and dielectric height $H$ = 1.575 mm (62 mils). $L_0$ and $2C_0$ are chosen 43 nH and 10 pF, respectively, from the twelve combinations, because they ensure that the left-handed and right-handed unit cells are small and can be fabricated. $d_c$ is chosen 1 mm to accommodate the capacitor. The unit cells are designed to operate at 1 GHz. Using the design process discussed in above, $\angle S_{21L}$ and $-\angle S_{21R}$ versus $d_{LH}$ using (4.16) and (4.23) are plotted as shown in Figure 4.7.

The intersection point gives that $d_{LH}$ = 7.128 mm, and $\angle S_{21L} = -\angle S_{21R} = 11.42^\circ$.

Hence, $d_L$ = 2.564 mm and $2d_R$ = 7.128 mm. Moreover, other parameters are calculated as: $Z_{0L}$ = 91.36 Ω, $Z_{0R} = Z_B$ = 93.52 Ω, $W_L$ = 1.699 mm and $W_R$ = 1.618 mm.

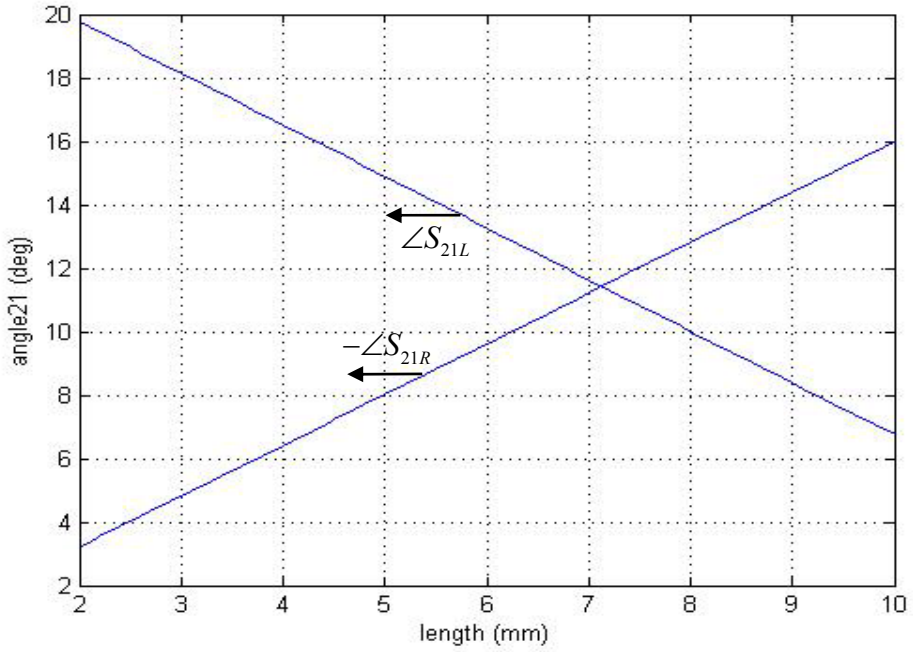


Fig. 4.7. Insertion phases of the left-handed and right-handed unit cells versus $d_{LH}$.

## 4.2 SIMULATION RESULTS

AWR Microwave Office is used to simulate the circuits of the left-handed and right-handed unit cells, shown in Figure 4.5 and Figure 4.6, with above calculated parameters, and doing a little tuning to optimise the simulation results, we obtain the final design parameters: $W_L$ = 1.668 mm, $W_R$ = 1.586 mm, $Z_{0L}$ = 91.3 Ω, $Z_{0R} = Z_B$ = 93.5 Ω, $d_L$ = 2.55 mm, and the size of the left-handed and right-handed unit cells is $d_{LH} = 2d_R$ = 7.1 mm.

Figure 4.8 and Figure 4.9 show the simulated $S_{11}$ magnitude and $S_{21}$ phase for the 1D left-handed and right-handed unit cells, respectively. The simulated $S_{21}$ magnitudes in both unit cells are almost 0 dB over the range from 0.6 GHz to 1.4 GHz, so they are not shown in the figures. The S-parameter port reference impedance for these two unit cells is 93.5 Ω. The simulation results show that the 1D left-handed and right-handed unit cells are matched to each other, and operate as expected at 1 GHz.

The insertion phases of the left-handed and right-handed unit cells at 1 GHz are 11.4° and -11.4°, respectively.

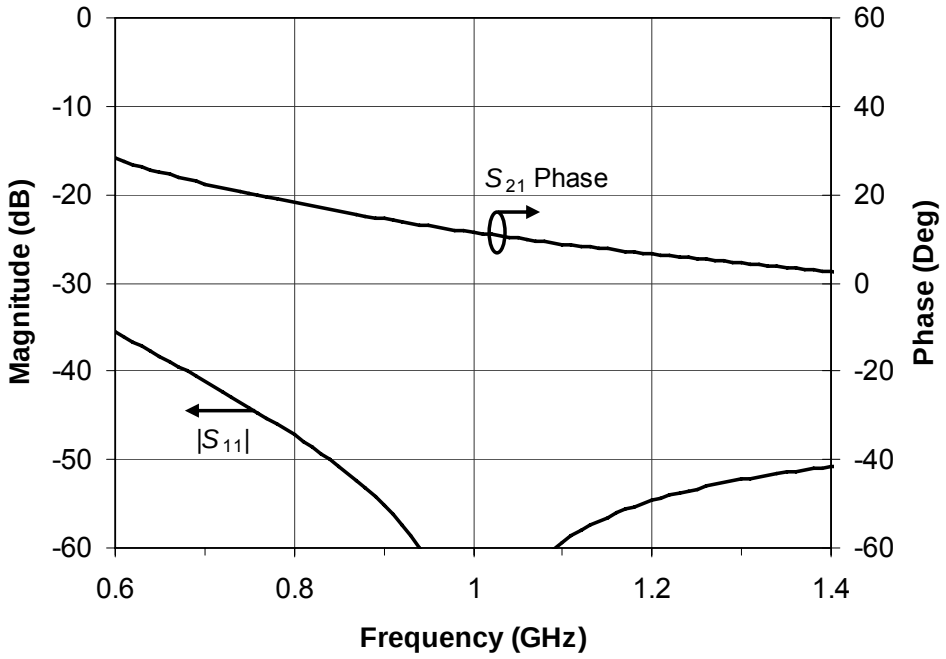


Fig. 4.8. Simulated responses of the 1D left-handed unit cell.

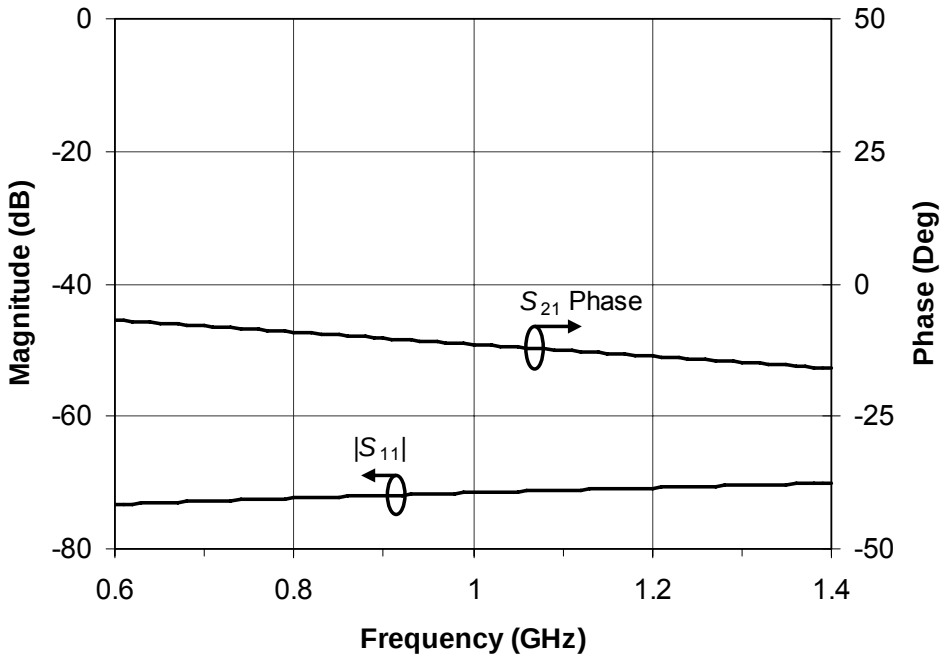


Fig. 4.9. Simulated responses of the 1D right-handed unit cell.

The above analysis has not considered the parasitic effects of lumped inductor and capacitor. In practice, the capacitor has a parasitic series inductance, and the inductor has a parasitic shunt capacitance. Therefore, the capacitor has a series resonant frequency, $F_{SR}$, and the inductor has a parallel resonant frequency, $F_{PR}$. The equivalent models of capacitor and inductor are shown in Figure 4.10 and Figure 4.11, respectively. And the equivalent 1D left-handed unit cell with parasitic effects of lumped components is shown in Figure 4.12.

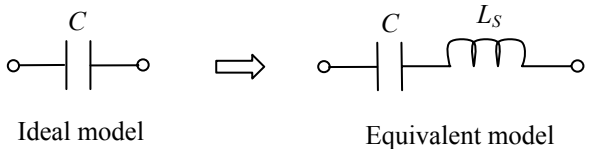


Fig. 4.10. The equivalent model of capacitor.

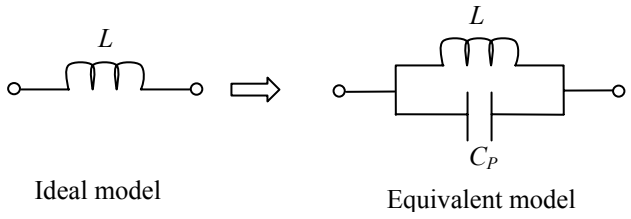


Fig. 4.11. The equivalent model of inductor.

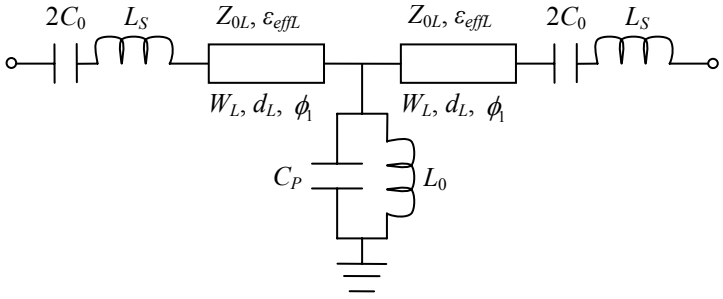


Fig. 4.12. The equivalent model for the 1D left-handed unit cell.

We choose the ATC 600S Series capacitors [30] and ATC 0603 Series inductors [31] in design and fabrication. For the 600S 10 pF capacitor, we find that its series resonant frequency $F_{SR}$ = 4.1147 GHz, from Tech-SELECT Component Selection program (version 3.3.1) [32] which is provided by American Technical Ceramics (ATC) company. Using the equation

$$2\pi F_{SR} = \frac{1}{\sqrt{L_S 2C_0}}, \tag{4.24}$$

we obtain $L_S$ = 0.15 nH. For the 0603 43 nH inductor, we obtain a parallel resonant frequency of $F_{PR}$ = 2 GHz, from Tech-SELECT Component Selection program (version 3.3.1) [32]. Using the equation

$$2\pi F_{PR} = \frac{1}{\sqrt{L_0 C_P}}, \tag{4.25}$$

we calculate $C_P$ = 0.15 pF.

Figure 4.13 shows the simulation results of the 1D left-handed unit cell with parasitic effects shown in Figure 4.12. The simulated $S_{21}$ magnitude is not shown due to its value is nearly 0 dB. The S-parameter port reference impedance is 93.5 Ω. The simulation results reveal that the insertion phase of the 1D left-handed unit cell becomes 8.3° at 1 GHz, and the insertion phases of the 1D left-handed and right-handed unit cells become equal but with opposite sign at 0.93 GHz. The 1D left-handed unit cell also operates at 1 GHz with a wide bandwidth, and is matched to the 1D right-handed unit cell. Therefore, the effect of parasitics is not significant at 1 GHz.

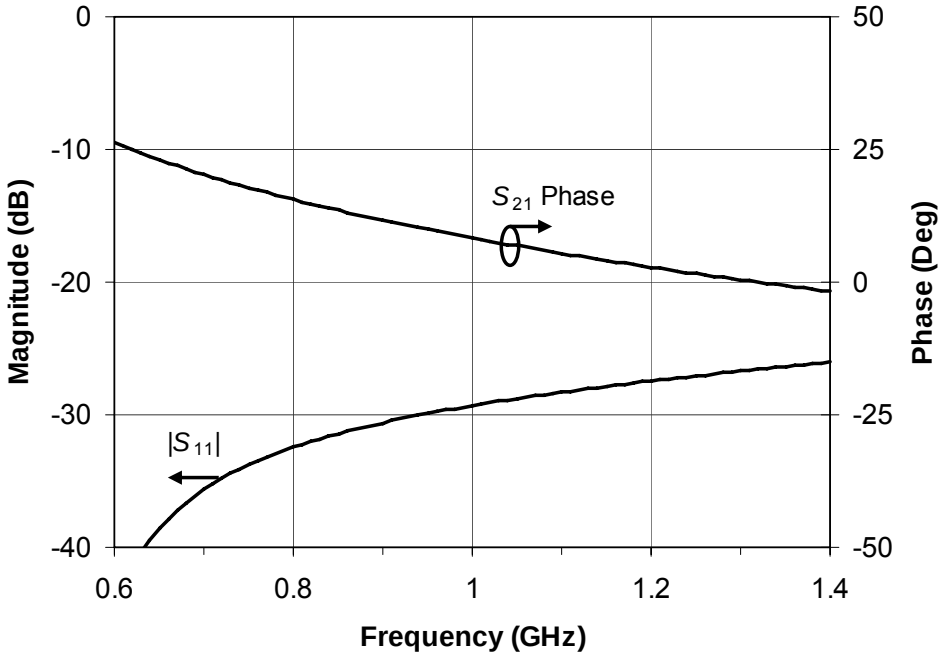


Fig. 4.13. Simulated responses of the equivalent 1D left-handed unit cell.

## 4.3 EXPERIMENTAL RESULTS

### 4.3.1 FABRICATION OF THE TEST CIRCUIT

To fabricate and test the 1D left-handed and right-handed unit cells, we choose the components discussed above and the SMA coaxial connectors [33].

Figure 4.14 and Figure 4.15 show the physical layout of the left-handed and right-handed unit cells with design parameters, respectively. A drill hole whose diameter is 1.5 mm is located in the centre of the microstrip line of the left-handed unit cell, and it is used to accommodate the inductor. The length of the left-handed unit cell is equal to the length of the right-handed unit cell, which are all 7.1 mm.

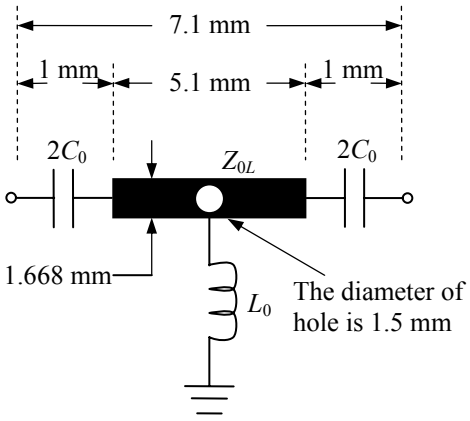


Fig. 4.14. The physical layout of the left-handed unit cell.

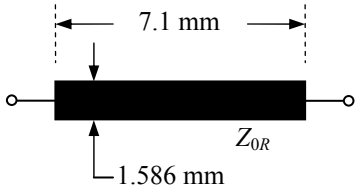


Fig. 4.15. The physical layout of the right-handed unit cell.

The left-handed and right-handed unit cell are measured in a 50 Ω microstrip line test fixture, so we build a 10 mm long microstrip interconnection line with 93.5 Ω (width is 1.586 mm) to match and connect to both sides of the left-handed and right-handed unit cells, and a 20 mm long 50 Ω microstrip feeding line (width is 4.8 mm) to connect to the SMA connector. Figure 4.16 shows the physical layout of this test

circuit. The total length of the test circuit is 67.1 mm. To determine the parasitic parameters of the SMA connector to microstrip line transitions, a 67.1 mm long 50 Ω microstrip test line (width is 4.8 mm) is fabricated in the same substrate with the test circuits of the left-handed and right-handed unit cells. Figure 4.17 displays the physical layout of the test circuit board, and Figure 4.18 shows a photograph of the fabricated test circuit board with SMA connectors.

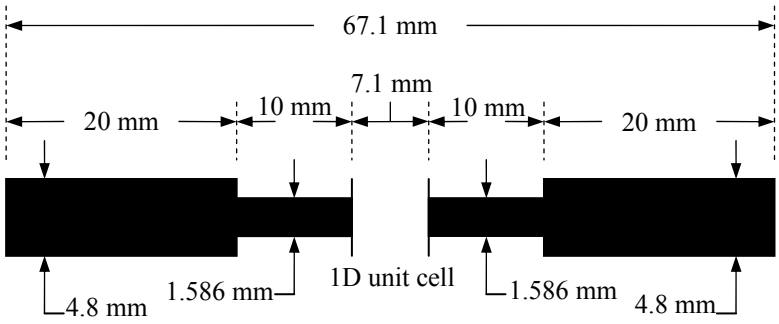


Fig. 4.16. The physical layout of the test circuit for left-/right-handed unit cell.

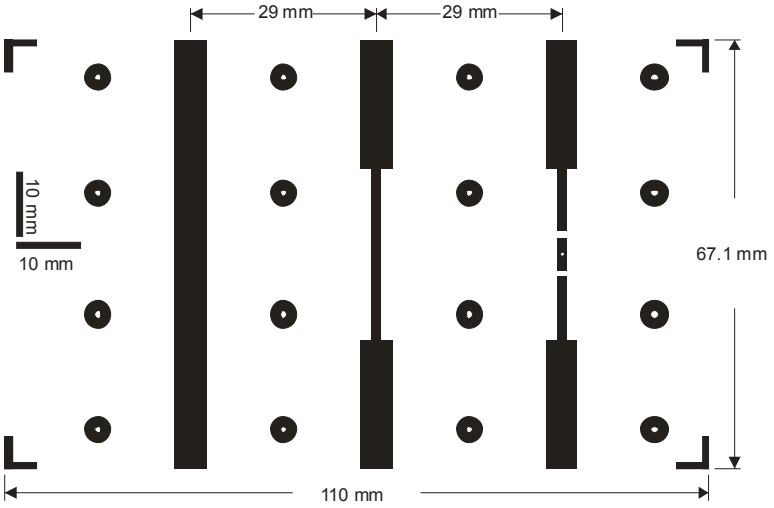


Fig. 4.17. The physical layout of the test circuit board.

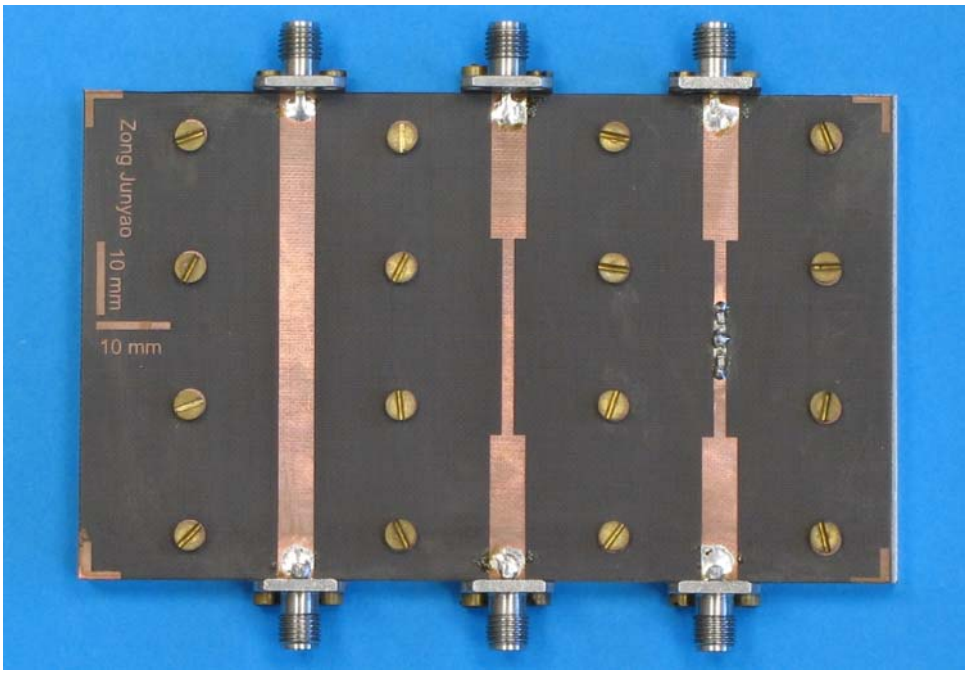


Fig. 4.18. The photo of the fabricated 1D test circuit board.

### 4.3.2 MEASUREMENT RESULTS

All measurements were carried out on a HP8753D network analyzer, and we obtained three groups of measurement results: 1D test circuit of the left-handed unit cell, 1D test circuit of the right-handed unit cell and a 67.1 mm long 50 Ω microstrip test line. We firstly describe the processes of obtaining the parasitic parameters of the SMA connector to microstrip line transitions, and then describe the de-embedded results.

Because the measurement results include the effects of discontinuities between the SMA connector and microstrip line, we need determine these parasitic parameters so that we can eliminate these effects from the measurement results and obtain the final test results. Figure 4.19 shows the cross section view of the SMA connector connected to microstrip line. Figure 4.20 shows the equivalent circuit model of the SMA connector with the parasitic parameters of discontinuity between the SMA connector and microstrip line. $L_1$, $C_1$ and $C_2$ are the parasitic inductance and capacitance of discontinuity, and $Z_0$ and $El$ are characteristic impedance and electrical length of the coaxial transmission line in the SMA connector, respectively, where $Z_0$ is 50 Ω. We simulate a circuit which comprises the 50 Ω microstrip test line and the

SMA connectors using the equivalent circuit model, as shown in Figure 4.21. Using simulated results of this circuit and test results of the 50 Ω microstrip test line, we ensure that simulated $|S_{11}|$ is equal to (measured $|S_{11}|$ +measured $|S_{22}|$)/2, and simulated $|S_{21}|$ is equal to measured $|S_{21}|$, and simulated $S_{21}$ phase is equal to measured $S_{21}$ phase; therefore we can obtain the optimisation results of $L_1$, $C_1$, $C_2$ and $EL$. Figure 4.22 shows the optimisation results, and the optimised model values are: $L_1$ = 0.46 nH, $C_1$ = 0.3 pF, $C_2$ = 0.03 pF, and $El$ = 11.39°. The simulated and measured $|S_{21}|$ are not shown in the figure because they are approximately equal to 0 dB.

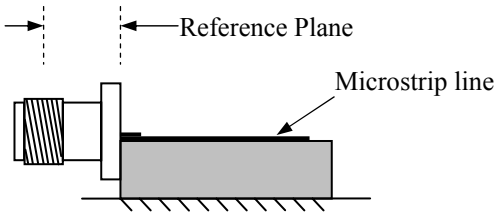


Fig. 4.19. The cross section view of the SMA connector connected to microstrip line.

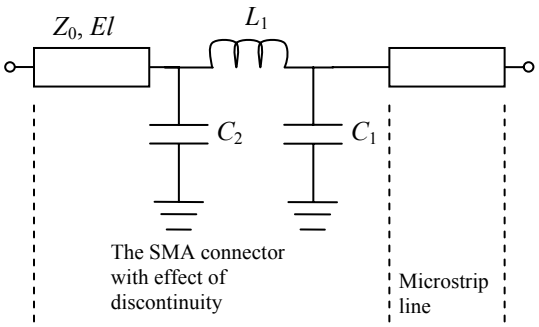


Fig. 4.20. The equivalent circuit model of the SMA connector with parasitic parameters of discontinuity.

The model for measurement results of the 1D left-handed and right-handed test circuits includes 1D left-handed and right-handed unit cells, 93.5 Ω microstrip interconnection lines, 50 Ω microstrip feeding lines, and the SMA connectors with effects of discontinuities, as shown in Figure 4.23. Figure 4.24 shows the de-embedding method to eliminate the effects of the SMA connectors, the discontinuities, the microstrip feeding and interconnection lines; thus, we obtain the de-embedded measurement results of the 1D left-handed and right-handed unit cells. In de-embedding, $-L_1$, $-C_1$, $-C_2$ and $-El$ are used in the SMA connector part to remove the effects of the SMA connector and discontinuity. A microstrip line with 50 Ω and -20

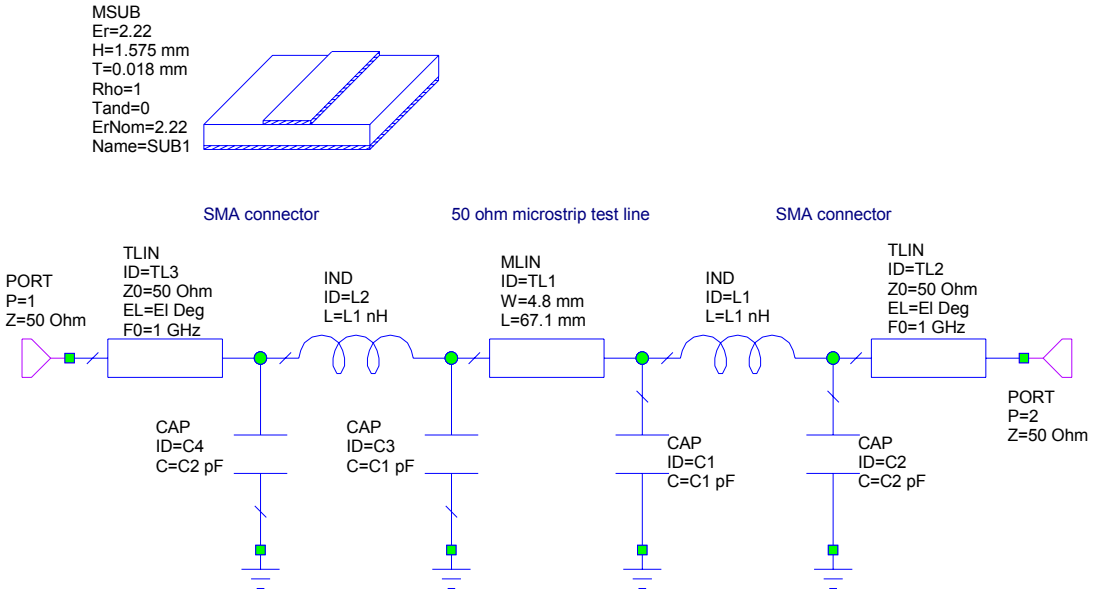


Fig. 4.21. The circuit model for the 50 Ω microstrip test line and the SMA connectors in Microwave Office.

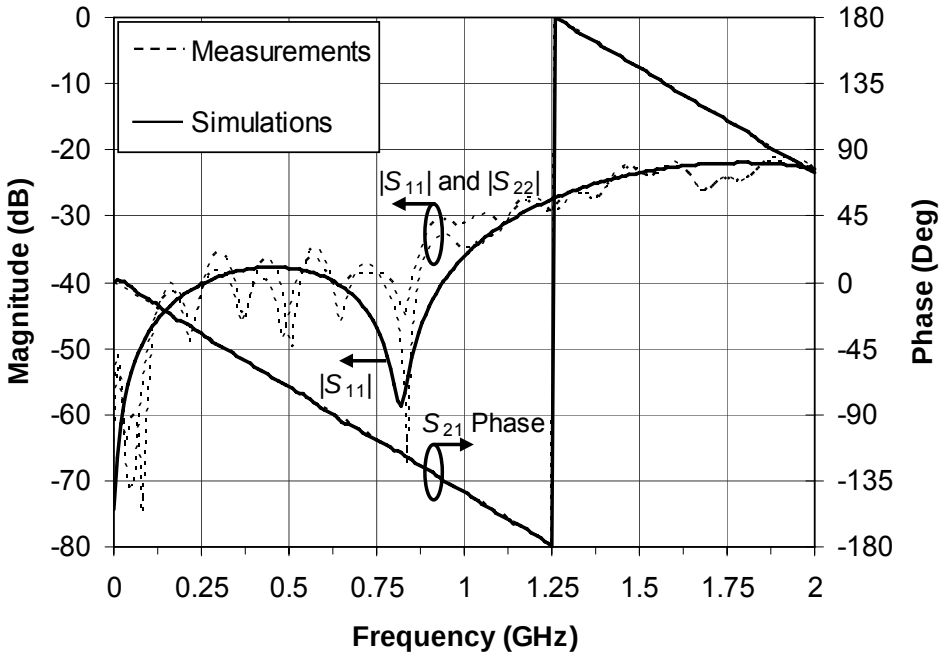


Fig. 4.22. Optimisation results of the 50 Ω test line.

mm length is used to eliminate the effect of the 50 Ω microstrip feeding line. The 93.5 Ω microstrip interconnection line is eliminated from the measurement results using a microstrip line with 93.5 Ω and -10 mm length.

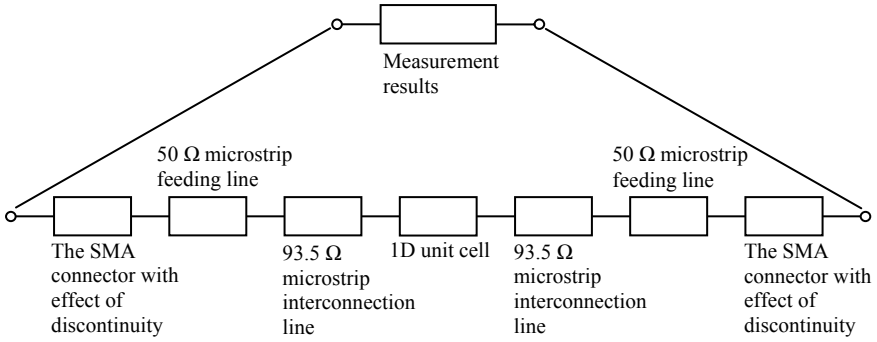


Fig. 4.23. Circuit model of measurement results.

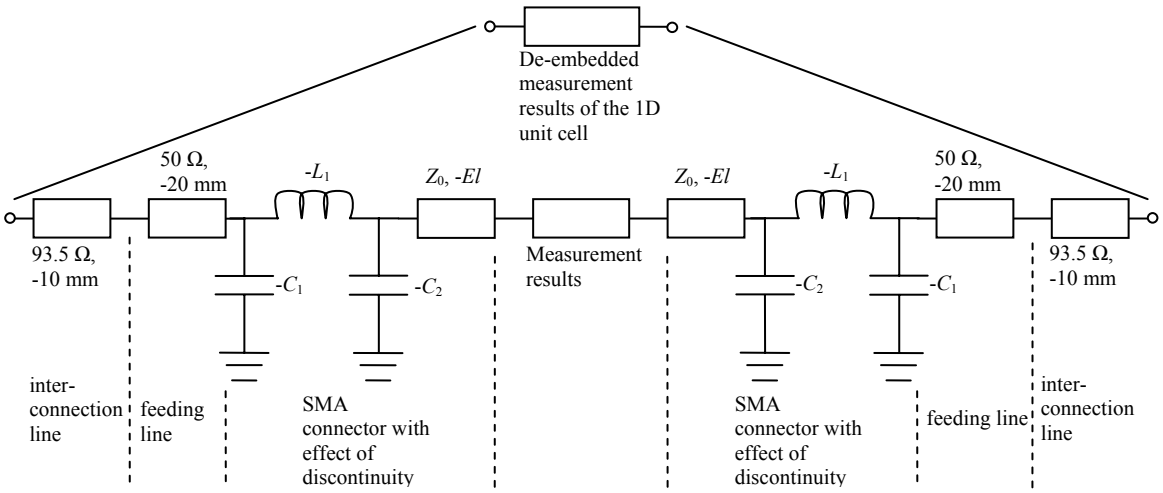


Fig. 4.24. De-embedding method.

Figure 4.25 and Figure 4.26 show the measured and simulated $S_{11}$ magnitudes and $S_{21}$ phases of the 1D left-handed and right-handed unit cells, respectively. The measured and simulated $S_{21}$ magnitudes are not displayed because they are approximately equal to 0 dB over this range, and the simulated $S_{11}$ magnitude for the right-handed unit cell is below -70 dB, so it is not shown in Figure 4.25. The S-parameter port reference impedance for these two unit cells is 93.5 Ω. The measurement results display that the 1D left-handed and right-handed unit cells are matched to each other over a wide bandwidth, and operate at 1 GHz. It is observed

that the measured $S_{21}$ phases of the 1D left-handed and right-handed unit cells correspond very closely to the simulated results. The measurements indicate that the insertion phases of the 1D left-handed and right-handed unit cells are 6.8° and -11.5°, respectively, at 1 GHz, and they are 8.3° and -11.4° in simulations. It is also clear that the measured insertion phases of the 1D left-handed and right-handed unit cells become equal but with opposite sign at 0.93 GHz, which is same as the result in simulations.

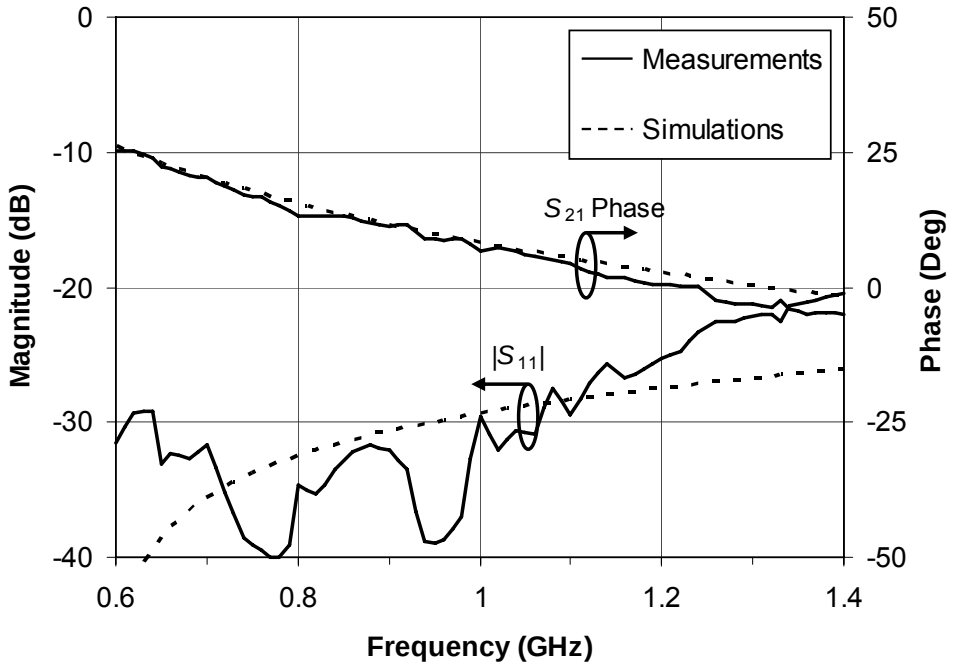


Fig. 4.25. Measured and simulated S-parameters of the 1D left-handed unit cell.

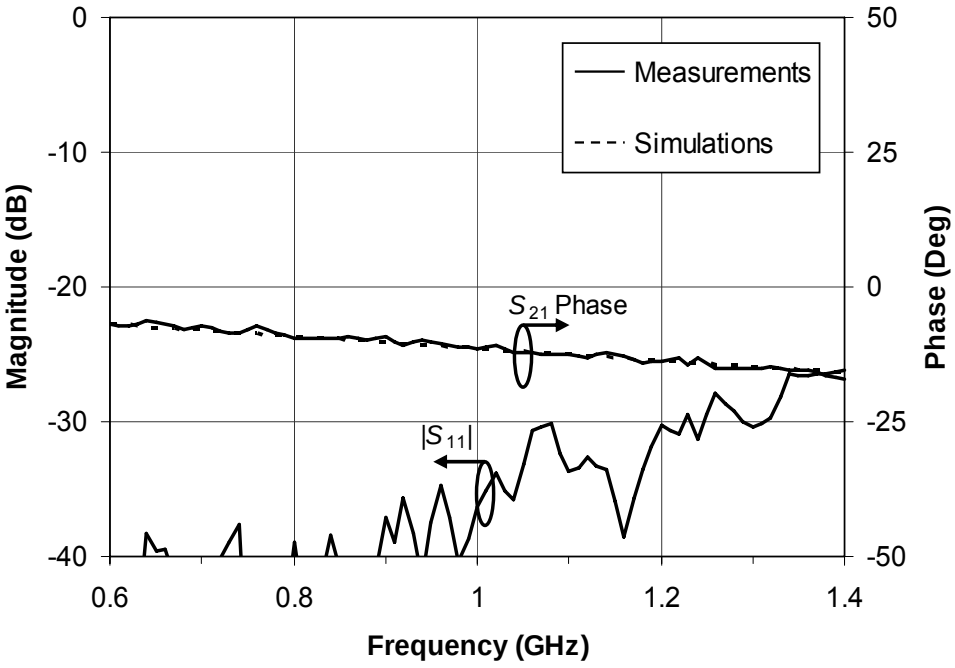


Fig. 4.26. Measured and simulated S-parameters of the 1D right-handed unit cell.

# Chapter 5

# DESIGN AND TEST THE 20-WAY POWER DIVIDER

In this chapter, we present the details about the 20-way power divider proposed in Chapter 3. In section 5.1, we describe the design details of the 20-way power divider and the simulation results. Then we discuss fabrication in section 5.2, and finally we give the experimental results in section 5.3.

## 5.1 DESIGN AND SIMULATE THE 20-WAY POWER DIVIDER

In chapter 4, the 1D left-handed and right-handed unit cells were designed and tested; therefore, the 2D left-handed and right-handed unit cells can be designed directly from the corresponding 1D unit cells. Figure 5.1 and Figure 5.2 show the circuit models for the 2D left-handed and right-handed unit cells, respectively. As calculated in chapter 4, we choose the Taconic TLY-5 substrate [29] with dielectric constant of

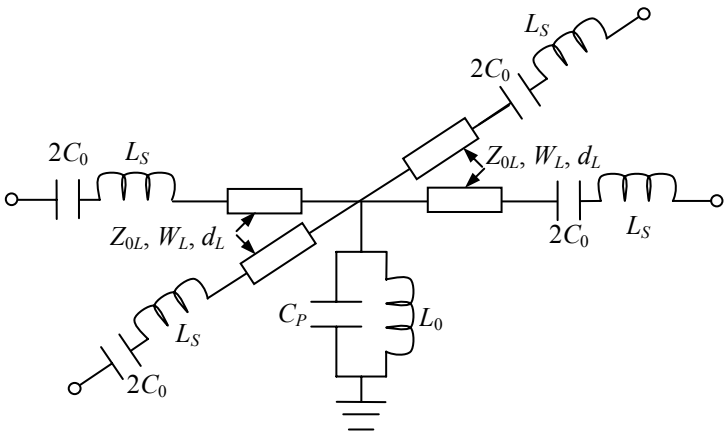


Fig. 5.1. Microstrip line 2D left-handed unit cell
included the parasitic effects of the surface-mount components.

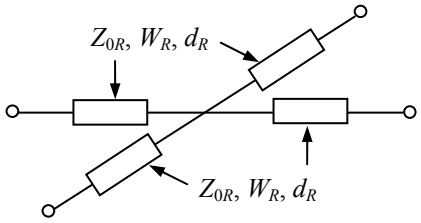


Fig.5.2. Microstrip line 2D right-handed unit cell.

2.2 and dielectric height of 1.575 mm (62 mil), and we obtain the parameters of 2D unit cells: $W_L$ = 1.668 mm, $W_R$ = 1.586 mm, $d_L$ = 2.55 mm, $d_R$ = 3.55 mm, $Z_{0L}$ = 91.3 Ω, $Z_{0R}$ = 93.5 Ω, $L_0$ = 43 nH with parasitic effect $C_p$ = 0.15 pF, and $2C_0$ = 10 pF with parasitic effect $L_S$ = 0.15 nH. The length for accommodating the capacitor is 1 mm; thus, the size of the 2D left-handed unit cell is 7.1 mm x 7.1 mm, and it is the same as the size of the 2D right-handed unit cell.

Figure 5.3 shows the simulated frequency responses of S-parameters of a 5 by 5 TMM structure using circuit models in Figure 5.1 and Figure 5.2. The reference impedance of the input port is 4.7 Ω, and those of the output ports are 93.5 Ω. The simulations include the parasitic effects of lumped components. The simulation results display that the difference between the coupling phases is either 0° or 11.4° at the design frequency, 1 GHz. To achieve the equal phases at peripheral ports, extra compensating microstrip lines with two different lengths should be connected to the output ports of the TMM structure as shown in Figure 3.41. The characteristic impedance of these two different length microstrip lines is equal to 93.5 Ω. As denoted in Figure 3.41, TL1 which is connected to the peripheral right-handed unit cell is chosen to be 7 mm, and TL2 which is connected to the peripheral left-handed unit cell is chosen to be 15.18 mm. These values ensure that the TL1 and TL2 are compact. In order that the output ports of the 20-way power divider are located on a straight line, TL2 must be meandered to ensure that the distance between its ports is 7 mm which is equal to TL1. Moreover, the phase shift difference of these two microstrip lines is 11.4° at 1 GHz, when TL2 is curved.

Figure 5.4 displays the simulated frequency responses of S-parameters of the 20-way power divider. The reference impedance is 4.7 Ω at input port and 93.5 Ω at output ports. The simulations include the parasitic effects of lumped components, inductors and capacitors. The simulated $S_{0,0}$ shows that good match is achieved at

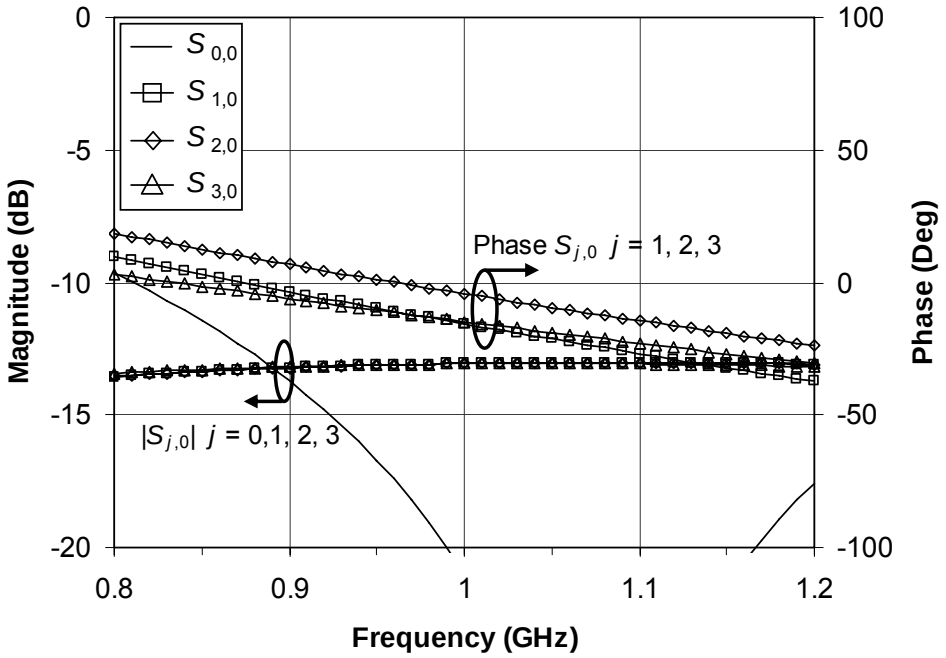


Fig. 5.3. The simulated frequency responses of the 5 by 5 TMM structure.

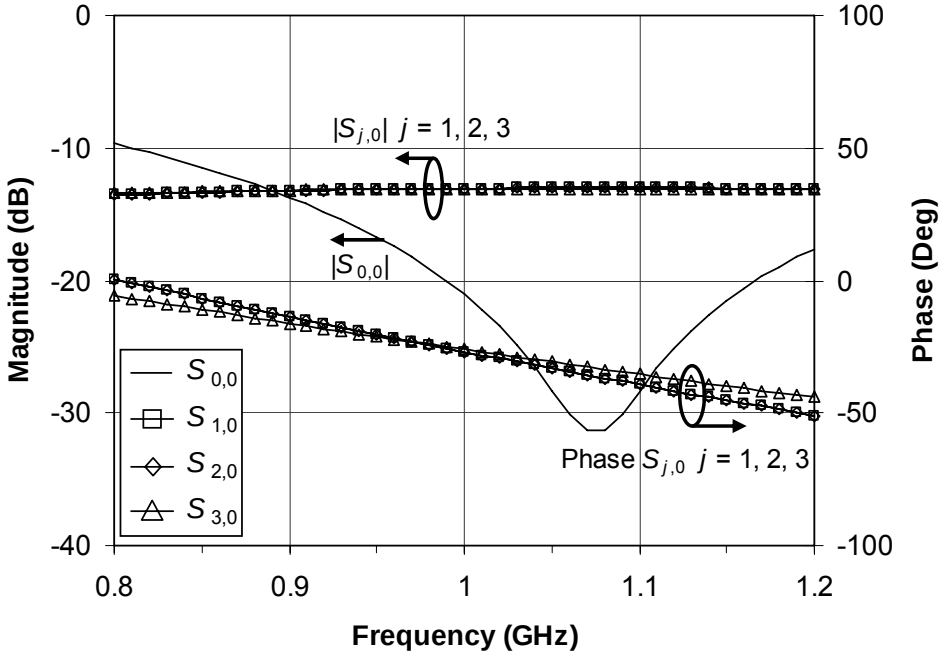


Fig. 5.4. The simulated frequency responses of the 20-way power divider.

input port over a wide bandwidth, and the best match occurs at 1.07 GHz. Residual mismatch is mainly reason which causes the discrepancy from 1 GHz. The simulated $S_{1,0}$, $S_{2,0}$ and $S_{3,0}$ reveal that the coupling phases from input port to output ports become equal at 0.97 GHz, and this means that equal magnitude and phase power division can be obtained at this frequency. The parasitic effects of lumped components cause the deviation from the theoretical value of centre frequency, 1 GHz. Furthermore, the coupling magnitudes are -13.1 dB at 1 GHz, which is similar to the theoretical value of -13 dB, and over a range 0.9 GHz to 1.1 GHz, they are almost identical and flat, and the corresponding coupling phases differ less than 4°. Figure 5.5 shows the simulated representative output port isolations. It is observed that all output port isolations are -26 dB at 0.97 GHz, and this value is consistent with the theoretical value of a lossless 20-way power divider. Isolations between ports 1 and 20, 5 and 6, 10 and 11, 15 and 16 are the same and hence only $|S_{20,1}|$ is shown in Figure 5.5, and other isolations vary in the same manner. Moreover, it can be seen that $|S_{20,1}|$ increases most rapidly away from the centre frequency.

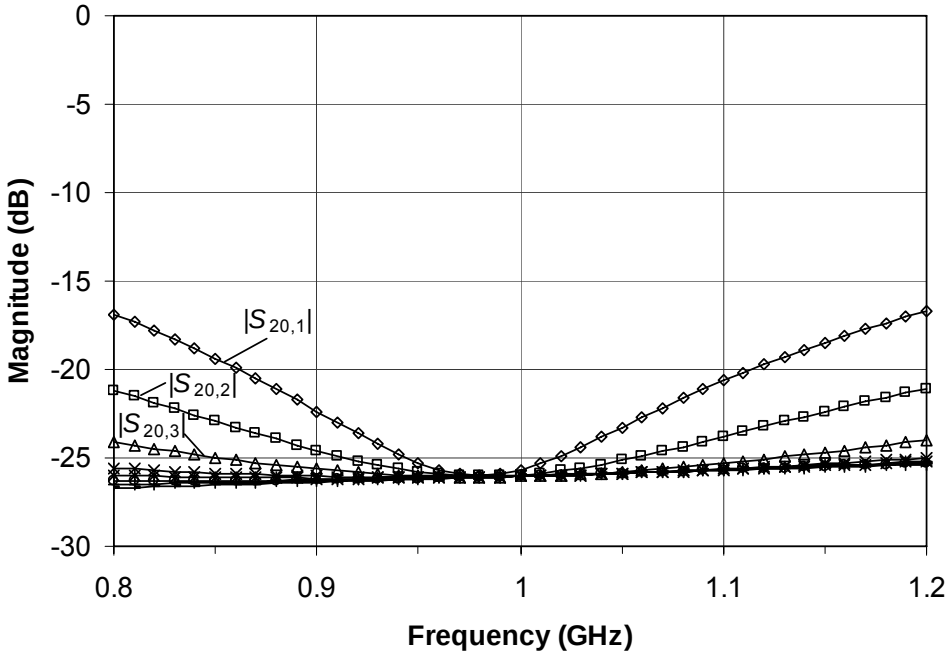


Fig. 5.5. The simulated representative output port isolations.

## 5.2 FABRICATION OF THE TEST CIRCUIT

To fabricate the 20-way power divider, we use the same components as in the experiment of the 1D unit cells. Figure 5.6 and Figure 5.7 show the physical layout of the 2D left-handed and right-handed unit cells with design parameters, respectively. In the 2D left-handed unit cell, the width of two cross microstrip lines is 1.668 mm, and the length of those is 5.1 mm, and their characteristic impedances, $Z_{0L}$, are 91.3 Ω. A drill hole which is in the centre of the microstrip lines is used to accommodate the inductor, and its diameter is 1.5 mm. The distance with 1 mm is used to allow for the capacitor length. In the 2D right-handed unit cell, two cross microstrip lines have the width of 1.586 mm and the length of 7.1 mm, and their characteristic impedances, $Z_{0R}$, are 93.5 Ω. Therefore, the sizes of the 2D left-handed and right-handed unit cells are the same, and they are 7.1 mm x 7.1 mm.

Figure 5.8 depicts the physical layouts of the compensating microstrip lines, TL1 and TL2. These two microstrip lines have the width of 1.586 mm, and hence their characteristic impedances are 93.5 Ω, which are matched to the peripheral left-handed and right-handed unit cells of the TMM structure. The length of microstrip line is 7 mm for TL1, and 15.18 mm for TL2; however, TL2 is meandered so that the distance between its ports is also 7 mm.

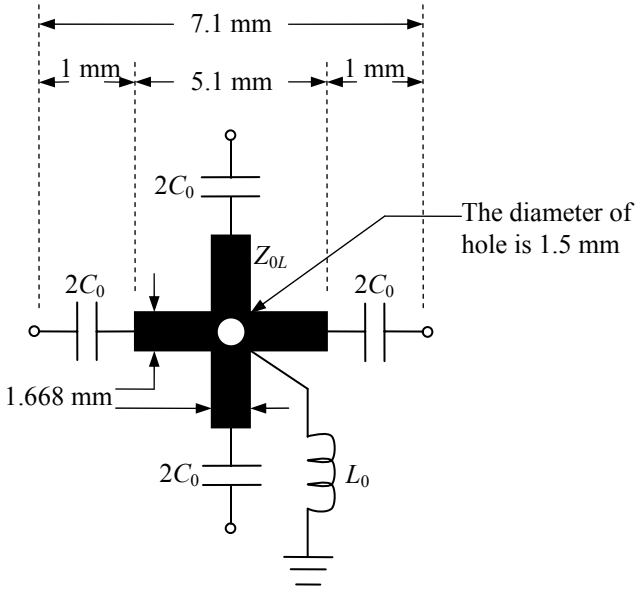


Fig. 5.6. The physical layout of the 2D left-handed unit cell.

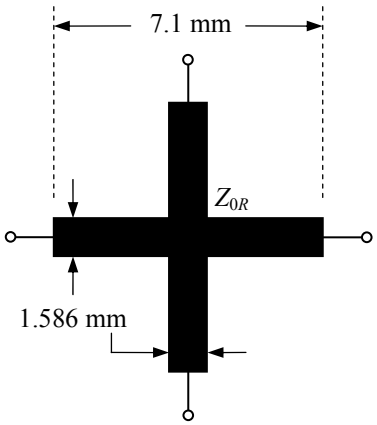


Fig. 5.7. The physical layout of the 2D right-handed unit cell.

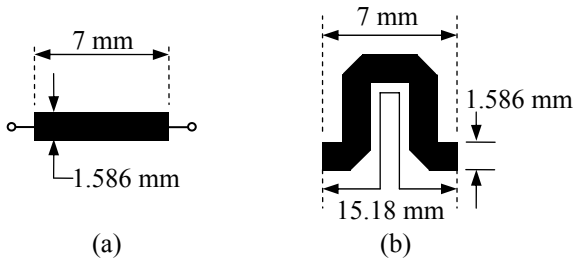


Fig. 5.8. The physical layouts of the compensating lines: (a) TL1, and (b) TL2.

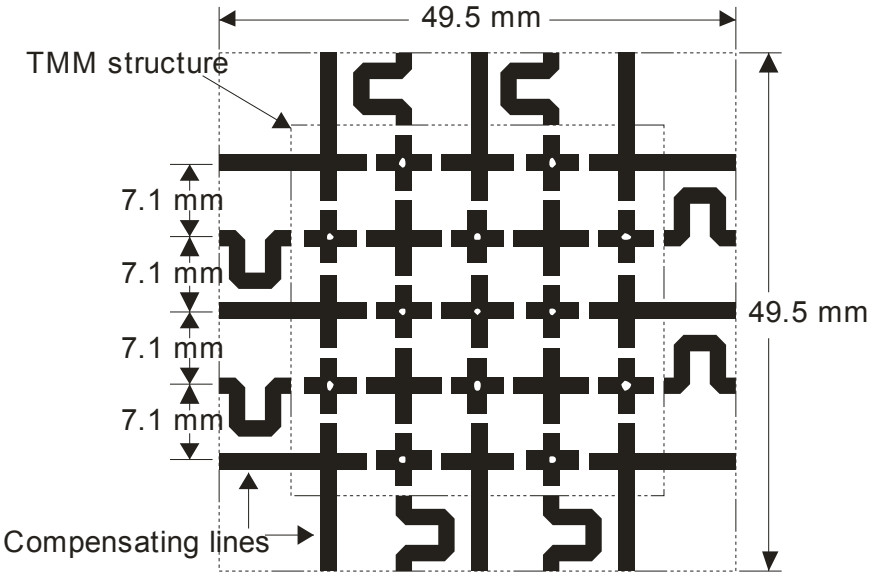


Fig. 5.9. The physical layout of the 20-way power divider.

Figure 5.9 shows the physical layout of the 20-way power divider based upon the TMM structure and compensation lines. The gaps between the left-handed unit cells and right-handed unit cells, and between the left-handed unit cells and TL2 microstrip

lines, accommodate the capacitors. The drill hole in the central right-handed unit cell is used to put the input probe feeding connector, and its diameter is 1.3 mm. Since TL2 microstrip lines are meandered, it is clear that the output ports are located on a straight line on each side; hence, the power divider is a square shape, and the size is 49.5 mm x 49.5 mm.

The divider test circuit is measured in a 50 Ω microstrip line test fixture, so quarter-wave transformers are used to transform 50 Ω to 93.5 Ω to match the output ports of the divider at 1 GHz, and 50 Ω feeding lines are used to connect to transformers and the SMA connectors. Therefore, the output ports of the divider are matched terminations only at 1 GHz.

Using the formula for a quarter-wave transformer [28], the characteristic impedance of the quarter-wave transformer is equal to 68.4 Ω, and using microstrip line design equations [28], the transformer has the width of 2.9 mm and the length of 55.228 mm. As shown in Figure 5.9, it is apparent that the distance between the two adjacent output ports is 7.1 mm, but it is not enough to locate the SMA connectors at terminations. Figure 5.10 shows the physical layouts of the transformers and 50 Ω feeding lines. Since the circuit is symmetrical, only three ports with the transformers and feeding lines are shown in Figure 5.10. In order to fix the SMA connectors at terminations, the distance between two adjacent output ports is chosen to be 14 mm, and the transformers which are connected to port 1 and port 2 are meandered to ensure that this distance is achieved. Moreover, to obtain that the output ports are located on a straight line, 50 Ω feeding lines with three different lengths are connected to the transformers. The width of the feeding lines is 4.8 mm, and the length is 15.738 mm for port 1, and 12.88 mm for port 2, and 10.022 mm for port 3.

The final full layout of the 20-way power divider test circuit is shown in Figure 5.11. Figure 5.12 depicts a photograph of the fabricated 20-way power divider test circuit board with the SMA connectors at terminations. Figure 5.12 (b) shows the view of the fabricated square-shaped metamaterial power divider. The input port is probe-fed using an SMA connector which is fixed on the bottom of the PCB mounting board as shown in Figure 5.13. Because the input SMA connector is longer than the height of the mounting base, an extra block is used to fix it.

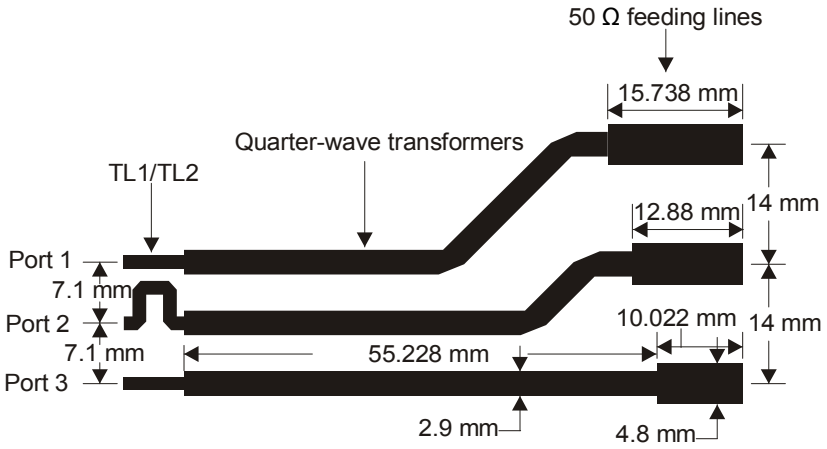


Fig. 5.10. The physical layouts of the transformers and feeding lines.

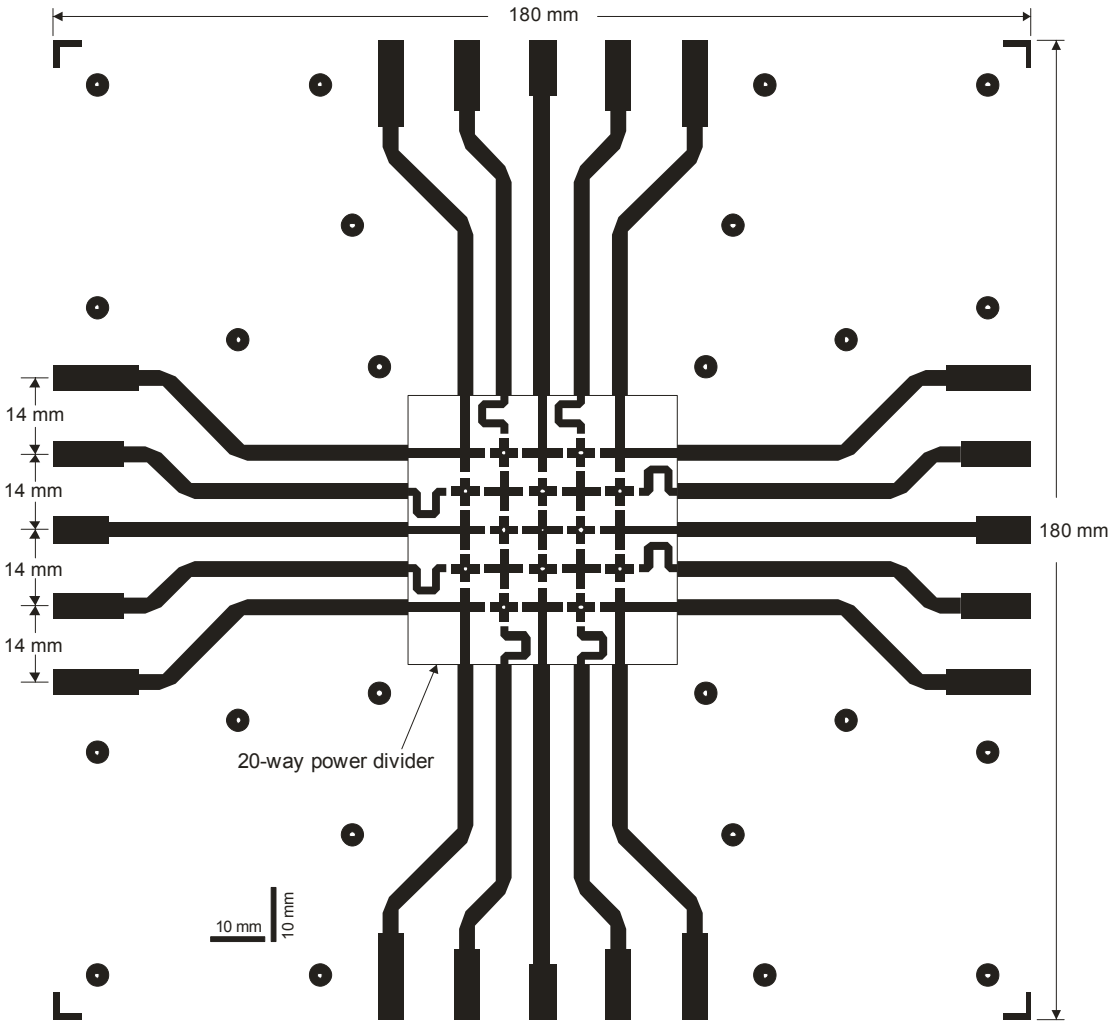


Fig. 5.11. The physical layout of the 20-way power divider test circuit.

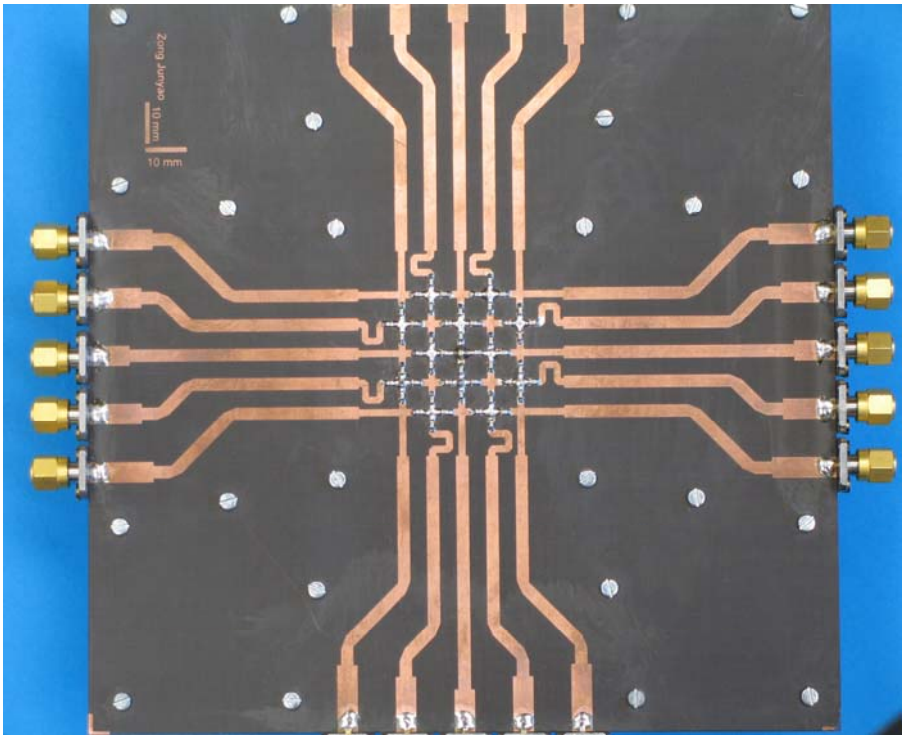


(a)

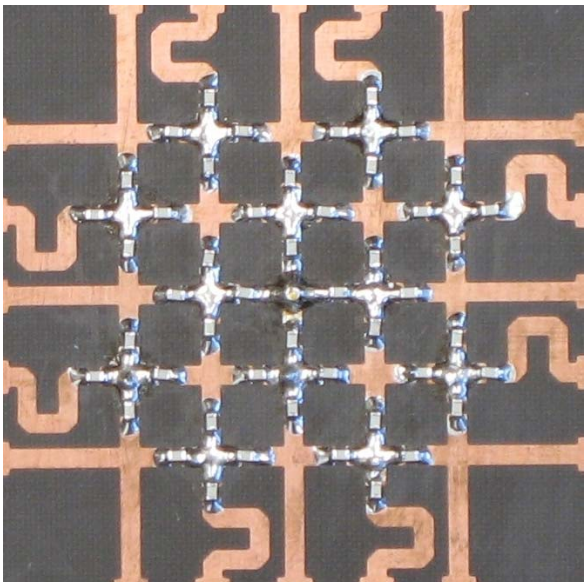

(b)

Fig. 5.12. The photo of the fabricated 20-way power divider: (a) overall view of the test circuit, and (b) close-up view of the 20-way metamaterial power divider.

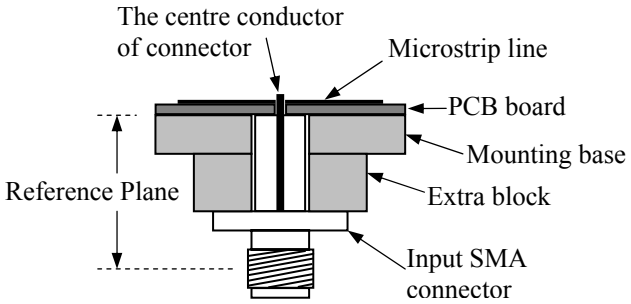


Fig. 5.13. The cross section view of the input SMA connector part.

## 5.3 EXPERIMENTAL RESULTS

All measurements were carried out on an Agilent Technologies E8362B PNA Network analyzer. When the circuit was measured, two ports were tested at a time, which are the input port and one of the output ports; hence, we obtain 20 groups of measurement results. The model for each measurement result includes the input SMA connector with effect of discontinuity, the 20-way power divider, the quarter-wave transformer, the 50 Ω feeding line, and the output SMA connector with effect of discontinuity. Using the de-embedding method, which was discussed in chapter 4, we eliminate the output SMA connector with effect of discontinuity, the 50 Ω feeding lines, the quarter-wave transformers, and the input SMA connector; therefore, the de-embedded measurement results of the 20-way power divider can be obtained. In de-embedding, we ignore the effect of discontinuity between the input SMA connector and the microstrip lines, and it will be shown later that this effect is significant. Furthermore, there are three main sources of random error: tolerance of the lumped components, inductors and capacitors, and residual mismatch of the 50 Ω SMA connectors, and random measurement errors.

Figure 5.14 shows the structure of the input SMA connector [33]. According to the dimensions of the connector, the length between the reference planes is equal to 22.63 mm, and it is also considered as the length of the coaxial transmission line in the connector. Because the filled material in the connector is Teflon, whose relative permittivity $\varepsilon_r$ is 2.08, the wave length of the coaxial transmission line is obtained by

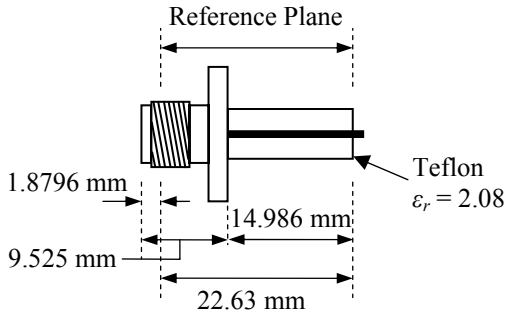


Fig. 5.14. The structure of the input SMA connector.

$$\lambda = \frac{\lambda_0}{\sqrt{\varepsilon_r}} = \frac{300}{\sqrt{2.08}} = 208mm, \tag{5.1}$$

where $\lambda_0$ is the wave length in the free space at 1 GHz. And the electrical length of the coaxial transmission line can be calculated by

$$EL = \frac{d}{\lambda} \times 360^\circ = \frac{22.63}{208} \times 360^\circ = 39.17^\circ, \tag{5.2}$$

where $d$ is the length of the coaxial transmission line, and the working frequency is 1 GHz.

Figure 5.15 displays the de-embedding model for the measurement results of the 20-way power divider. The output SMA connectors are the same type as those which were used in Chapter 4, so they are considered to have the same model shown in Figure 4.20, and they have the same values of parameters which were determined in Chapter 4. The length of 50 Ω feeding line is -15.738 mm for the measurement results of port 1, 5, 6, 10, 11, 15, 16, 20, and -12.88 mm for port 2, 4, 7, 9, 12, 14, 17, 19, and -10.022 mm for port 3, 8, 13, 18.

Figure 5.16 shows the de-embedded measurement results which include the average magnitude of the input reflection coefficient $S_{0,0}$, and the magnitudes and phases of the couplings $S_{j,0}$, where $j$ = 1…20. The reference impedance is 4.7 Ω for the input port, and 93.5 Ω for the output ports. Because there are twenty 2-port S-parameter data sets, there are twenty traces for $S_{0,0}$, and these traces are all consistent. Hence, the average measured magnitude of $S_{0,0}$ is shown in Figure 5.16. The twenty couplings are also consistent, and the coupling magnitudes are around -14 dB at 1

GHz. Furthermore, over the range from 0.95 GHz to 1.05 GHz, the coupling magnitudes are almost flat, and their differences are less than 1 dB, and the corresponding coupling phase differences are less than 10°. Because of the limitation of the measurement equipment, such as lack of the suitable termination at the input port, the divider output port isolations were not measured.

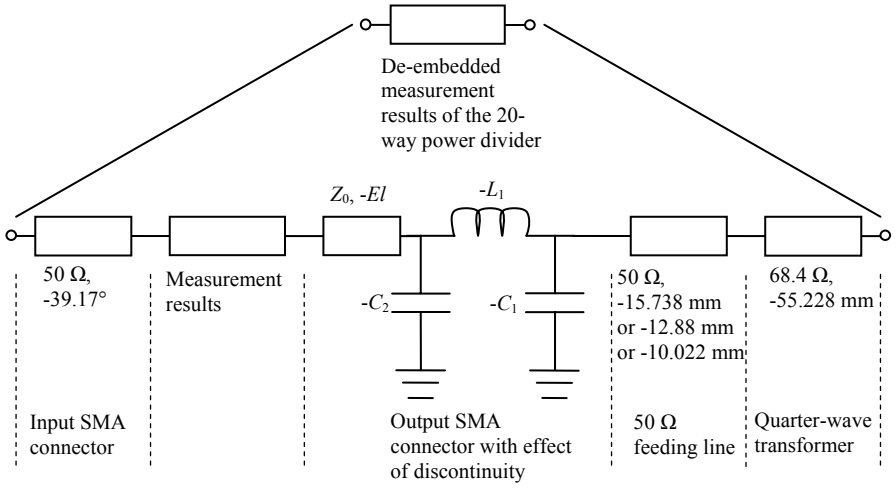


Fig. 5.15. The de-embedding model for the 20-way power divider.

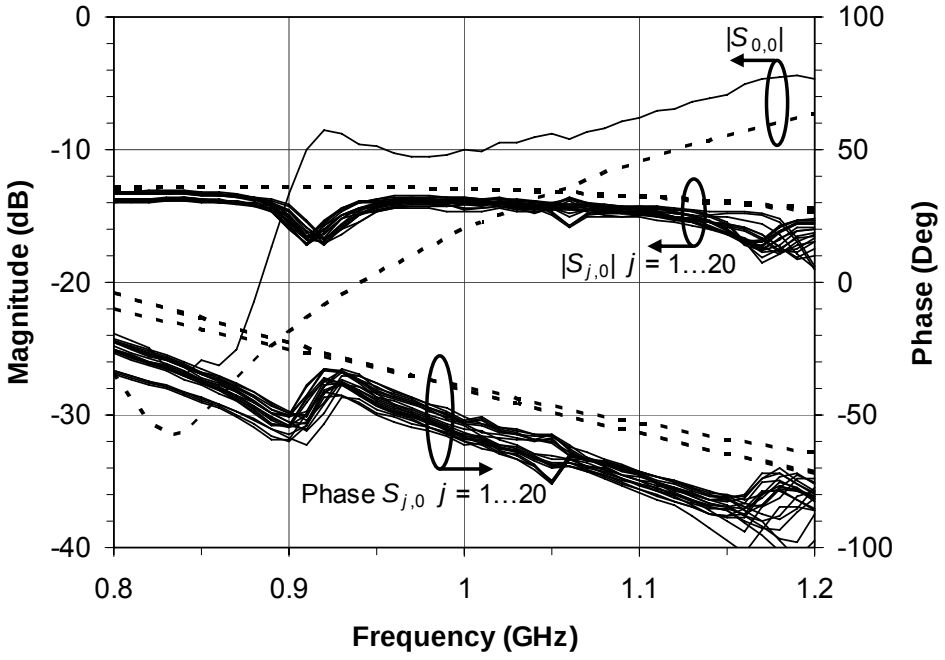


Fig. 5.16. De-embedded measurement results (solid curves) of the 20-way power divider, and the simulation results (dashed curves) which include the effect of the probe feed discontinuity at the input port.

Figures 5.16 also shows the simulation results which include the effect of the probe feed discontinuity of the central tile by the input SMA connector and are plotted using dashed lines. Figure 5.17 displays the electromagnetic structure for the central right-handed unit cell of the 20-way power divider in simulation. Port 5 is a probe-fed port which is used to describe the effect of the discontinuity at the input port of the power divider. Because of the limitation of the electromagnetic simulator, a square shaped probe feed, not a circular shaped, was used in simulation as shown in Figure 5.17. These simulation results indicate the differences between the simulation results in Figure 5.16 and the simulation results in Figure 5.4 which did not include the effect of the probe feed discontinuity of the central tile. It is clear that this effect of the discontinuity at the input port causes a significant effect on the $S_{0,0}$ response and the divider coupling phases. Figure 5.18 shows another simulation of the 20-way power divider which includes the effect of the microstrip cross in the right-handed unit cells. It can be seen that this effect presents a resonance in the coupling responses at around 1.05 GHz, and this phenomenon can be also seen in the measurement results.

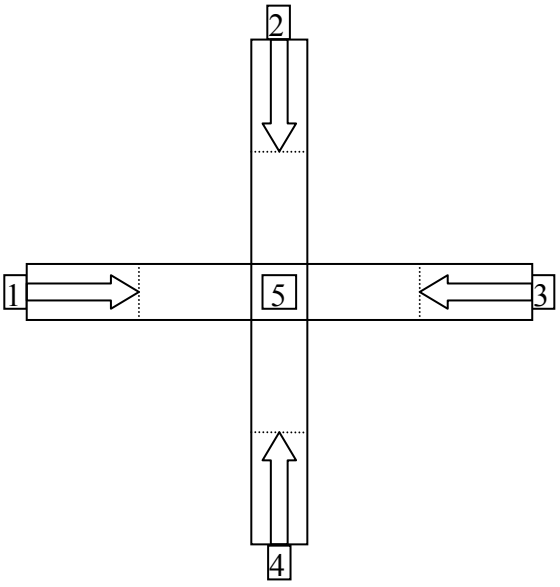


Fig. 5.17. The electromagnetic structure for the central right-handed cell of the power divider.

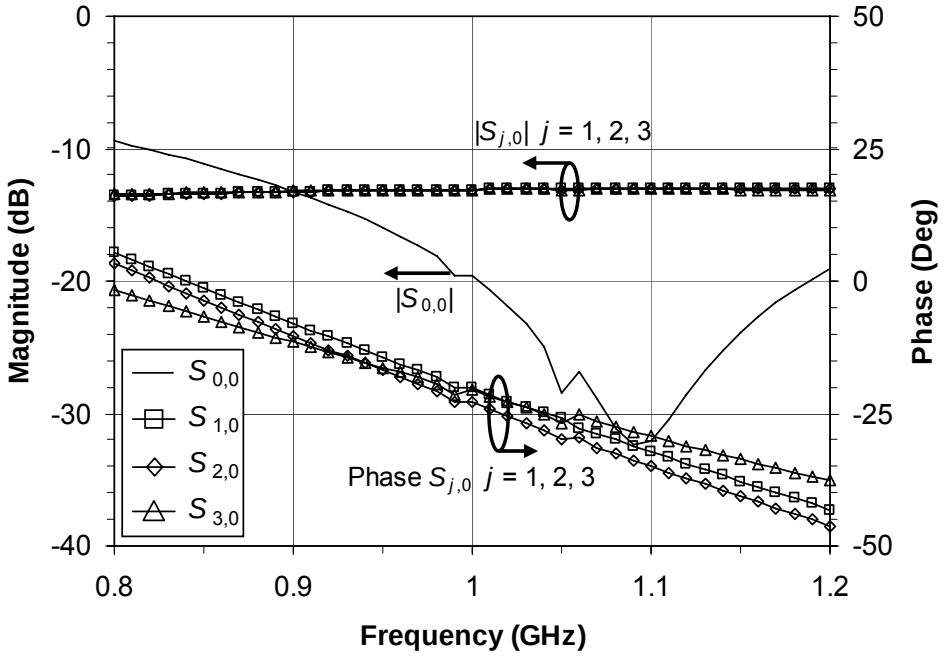


Fig. 5.18. The simulated frequency responses of the 20-way power divider which includes the effect of the microstrip cross in the right-handed unit cells.

Normalised divider couplings can eliminate common artifacts and measurement uncertainties, and normalised corresponding coupling phases can help us to check the bandwidth where in-phase power division can be achieved. Since the fabricated circuit is symmetrical, three average de-embedded divider couplings are expressed as

$$S_{1,0ave} = \frac{S_{1,0} + S_{5,0} + S_{6,0} + S_{10,0} + S_{11,0} + S_{15,0} + S_{16,0} + S_{20,0}}{8}, \tag{5.3}$$

$$S_{2,0ave} = \frac{S_{2,0} + S_{4,0} + S_{7,0} + S_{9,0} + S_{12,0} + S_{14,0} + S_{17,0} + S_{19,0}}{8}, \tag{5.4}$$

$$S_{3,0ave} = \frac{S_{3,0} + S_{8,0} + S_{13,0} + S_{18,0}}{4}. \tag{5.5}$$

Then the overall average de-embedded divider coupling is written as

$$\begin{aligned} C_{ave} &= \frac{8S_{1,0ave} + 8S_{2,0ave} + 4S_{3,0ave}}{20} \\ &= 0.4S_{1,0ave} + 0.4S_{2,0ave} + 0.2S_{3,0ave}. \end{aligned} \tag{5.6}$$

And the normalised de-embedded divider couplings can be calculated as

$$S_{1,0nor} = S_{1,0ave} / C_{ave} , \tag{5.7}$$

$$S_{2,0nor} = S_{2,0ave} / C_{ave} , \tag{5.8}$$

$$S_{3,0nor} = S_{3,0ave} / C_{ave} . \tag{5.9}$$

Moreover, the normalised simulated divider couplings are also calculated in the same way as above. Figure 5.19 (a) and (b) show the normalised measured coupling phases and the normalised simulated coupling phases, respectively. It is observed that there is a resonance in the coupling responses at around 1.05 GHz in measurements shown in Figure 5.19 (a). Except for the resonance at 1.05 GHz, the differences between the normalised measured coupling phases are less than 10° over the range from 0.9 GHz to 1.1 GHz, and this is favourable compared to the simulation results where the differences between the normalised simulated coupling phases are less than 4° over the same range. Furthermore, except for the resonance at 1.05 GHz, the measured and simulated normalised coupling phases differ less than 5° over this same range.

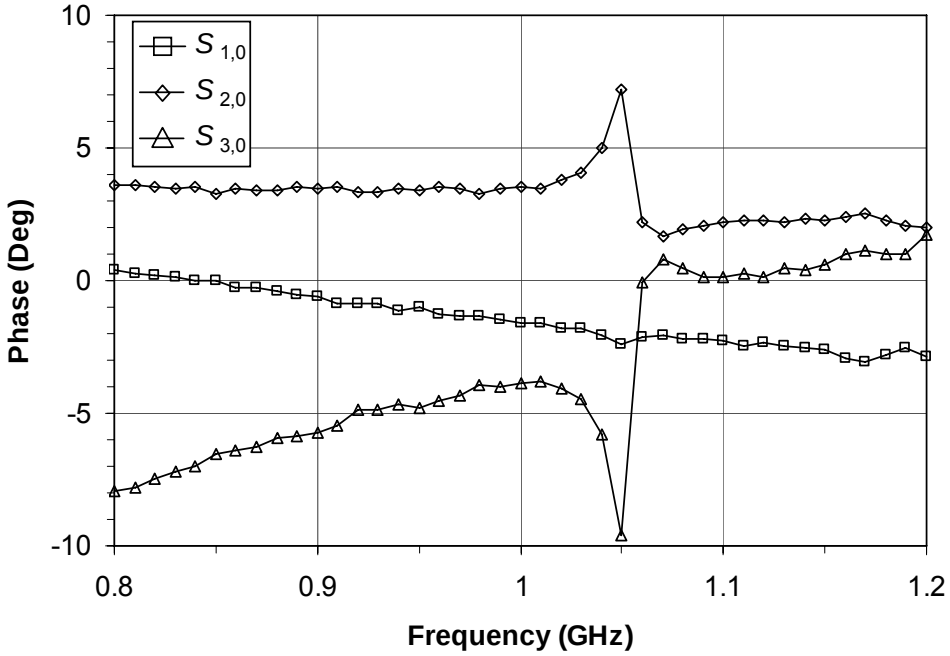


(a)

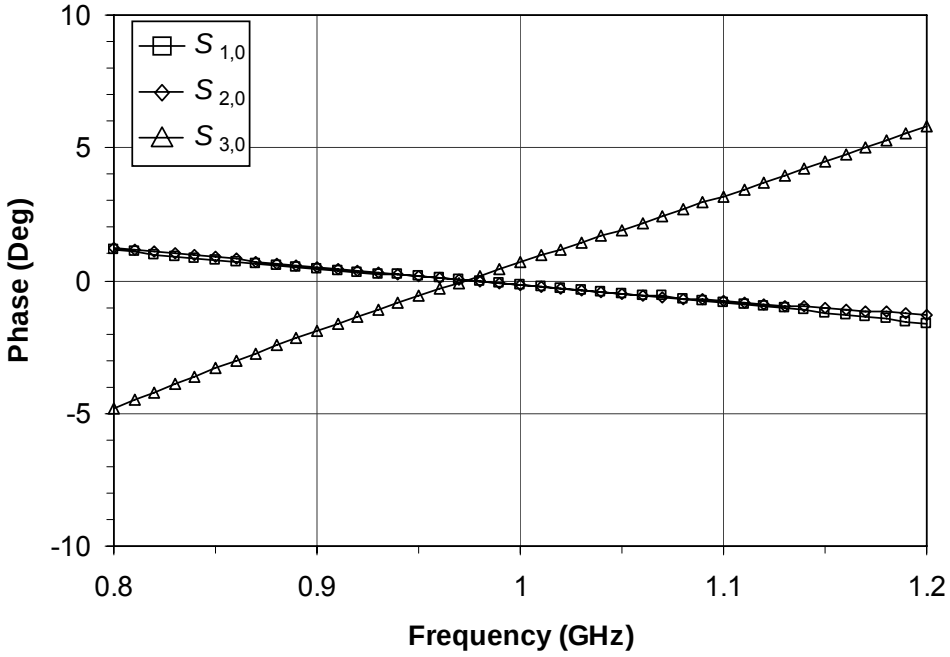


(b)

Fig. 5.19. Normalised divider coupling phases: (a) measured, and (b) simulated.

# Chapter 6

# CONCLUSION

## 6.1 RESEARCH SUMMARY

In this thesis, we proposed a novel square-shaped *N*-way metamaterial power divider. It comprises left-handed and right-handed unit cells and is implemented in microstrip line. In chapter 2, we have given a brief overview of the left-handed transmission line.

This *N*-way power divider is based on the tessellated metamaterial (TMM) structure, where the left-handed and right-handed unit cells are located in a checkerboard tessellation, and the infinite wavelength phenomenon in two-dimensions. To study the TMM structure, in chapter 3 we simulated a 17 by 17 TMM structure. The simulation results show that the voltage, both magnitude and phase, across the TMM structure is nearly constant, so that the TMM structure exhibits the infinite wavelength phenomenon in two-dimensions. For comparison, in chapter 3 we also simulated a 17 by 17 mosaic structure comprised of entire right-handed unit cells, and the simulation results display that the voltage magnitude and phase vary significantly across the mosaic structure.

In chapter 3, we have also simulated the 20-way metamaterial power divider based on the 5 by 5 TMM structure, and for comparison, the power divider which is based upon the 5 by 5 mosaic structure comprised of only right-handed unit cells. The simulation results demonstrate the advantage of the proposed power divider.

To design the left-handed and right-handed unit cells in the TMM structure, in chapter 3 we have simulated a 25 by 17 TMM structure which can be considered as a large TMM structure, and also simulated a 17 by 17 TMM structure with four plane

waves excited at each edge of the structure, and then we found the equivalent 1D left-handed and right-handed models of the 2D unit cells. Therefore, to design the 2D left-handed and right-handed unit cells, we only need to design their equivalent 1D unit cells, and then these design results can be used in the 2D left-handed and right-handed unit cells directly.

In chapter 4, we have given the design method of the 1D left-handed and right-handed unit cells. Then we fabricated the designed 1D left-handed and right-handed unit cells in microstrip line and tested them. The experimental results validate the design method and fabrication techniques.

In chapter 5, we have designed, fabricated and tested a square-shaped 20-way metamaterial power divider. The divider operates at 1 GHz and comprises 12 left-handed unit cells and 13 right-handed unit cells which are placed in a checkerboard tessellation. The size of the divider is 49.5 mm by 49.5 mm. The test results also validate the design method.

In summary, the proposed *N*-way power divider, where *N* is an odd integer multiple of 4, is square-shaped, and gives an equal-amplitude equal-phase power division from the central port to the output ports, where the output ports have four groups and they are located on a straight line in each group. Therefore, it allows convenient integration with amplifier modules in a parallel combined power amplifier.

## 6.2 FURTHER RESEARCH

During the course of this thesis research, several issues were raised and could not be completed. For example, the effect of the probe feed discontinuity at the input port, which causes a significant effect of the S-parameter responses of the divider, needs to be ascertained and considered in the design model. Also, the input impedance of the divider is very low and this needs additional impedance transformers, such as the stepped coaxial impedance transformers, at the input port of the divider. Furthermore, the effect of the microstrip cross in the right-handed unit cell presents a resonance in the coupling responses in the bandwidth, so this effect needs to be considered and further research needs to be explored to eliminate this resonance in the bandwidth. Similarly, in the left-handed unit cell, due to the presence of the surface mount

inductor in the central hole, it introduces a new discontinuity, and the effect of this discontinuity needs to be determined and considered in the design model.

# REFERENCES


[1] K. J. Russell, "Microwave power combining techniques," *IEEE Trans. Microwave Theory Tech*., vol. MTT-27, pp. 472-478, May 1979.

[2] D. F. Peterson, "Radial-symmetric *N*-way TEM-line IMPATT diode power combining arrays," *IEEE Trans. on Microwave Theory and Techniques*, vol. MTT-30, No. 2, pp. 163-173, Feb. 1982.

[3] E. Fathy, S.-W. Lee and D. Kalokitis, "A simplified design approach for radial power combiner," *IEEE Trans. on Microwave Theory and Techniques*, vol. 54, No. 1, pp. 247-255, Jan. 2006.

[4] "Breakthrough of the year: The runners-up," *Science*, vol. 302, No. 5653, pp. 2039-2045, 2003.

[5] V. Veselago, "The electrodynamics of substances with simultaneously negative values of ε and μ," *Soviet Physics Uspekhi*, vol. 10, No. 4, pp. 509-514, 1968.

[6] R. A. Shelby, D. R. Smith, and S. Schultz, "Experimental verification of a negative index of refraction," *Science*, vol. 292, pp. 77–79, Apr. 2001.

[7] G. V. Eleftheriades, A. K. Iyer, and P. C. Kremer, "Planar negative refractive index media using periodically L-C loaded transmission lines," *IEEE Trans. Microw. Theory Tech.*, vol. 50, No. 12, pp. 2702–2712, Dec. 2002.

[8] C. Caloz and T. Itoh, “Transmission line approach of left-handed (LH) materials and microstrip implementation of an artificial LH transmission line,” *IEEE Trans. Antennas Propag.*, vol. 52, No. 5, pp. 1159–1166, May 2004.

[9] M. A. Antoniades and G. V. Eleftheriades, “Compact linear lead/lag metamaterial phase shifters for broadband applications,” *IEEE Antennas and Wireless Propagation Letters*, vol. 2, No. 7, pp. 103–106, Jul. 2003.

[10] G. V. Eleftheriades and K. G. Balmain, *Negative-Refraction Metamaterials: fundamental principles and applications*. New York, Wiley-IEEE, 2005.

[11] C. Caloz and T. Itoch, *Electromagnetic metamaterials: transmission line theory and microwave applications*. New York, Wiley-IEEE, 2005.

[12] K.W. Eccleston, “N-way microwave power divider using two-dimensional meta-materials,” *Electronics Letters*, vol. 42, No. 15, pp. 863 – 864, 20 July 2006.

[13] K.W. Eccleston, “Investigation of a Tessellated Meta-Material Planar Circuit,” *2006 Asia Pacific Microwave Conference*, 12 - 15 Dec. 2006, Yokohama, Japan.

[14] A. Fathy and D. Kalokitis, “Analysis and design of a 30-way radial combiner for Ku-band applications,” *RCA Rev*., vol. 47, pp. 487-508, Dec. 1986.

[15] Z. Galani and S. J. Temple, “A broadband planar *N*-way combiner/divider,” in *1997 IEEE MTT-S Int. Microwave Symp. Dig.*, vol. 77, Issue 1, pp. 499-502, June 1977.

[16] M. D. Abouzahra and K. C. Gupta, “Multiport power divider-combiner circuits using circular-sector-shaped planar components,” *IEEE Trans. on Microwave Theory and Techniques*, vol. 36, No. 12, pp. 1747-1751, December 1988.

[17] M. D. Abouzahra, K. C. Gupta and A. Dumanian, "Use of circular sector shaped planar circuits for multiport power divider-combiner circuits," in *1988 IEEE MTT-S Int. Microwave Symp. Dig.*, vol. 2, pp. 661-664, May 1988.

[18] W. Yau, J. M. Schellenberg and Y. C. Shih, "A new N-way broadband planar power combiner/divider," *1986 IEEE MTT-S Int. Microwave Symp. Dig.*, vol. 86, Issue 1, pp. 147-149, June 1986.

[19] K. W. Eccleston, Q. C. Sun and S. P. Yeo, "Tapered microstrip line power combiners with colinear input ports," *Microwave and Optical Technology Letters*, vol. 15, No. 6, pp. 339-342, 20 August 1997.

[20] Z. Galani, J. L. Lampen, S. J. Temple, "Single-Frequency analysis of radial and planar amplifier combiner circuits," *IEEE Trans. Microwave Theory Tech*., vol. 29, pp. 642-654, July 1981.

[21] M. S. Gupta, "Degradation of power combining efficiency due to variability among signal sources," *IEEE Trans. on Microwave Theory and Techniques*, vol. 40, No. 5, pp. 1031-1034, May 1992.

[22] A. M. Saleh, "Planar electrically symmetric *n*-way hybrid power dividers/combiners," *IEEE Trans. on Microwave Theory and Techniques*, vol. MTT-28, No. 6, pp. 555-563, June 1980.

[23] J. M. Schellenberg and M. Cohn, "A wideband radial power combiner for FET amplifiers," *1978 IEEE international Solid-State Circuits Conference Digest of Technical Papers*, pp. 164-165, 273; February 1978.

[24] K. Iyer, P. C. Kremer, and G. V. Eleftheriades, "Experimental and theoretical verification of focusing in a large, periodically loaded transmission line negative refractive index metamaterial," *Optics Express*, vol. 11, No. 7, pp. 696-708, April 2003.

[25] A. Lai, K. M. K. H. Leong and T. Itoh, "A novel N-port series divider using infinite wavelength phenomena," *2005 IEEE MTT-S Int. Microwave Symp. Dig.*, pp. 1001 - 1004.

[26] M. A. Antonaides and G. V. Eleftheriades, "A broadband series power divider using zero-degree metamaterial phase-shifting lines," *IEEE Microwave and Wireless Component Letters*, vol. 15, No. 11, pp. 808 - 810, Nov. 2005.

[27] S. Ramo, J. R. Whinnery and T. Van. Duzer, *Fields and Waves in Communication Electronics*, 2nd ed. New York, John Wiley & Sons, 1984.

[28] D. M. Pozar, *Microwave engineering*, 3rd ed. New York, John Wiley and Sons, 2005.

[29] Taconic High-Performance Laminates Material Guide, from http://www.taconic-add.com/pdf/taconic-laminate_material_guide.pdf

[30] ATC 600S Series Ultra-Low ESR, High Q, NPO RF & Microwave Capacitors, from http://www.atceramics.com/pdf/600s(1).pdf

[31] ATC Inductor Products Catalog, from http://www.atceramics.com/pdf/inductor_products.pdf

[32] Tech-SELECT Component Selection program, from http://www.atceramics.com/designsupport/index.asp

[33] Coaxial Components Corp. Post-Millennium Edition, from http://www.coaxicom.com/download.html